POLITECNICO DI MILANO

SCHOOL OF INDUSTRIAL AND INFORMATION ENGINEERING
Master Thesis in Materials Engineering and Nanotechnology

Ion Assisted Pulsed Laser Deposition of Titanium Nitride Thin Films: Analysis of Electrical and Optical Properties

Supervisor
Prof. Andrea Li Bassi

Co-Supervisor
Dr. Beatrice Roberta Bricchi

Graduation thesis of
Francesco Andrea Bresciani – 920783

Academic Year 2019 – 2020

ABSTRACT

The exploitation of plasmonic phenomena, and their possible applications in many technological fields, has risen considerable interest over the last years. In principle, the collective electronic oscillation, at the base of plasmonics, can be strongly coupled with light, achieving the twofold effect of a significant intensification of the local electromagnetic field and a confinement of the light below its diffraction limit. These phenomena may be the working principle of many advanced solutions in electronics, telecommunications, solar energy harvesting, photodetection, photochemistry and catalysis, biosensing, optical storage of information and metamaterials.
Thanks to their low ohmic losses and their plasmonic response in the optical range, the noble metals are the most common plasmonic materials. However, they have many drawbacks that are highlighted when it comes to the technological applications. Indeed, they suffer from poor chemical and thermal stability and are mostly incompatible with the standard manufacturing process of silicon. Moreover, the plasmonic frequency of the noble metals, usually in the UV spectrum, is often too high in energy for practical applications, where a good response in the infrared region is often required. Driven by these motivations, the research for alternative plasmonic materials has recently been particularly active. A good plasmonic material should feature a tunable plasma frequency, to cover a wide range of applications, and low ohmic losses, together with good compatibility with the CMOS devices and chemical and thermal stability. All these requirements are satisfied by the titanium nitride (TiN), a compound that belongs to the Transition Metal Nitrides (TMNs), a group of ceramic materials that has been extensively studied due to their intrinsic resistance to the corrosion and the low cost. Titanium nitride is a compound easy to deposit with several techniques and intrinsically non-stoichiometric, this means that its plasmonic response can be tuned, in principle, modifying the parameters of deposition.

This thesis work deals with development of thin TiN films (~ 400 nm thick) via nitrogen ion assisted room temperature Pulsed Laser Deposition (PLD). Several samples were fabricated, varying both the fluence of deposition (from 1.7 to 3.1 J/cm^2) and the acceleration voltage of the ions (from 200 to 350 V),

and comparing the results with TiN films deposited via traditional PLD (i.e. without assisting ions). The effects of the assisting ions on the properties of the film were extensively studied, in particular focusing on the structure, the composition, the electrical characteristics and the optical response. Moreover, the effect of different post-deposition thermal treatments at 700 and 865°C were studied. Finally, a preliminary study on the internal stress and the electrical properties of the films as a function of the thickness was carried out on films deposited both with and without ion assistance.
From the beginning, the EDXS and Raman analysis indicated an increasing trend in the nitrogen content in the films as the energy of the assisting ions was enhanced that, furthermore, was paired with a decrease in the oxygen concentration in the films. The analysis repeated after the thermal treatments highlighted an increase of the oxygen together with an enhancement of nitrogen-titanium ratio in almost all the samples. The electrical measurements, as the energy of the ions was increased, registered a lowering of the electronic density, together with an increase in the mobility and in the resistivity.
The annealing treatments often determined a lowering of the resistivity, however, the lowest value achieved was even an order of magnitude higher with respect to the best values of the literature. Moreover, the results of the optical measurements suggested that the thermal treatments favoured an improvement of the film quality, in particular if carried out at high temperature, but they also highlighted that the quality was probably decreased by the ion bombardment.
The residual stress and electrical measurements as a function of the thickness highlighted some possible trends, but the statistics was definitely too low to draw some definitive conclusions.
Thus, it is clear that additional studies are needed to better understand the effect of the ion assistance and the thermal treatments on PLD TiN films. In particular, further investigation on the crystallinity of the films through XRD analysis are of utterly importance to have a complete description of the properties.

SOMMARIO

Nel corso degli ultimi anni, la plasmonica e le sue possibili applicazioni tecnologiche hanno suscitato un notevole interesse nella comunità scientifica. In linea di principio, è possibile ottenere un forte accoppiamento tra le oscillazioni elettroniche collettive, alla base della plasmonica, e la radiazione luminosa, comportando una notevole intensificazione del campo elettromagnetico locale e un confinamento della luce al di sotto del limite di diffrazione. Questi due fenomeni possono essere sfruttati in molteplici soluzioni avanzate in elettronica, telecomunicazioni, celle fotovoltaiche, fotorilevazione, fotochimica e catalisi, *biosensing*, archiviazione ottica di informazioni e metamateriali.
Grazie alle contenute perdite ohmiche nel visibile, i metalli nobili sono i materiali più comunemente utilizzati in questo campo. Tuttavia, nel tentativo di sfruttarli in possibili applicazioni tecnologiche, sono emersi notevoli limitazioni. Infatti, oltre ad una scarsa stabilità chimica e termica, sono in generale incompatibili con i processi di produzione standard del silicio. Oltretutto, la frequenza di plasma dei metalli nobili è solitamente nello spettro ultravioletto, troppo elevata dal punto di vista energetico per le applicazioni pratiche, dove è solitamente richiesta una buona risposta nell'infrarosso.
Spinta da queste motivazioni, la ricerca di materiali plasmonici alternativi è stata recentemente particolarmente attiva. In generale, un buon materiale plasmonico dovrebbe essere caratterizzato dalla possibilità di regolare la sua frequenza di plasma, per coprire un ampio spettro di applicazioni, e da basse perdite ohmiche, oltre che da un'elevata compatibilità con i dispositivi CMOS e una buona stabilità termica e chimica. Tutti questi requisiti sono soddisfatti dal nitruro di titanio (TiN), un composto appartenente alla famiglia dei Nitruri di Metalli di Transizione (*Transition Metal Nitrides*, TMNs), un gruppo di materiali ceramici che è stato estensivamente studiato per l'elevata resistenza alla corrosione e il basso costo. Inoltre, il nitruro di titanio è un composto facilmente depositabile con svariate tecniche e intrinsecamente non stechiometrico, il che significa che la risposta plasmonica può essere regolata, in linea di principio, modificando i parametri di deposizione.

Durante questo lavoro di tesi, sono stati sviluppati diversi film sottili di TiN (spessi $\sim$ 400 nm) depositati a temperatura ambiente tramite *Pulsed*

Laser Deposition (PLD) assistita con ioni di azoto. Sono stati fabbricati diversi campioni, variando la fluenza di deposizione (da 1.7 a 3.1 J/cm^2) e la differenza di potenziale di accelerazione degli ioni (da 200 a 350 V), e confrontando i risultati con dei campioni di TiN depositati tramite PLD tradizionale, cioè senza assistenza ionica. In questo modo è stato possibile studiare approfonditamente l'effetto dell'assistenza degli ioni, concentrandosi in particolare sulla struttura, la composizione, le proprietà elettriche e la risposta ottica dei campioni. Inoltre, è stato investigato anche l'effetto di diversi trattamenti termici a 700 e 865°C effettuati dopo la deposizione. Infine, è stato condotto uno studio preliminare sugli stress interni e le proprietà elettriche dei film in funzione dello spessore, sia su film depositati con assistenza ionica, che senza.
Fin dall'inizio, le analisi EDXS e Raman hanno indicato che un aumento dell'energia degli ioni comportava un incremento del contenuto di azoto nei campioni e, contemporaneamente, una riduzione della concentrazione di ossigeno. Le analisi ripetute dopo i trattamenti termici hanno evidenziato un aumento dell'ossigeno e un incremento del rapporto azoto-titanio in quasi tutti i campioni. Le misure elettriche hanno registrato un abbassamento della densità elettronica e un aumento della mobilità e della resistività a seguito dell'incremento dell'energia degli ioni.
A seguito dei trattamenti termici, è stata registrata una generale diminuzione della resistività, tuttavia i valori misurati sono rimasti circa un ordine di grandezza superiori rispetto ai migliori riportati in letteratura. Inoltre, i risultati delle misure ottiche suggeriscono che questi trattamenti possano aver favorito un miglioramento della qualità dei film, specialmente se compiuti ad elevata temperatura, qualità che, invece, era stata probabilmente ridotta dal bombardamento ionico.
Lo studio degli stress residui e delle misure elettriche in funzione dello spessore ha evidenziato dei possibili trend, ma la statistica era decisamente troppo bassa per tracciare delle conclusioni definitive.
È dunque chiaro che ulteriori studi sono necessari per migliorare la comprensione dell'effetto dell'assistenza ionica e dei trattamenti termici sui film di TiN depositati con PLD. In particolare, ulteriori studi sulla cristallinità dei campioni con analisi XRD sono fondamentali per ottenere una descrizione completa delle proprietà.

CONTENTS

1. TiN thin films: an overview 1

1.1 TiN structure and properties 1

1.2 Applications as plasmonic material 2

1.3 Thin TiN films 6

1.3.1 Electronic and optical properties 6

1.3.2 Film growth and residual stresses 13

1.3.3 Grains growth orientation 18

1.3.4 Oxidation of TiN 23

1.3.5 Ion Beam Assisted Deposition (IBAD) 24

1.3.6 Ultrathin TiN films 27

1.4 Previous results from the research group: a starting point . . 31

1.5 Thesis objectives 34

2. Experimental methods 36

2.1 Pulsed Laser Deposition (PLD) 36

2.1.1 Radio Frequency (RF) Ion Gun 39

2.2 Scanning Electron Microscopy (SEM) 40

2.2.1 Energy Dispersive X-ray Spectroscopy (EDXS) 41

2.3 Raman Spectroscopy 43

2.3.1 Raman Spectroscopy of TiN 45

2.4 Electrical and Hall measurements 47

2.5 Optical reflectance measurements 51

2.5.1 Reflectance behaviour of TiN 52

2.6 Thermal treatments 56

2.7 Residual stresses measurements setup 57

3. Titanium nitride thin films deposited via ion assisted PLD 59

3.1 As-deposited samples analysis 59

3.1.1 EDXS measurements 62

3.1.2 Raman analysis 67

3.1.3 Electrical measurements 72

3.1.4 Reflectance measurements 76

3.1.5 Conclusions 82
3.2 Effect of the thermal treatments 84
3.2.1 EDXS analysis 84
3.2.2 Raman analysis 88
3.2.3 Electrical analysis 90
3.2.4 Optical analysis 94
3.2.5 Conclusions 99

4. Thickness dependent analysis 102
4.1 Residual stress 102
4.1.1 Results 102
4.2 Electrical measurements 106
4.2.1 Results 106

5. Conclusions and perspectives 109

Appendix 116

A. Fundamentals of plasmonics 117
A.1 The dielectric function of the Free Electron Gas 119
A.2 Lorentz model 121
A.3 Surface plasmon polariton 123
A.4 Localized surface plasmon 127

Bibliography 130

LIST OF FIGURES

1.1 Titanium nitride (TiN) rock-salt structure 1
1.2 Schemes for the enhancement of the efficiency in solar cells exploiting plasmonic phenomena 5
1.3 Calculated TiN Electron Density Of States 6
1.4 Calculated band structure of TiN 7
1.5 Simulation of TiN dielectric function 8
1.6 Interband transitions frequency with respect to cell size and stoichiometry 10
1.7 Experimental dielectric function of two 100 nm thick films . . 11
1.8 *Zone T* of the *Structure Zone Model* 14
1.9 Extended *Structure Zone Model* 15
1.10 Stress evolution of reactive sputtering TiN depending on the nitrogen flux 16
1.11 Scheme of *Volmer-Weber* growth mechanism 17
1.12 Simulated *Volmer-Weber* stress evolution 18
1.13 Threshold thickness depending on the strain into the film . . . 19
1.14 Stages and threshold thickness of TiN film growth 20
1.15 TiN out-of-plane direction of growth during sputtering 21
1.16 [XRD spectra of IBAD TiN films with different I_A and E_A . . 26
1.17 Cross-over thickness in IBAD films depending on V_A 26
1.18 Resistivity and electron free mean path depending on the thickness of a PA-ALD ultrathin TiN films 28
1.19 Comparison between resistivity evaluated by Fuch-Sondheimer model and experimentally for a single crystal TiN film 29
1.20 Real and imaginary part of the dielectric function of TiN films depending on the thickness 29
1.21 Raman spectra of PLD-TiN depending on the annealing and deposition atmosphere 32

2.1 General scheme of a PLD apparatus 37
2.2 Plasma plume during PLD tungsten deposition 38
2.3 RFMAX60 RF Ion Source 40
2.4 Scheme of a SEM 41

2.5 Scheme and intensity peaks of the three different de-excitation mechanism during Raman spectroscopy 44
2.6 Raman spectra of a TiN film obtained via Pulsed Laser-Scattered Ballistic Deposition 46
2.7 Resistivity measurements on a 2D sample with van der Pauw method 48
2.8 Hall effect measurements on a 2D sample with van der Pauw method 49
2.9 General scheme of a Ulbricht's integrating sphere setup 51
2.10 Complex refractive index and optical behaviour 52
2.11 Theoretical reflectance edge of a hypothetical Drude meta . . 53
2.12 Reflectance curve of TiN in the plasmonic edge region 54
2.13 Scheme of the heater setup 56
2.14 Scheme of the experimental setup to measure the residual stress 58

3.1 Cross-section SEM imagines of the samples deposited without ion assistance 61
3.2 Cross-section SEM imagines of the samples deposited with ion acceleration voltage of 350 V 61
3.3 EDXS measurements the oxygen concentration in the samples deposited at 1.7 J/cm^2 63
3.4 EDXS measurements of the oxygen concentration in the as-deposited samples 65
3.5 Correlation between the nitrogen-titanium ratio and the oxygen concentration in the as-deposited samples 65
3.6 EDXS measurements of the N/Ti ratio in the as-deposited samples 66
3.7 Raman spectra depending on the assisting ion acceleration voltage of the samples deposited at 1.7, 1.9 and 3.1 J/cm^2 . . 68
3.8 Raman spectra of reactive magnetron sputtering TiO_xN_y . . . 69
3.9 Raman spectrum of an amorphous TiO_x film 70
3.10 Raman spectrum of the sample deposited at 1.7 J/cm^2 and ion acceleration at 350 V 71
3.11 Mobility data depending on the fluence and the assisting ion acceleration voltage 73
3.12 Electronic density data depending on the fluence and the assisting ion acceleration voltage 74
3.13 Correlation between the nitrogen-titanium ratio and the electronic density in the films 74
3.14 Resistivity data depending on the fluence and the assisting ion acceleration voltage 76

3.15 Reflectance curve of the sample deposited at 1.7 J/cm^2 and no ion assistance . . . 77
3.16 Reflectance curves of the samples deposited at 1.9 J/cm^2 . . . 78
3.17 Reflectance curves of the samples deposited at 200 V . . . 78
3.18 Position of the minimum of reflectance in the as-deposited samples . . . 79
3.19 Correlation between the nitrogen-titanium ratio and the position of the minimum of reflectance . . . 80
3.20 Slope of the reflectance edge in the as-deposited samples . . . 80
3.21 Reflectance value at the minimum and at 1200 nm of the as-deposited samples . . . 82
3.22 EDXS data of the oxygen concentration depending on the thermal treatment . . . 85
3.23 EDXS data of the nitrogen-titanium ratio after the thermal treatment . . . 87
3.24 Raman spectra of the annealed samples deposited at 1.9 J/cm^2 with no ion assistance and at 1.7 J/cm^2 at ion assistance acceleration voltage of 350 V . . . 89
3.25 Resistivity data after the thermal treatments . . . 91
3.26 Reflectance curves of the annealed samples deposited at 1.9 J/cm^2 and 200 V . . . 94
3.27 Position of the reflectance minimum (λ_{min}) of the annealed samples . . . 95
3.28 Values of the slope of the reflectance edge after λ_{min} for the annealed samples . . . 97
3.29 Data of the values of the minimum of reflectance for the annealed samples . . . 98
3.30 Data of the value of the reflectance at 1200 nm for the annealed samples . . . 101

4.1 Residual stress trend as a function of the thickness . . . 103
4.2 Polycrystalline silicon *Volmer-Weber* stress evolution . . . 104
4.3 Resistivity as a function of the thickness of the films . . . 107
4.4 Electronic density and mobility as a function of the thickness of the films deposited with ion assistance . . . 108

A.1 Comparison between Drude model and experimental dielectric function of gold . . . 122
A.2 Scheme of metal-dielectric interface . . . 123
A.3 Not damped dispersion relation of surface plasmon polariton at metal-dielectric interface . . . 125

A.4 Damped dispersion relation of surface plasmon polariton at metal-dielectric interface 126

LIST OF TABLES

1.1 TiN growth direction depending on reactive gas and adparticles 21
1.2 Dielectric function parameters of 12 nm 65 nm thick TiN films 30

3.1 Deposition conditions and samples 60

INTRODUCTION

Over the last decades, we have assisted to a technological progress faster then ever before in the human history. The main role in this rush has always been played by the silicon, that, thanks to its peculiar features, finds application in almost every field, from electronics to solar energy harvesting. One of the development path followed over the year has been the decrease of the dimensions of the components. This has permitted to reduce the use of material, thus to save money, and to increase the number of components in the same space, increasing the capability of the systems. However, thanks to the continuous improvements, the dimension of the components has almost reached the physical limit.
Moreover, the increasing demand of energy, and the evident environmental issues that the use of fossil fuels has caused, has led to a growing request of renewable resources, such as solar energy. However, the existing photovoltaic technology is not sufficiently efficient to satisfy the demand.
To overcame these issues, several alternatives have been proposed, many new materials and techniques have been presented, without having solved the problem yet. Among these solutions, the exploitation of the plasmonics has recently claimed some attention thanks to its possible application in numerous fields, including: solar energy harvesting, electronics, photodetection and telecommunications.
The term plasmonics includes several phenomena that imply the existence of a free electrons collective wave, called plasmon, in a metallic material. These collective oscillations are activated by the interaction with an electromagnetic wave at a precise frequency, called plasma frequency (ω_p). Depending on the geometry of the system and on the characteristics of the stimulus, the result of this interaction can be different. Considering a metallic surface in contact with a dielectric, it is possible to generate an extremely confined electronic oscillation tightly bound to the electromagnetic wave in the dielectric. This strong light-matter interaction causes a local intensification of the electromagnetic field and confinement of the light below the diffraction limit. When the plasmonic excitation happens in a metallic nanoparticle, the

resulting plasmon takes the name of Localized Surface Plasmon (LSP), as it is confined within the dimension of the particle. While, when the considered system is an unconfined metal-dielectric interface, the excitation can propagate as a travelling wave and goes under the the name of Surface Plasmon Polariton (SPP). Both these effects may have interesting technological applications, some of them already extensively studied. For instance, the strong confinement and the intensification of the electromagnetic field can be exploited in the solar energy harvesting, to increase the efficiency of the solar cells, in high density solid state storage for electronics, or even for optical-electronic circuits, smaller that the actual ones based on copper, that could lead to an increase in the density of the components.
The most common materials to exploit the plasmonics phenomena are the noble metals due to their low ohmic losses. However, the plasmonic frequency of such materials in the near UV is a strong limitation for the technological applications, as the electromagnetic window of interest is usually in the infrared region. Moreover, they suffer from high interband losses and incompatibility with silicon manufacturing process. For these reasons, many other materials, that combine a lower electronic density, thus a red-shifted plasma frequency, with low Ohmic losses are currently tested as alternatives. A wide category of materials that feature these characteristics are the Transition Metal Nitrides (TMNs). Even if the noble metals still perform better when the SPP are exploited, the interest in these materials is growing considerably because, in addition to good plasmonic properties, they combine a competitive cost-effectiveness with a high thermal and chemical stability and CMOS compatibility. Among this class of materials, a good and promising candidate is titanium nitride (TiN). This material is particularly interesting due to the wide range of deposition techniques that can be used for the fabrication, from Physical Vapour Deposition (PVD) techniques to cathodic vacuum arc, and to its intrinsic non stoichiometry. Indeed, modifying the atomic ratio of nitrogen and titanium in the material, it is possible to change the electronic density and, consequently, tune the plasmonic frequency.

The aim of this thesis work is the development of thin film of TiN (~ 400 nm) via nitrogen ion assisted room temperature Pulsed Laser Deposition (PLD). Indeed, even if in most of the studies on TiN the chosen technique of deposition is sputtering, the peculiarity of PLD may lead to the discover of new features or possible applications. The use of nitrogen ions to bombard the growing film has as main objectives the tuning of the nitrogen content and the improvement of samples crystallinity and structure. The exploitation of the ion assistance is a consequence of the observations made in a previous thesis work of the research group [1], where the attempts to increase the ni-

trogen content in the films using a background gas during the deposition did not lead to the expected results. Nevertheless, the use of energetic particles striking the film is expected to create additional defects in the specimens. Thus, it is important to balance and deeply investigate pros and cons of this technique.
For the fabrication of the samples several deposition conditions were tested. The films were deposited both with and without ion assistance, modifying the laser energy densities (fluence) and the ion acceleration voltages. Moreover, after the deposition, different thermal treatments, at 700 and 865°C, were performed on all the deposited specimens. The samples were deeply analysed and compared, both before and after the thermal treatments, investigating the role of the different conditions of deposition and annealing. I personally carried out sample synthesis (i.e. deposition and thermal treatments) and characterizations via cross-section images taken with a Scanning Electron Microscope (SEM), Energy Dispersive X-ray Spectroscopy (EDXS), to evaluate the atomic composition of the films, Raman analysis and four-point probe measurements, to explore the electrical properties, at the Micro and Nanostructured Materials Laboratory (NanoLab) of the department of Energy at Politecnico di Milano. Moreover, UV/Vis/NIR spectrophotometry measurements, for the reflectance behaviour, were carried out at the Center for Nanoscience and Technology (CNST) of the Italian Institute of Technology (IIT) in Milan. Finally, a preliminary study to assess the entity of the residual stress and the electrical properties of the films as a function of the thickness was performed, both on films deposited without ion assistance and with it.

This thesis is divided into five chapters:

- *Chapter 1* presents the results of the bibliographic research conducted. Initially, a brief description of the structure and the general properties of TiN is addressed, followed by an overview on the possible applications of this material in the field of plasmonics. Then, the chapter becomes more focused on the theme of this thesis, with detailed description of the electronic and optical properties of TiN and its characteristics as thin film, from the growth mechanisms to the Ion Beam Assisted Deposition. The paragraph is concluded by a focus on the ultrathin films and the Ion Beam Assisted Deposition (IBAD). The last two paragraphs of the chapter are an introduction to the experimental part of the thesis, as they present the results of the previous work of the research group on TiN and the objectives of my thesis.

- *Chapter 2* presents all the deposition and characterization techniques

used during this thesis. Each technique is presented with a brief description of the theoretical background and of the setup of the measurements. Where needed, a focus on the application of that particular technique on TiN is presented, to facilitate the comprehension of the experimental results.

- In *Chapter 3* a detailed description, analysis and discussion of the experimental results is presented, where needed with literature references. The chapter is divided into two sections, the first deals with the characterizations of the films, studying the effects of fluence and ion acceleration voltage, the second is focused on the thermal treatments effects. Each section is organized in sub-sections, where the results related to the single analysis technique are described and compared to the others. At the end of each section and sub-section a brief conclusion is drawn to sum up the main results.
- *Chapter 4* is the last chapter on the experimental results, and addresses the preliminary studies conducted on the residual stress and the electrical properties as a function of the thickness, with the relative conclusions.
- *Chapter 5* summarizes the results of this thesis work to highlight the main achievements and draw general conclusions. In addition, some possible perspectives are presented.

The thesis is concluded by an appendix on the fundamentals of plasmonics, where a general description of plasmonic phenomena is presented, for the sake of completeness.

1. TIN THIN FILMS: AN OVERVIEW

1.1 TiN structure and properties

Titanium nitride (TiN) has been investigated intensively over the last decades due to its durability and high versatility: its possible applications span from the use as coating material [2, 3], thanks to its gold appearance, durability and super-hardness [4], to applications as barrier layer [5, 6] or Ohmic contacts [7] in electronics. More recently, the attention on TiN has risen again dragged by the interest in its possible application in the field of plasmonics: as it will be shown in this chapter, titanium nitride shares with noble metals many electronic and optical properties, but in a lower energy spectral range, in the infrared (IR) region [8]. From a technological point of view, IR is an important portion of the electromagnetic spectrum and the conjugation with good mechanical properties is a promising starting point that may lead to interesting applications in the future years.

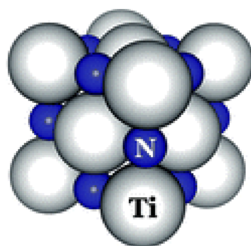

Fig. 1.1: Titanium nitride (TiN) rock-salt structure. Taken from [9].

Titanium belongs to the transitional metals of the IVb group, while nitrogen belongs to the XV group, their electronic structure is respectively $3d^2 4s^2$ and $2s^2 2p^3$. As it will be discussed in 1.3.1, most of the electronic and optical features of TiN, as well as the partial covalent character of the bonding between the two species, are related to the hybridization between Ti and N orbitals [10]. Nevertheless, the electrical conductivity is mostly given by the $Ti - 3d$ orbitals, indeed, their hybridization with the $N - 2p$ orbitals is

uncompleted leading to a partially unoccupied conduction band.
Among the various phases in which titanium nitride can be found, the most stable structure, that happens to be the more interesting for electronics application too, is the cubic rock-salt $B1-TiN$ (fig.1.1), also called $\delta-TiN$. This particular lattice configuration guarantees chemical stability, a melting point as high as 2930°C, high temperature durability [11], good abrasion resistance, high hardness, electrical conductivity, large reflectance and a gold-like yellow colour [4], making this material really appealing for many purposes, from electronics to protective and aesthetic coatings. While, as far as the crystalline structure is considered, the principal out-of-plane growth direction of the grains are [001] and [111], with the second one that seems to be associated to higher value of electric resistivity [12, 13].
Furthermore, titanium nitride is an intrinsically non-stoichiometric compound, indeed, writing its composition formula as TiN_x, it is thermodynamically stables with x ranging between 0.6 and 1.2 [14]. This means that the chemical composition may be modified easily to obtain different optical and electronic properties without modifying the structure [8]. The variation of the stoichiometry affects both the electronic density (the more nitrogen is present the less metallic is the film) and the lattice parameter a [10]. In particular, it is worth to mention that the lattice parameter is somehow linear with the content of nitrogen: it increases for sub-stoichiometric samples and decreases for over-stoichiometric. This behaviour causes the stoichiometric films to feature the highest lattice parameter ($a_0 = 0.424$ nm) [15]. However, the films stoichiometry can not be inferred by the lattice parameter since it is affected by many other factors, such as stress and oxidation phenomena.
The possibility to tune the electronic density, proportional to the square of the plasmonic frequency (ω_p), without modifying the structure of TiN, is an advantage for technological applications, with the possibility to cover a wide electromagnetic spectral range. Nevertheless, the variation of the stoichiometry is not immune to other major effects. For example, the modification of the lattice parameter changes the electronic structure of the material, affecting the optical response [10], as discussed in section 1.3.1, that must be taken into account.

1.2 Applications as plasmonic material

The long therm aim of this thesis work is the exploitation of TiN as plasmonic material in technological applications. At the moment, the most com-

mon plasmonic materials are the noble metals. However, they are unsuitable for applications in the field of telecommunications, solar energy harvesting, biology and electronics [8, 16]. Indeed, while the spectral range of interest for all these possible applications is the infrared, the noble metals feature a plasmonic frequency in the ultraviolet range. This means that the implementation of noble metals in systems that exploit the lower portion of the optical range or the infrared is almost impossible, since the interband losses are too high for any practical purpose [8]. Moreover, many noble metals suffer from chemical and thermal instability and are incompatible with the CMOS devices manufacturing, as they tend to diffuse into the silicon structures forming deep traps [8]. For these reasons, the research for alternative plasmonics materials has been very active recently. In particular, the investigations have been focused on materials with low Ohmic losses, compatibility with the silicon manufacturing and good plasmonic response in the IR spectrum, as the Transition Metal Nitrides (TMNs). Among these compounds, titanium nitride has risen considerable interest due its intrinsic non-stoichiometry, durability and cost-efficiency [2, 4, 17].

Even though most of the applications of TiN as plasmonic material are still at the laboratory level, they may potentially cover a wide range of fields. In general, the application of TiN is proposed when the working condition are particularly tough for conventional plasmonic materials [11] or the spectral range of interest is the infrared or the lower portion of the optical spectrum [16, 17].
In electronics, it is currently used as diffusional barrier layer [5, 6], nevertheless, many applications as plasmonic material are under study. For example, Guler, Shalaev, and Boltasseva in [16] reported that TiN nanoparticles are currently studied for future implementation in *heat assisted magnetic recording* to achieve higher data storage density in solid state systems. Indeed, to increase the storage density, the employment of new materials with higher magnetic anisotropy can be a feasible solution, however, this would imply the use of higher magnetic fields strength for the recording. A possible solution is to reduce momentarily the coercivity of the material through a local increase of temperature. This can be done exploiting the Localized Surface Plasmon (LSP) excitation (section A.4), shining plasmonic nanoparticles with a laser beam, allowing a sub-wavelength concentration of the electromagnetic energy. TiN is a promising material for this application thanks to its high thermal stability and hardness, moreover it would allow the use of the well-known IR laser as source of light stimulus.
Other possible applications of the plasmonic properties of TiN are in medicine. As example, a study for cancer ablation described in [16] is reported. The

basic idea is to irradiate with a laser plasmonic nanoparticles injected in the damaged cells, exploiting the enhancement effect of the local field caused by the LSP to thermally ablate the cancer. It is clear that, since it is an biological application, the materials must be non toxic. A good option is gold, however, its optical response in the biological frequency window, that is in the infrared, is poor. For this reason titanium nitride has been investigated as a valid alternative for the scope.
Furthermore, many authors [11, 18] reported that a well engineered surface morphology or hierarchical structure of TiN can lead to a wide broadband absorption, even larger than 95% for the majority of the visible spectrum, as claimed by Li et al. in [11]. This absorbance properties of TiN can be exploited in several technological applications, as water splitting processes, where it is shown that TiN permits superior performances than gold [18], or in hybrid solar-thermophotovoltaic cells, thanks to its high melting point [11]. Indeed, in this type of cells it is present an intermediate layer made by a quasi-perfect absorber that collects the radiation too low in energy to be collected by the active semiconductor. In this region the temperature may arise significantly and conventional plasmonic materials might not bear it.
A very active field in which the research on plasmonics is well established is the solar energy harvesting. In general, TiN is well suited for solar cell applications where it could be useful to increase the light harvesting in the infrared region. It can be applied both as thin film, for the exploitation of Surface Plasmon Polariton (SPP) (section A.3), or nanoparticles, to exploit the LSP. According to Atwater and Polman [19] there are mostly three different feasible configurations that allow to improve the efficiency of a solar cell using plasmonic properties. The first one, represented in figure 1.2a, exploits the sub-wavelength scattering of nanometric plasmonic particles to trap the light, permitting to reduce the thickness of the absorbing material, without affecting the efficiency, as the probability of absorbing the radiation is enhanced. The second setup is explained by figure 1.2b. To improve the absorption, this scheme take advantage of the excitation of LSP in plasmonic nanoparticles that, enhancing the local intensity of the electromagnetic field, increases the effective cross-section of the cell. The last method is presented in figure 1.2c. This setup exploits the activation of SPP modes in thin films of a plasmonic material to trap the light. These electromagnetic waves are activated at the interface between the plasmonic material and the semiconductor by proper corrugation of the active thin film, to resemble a Bragg's lattice. The idea is to guide the light along the plasmonic film to increase the optical path and improve the probability of absorption of the less energetic portion of the spectrum.

The application of thin TiN films as plasmonic material in solar cells is the long therm aim of my thesis work. However, before the application of this material, a good knowledge of its optical, electronic and structural properties is needed, as well as a good control on the deposition parameters. In particular, to exploit the plasmonic excitation, it is of utterly importance the reduction of the ohmic and optical losses. These issues will be addressed during this thesis work, with an extensive characterization of the properties of thin TiN films deposited with ion assisted room temperature PLD.

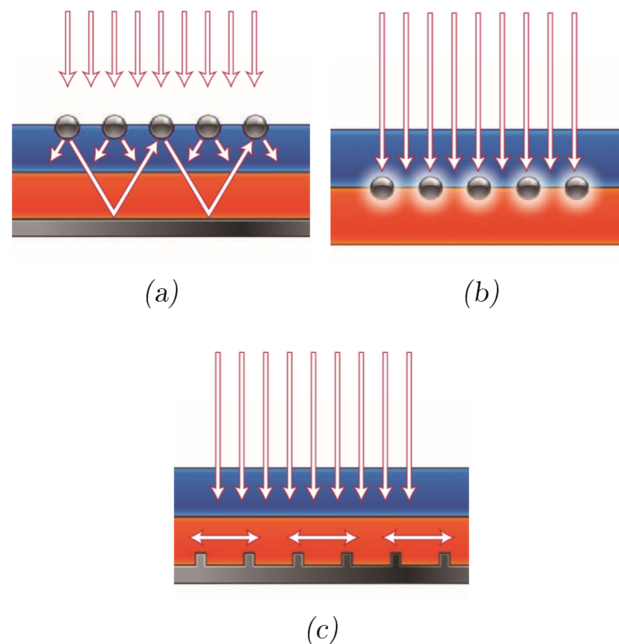

(a) *(b)* *(c)*

Fig. 1.2: Three different methods to enhance the absorption efficiency in solar cells exploiting the plasmonic properties: sub-wavelength particles for light trapping by scattering *(a)* or near-field enhancement *(b)* and nanostructured plasmonic film to increase of the optical path by coupling light with SPP modes *(c)*. Taken from [19].

1.3 Thin TiN films

1.3.1 Electronic and optical properties

As introduced in section 1.1, the peculiar electronic features of TiN are strongly related to the hybridization between the valence orbitals of titanium and nitrogen. Figure 1.3 shows the calculated Electron Density Of States (EDOS) of TiN from [20], where 0 eV stands for Fermi Energy (E_F). The strong hybridization between the $2p-$electrons of the nitrogen and the $3d$ of titanium, at the base of the partial covalent bonding of TiN, is well visible in the region below ~ -4 eV. Above this region, the states are prevalently $Ti - d$, forming the conduction band. In the region between ~ -5.5 eV and ~ -2.5 eV, where the electronic states are mainly from the $N - p$ electrons, we can identify the interband transitions manifest as two wide absorption peaks [4]. The first one, identified by the energy E_{01}, is the principal source of dielectric losses [10] and originates from the spectrum shoulder located at ~ -3.9 eV, the second one from the peak at ~ -5.6 eV. Since, the unoccupied states above E_F correspond to $d-$electrons of titanium, this means that the interband transitions are between $N - p$ orbitals and $Ti - d$ orbitals, in accordance to selection rule for optic transitions ($\Delta l = 0, \pm 1$). The cut-off energy represented in fig.1.3 defines the highest energy at which the $N - p$ EDOS gets a value different from zero. It is of great importance because it is the threshold energy at which the dielectric losses start to contribute to the optical response [10].

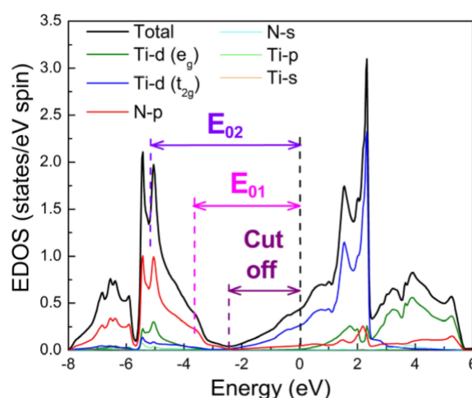

Fig. 1.3: Calculated Electron Density Of States (EDOS) of TiN. Taken from [20].

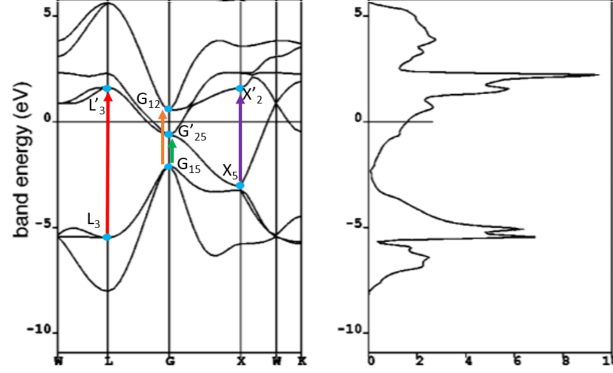

Fig. 1.4: Calculated band structure of TiN with the corresponding EDOS spectrum on the right, taken from [21]. The arrows indicating the interband transitions were drawn according to [22].

From a different point of view, the interband transitions can be defined starting from the arrows drawn on the band structure diagram in figure 1.4 from [21]. These transitions are represented by the arrows $G_{15} \rightarrow G_{12}$, at the centre of the Brillouin zone, $X_5 \rightarrow X_2'$ and $L_3 \rightarrow L_3'$ at the border of the zone, the first along [001] direction, the second along [111] [22]. They correspond to the strong interband absorptions with energy $\sim$ 3.3 eV, $\sim$ 4.9 eV and $\sim$ 6.6 eV, that originate from $E_{cut\ off}$, E_{01} and E_{02}, respectively [22]. The colour of TiN is determined by $G_{15} \rightarrow G_{12}$, being the only transition in the visible spectral range, and in stoichiometric samples is at a similar energy of those of gold, thus the characteristic bright yellow dye [10]. Nevertheless, it has to be mentioned that, as in the case of this thesis work, in nanocrystalline samples at non-cryogenic temperatures, the transitions bands are too wide and overlap to distinguish the single peak [10].

The optical response of a material is described by the complex dielectric function: $\epsilon = \epsilon_1 + i\epsilon_2$. In the case of TiN this function can be modelled using three different terms [22] (for further details on the parameters introduced in the following, the reader is addressed to sections A.1 and A.2):

$$\epsilon = \epsilon_\infty - \frac{\omega_{pu}^2}{\omega^2 - i\Gamma_D\omega} + \sum_{j=1}^{2} \frac{f_j \cdot \omega_{0j}^2}{\omega_{0j}^2 - \omega^2 + i\gamma_j\omega} \tag{1.1}$$

the first term accounts for high energy response, that will not be further described but using a generic positive ϵ_∞. The second is the Drude term,

for intraband transitions, where ω_{pu} is the unscreened plasma frequency ($\sim$ 6.9 eV for a stoichiometric TiN film [4]) that characterises the metallic behaviour of the material and Γ_D the damping factor. The sum represents two Lorentz oscillator to account for interband transitions E_{01} and E_{02}. For each $j-$oscillator f_j represents the respective strength, γ_j the damping factor (or broadening factor) and ω_{0j}^2 the characteristic frequency, thus the energy of the transition. When all the contributions are considered, thus both the metallic and dielectric behaviour of the material are taken into account, the frequency at which $\epsilon_1 = 0$ does not corresponds to ω_{pu}, but to the so called screened plasma frequency (ω_{ps}). This frequency red-shifts as the nitrogen content increases [23], since the energy at which $\epsilon_1 = 0$ decreases. In figure 1.5 it is presented a simulation of the model just presented from [10]. The red line represents the dielectric function of a TiN stoichiometric sample with B1 structure as sum of the Drude contribution (magenta dotted line) and the collective Lorentz contribution (red dotted line). First of all, it is clear that the dielectric function of TiN shows a metallic behaviour, with ϵ_1 that assumes negative value. Moreover, in contrast to noble metals, like gold, that

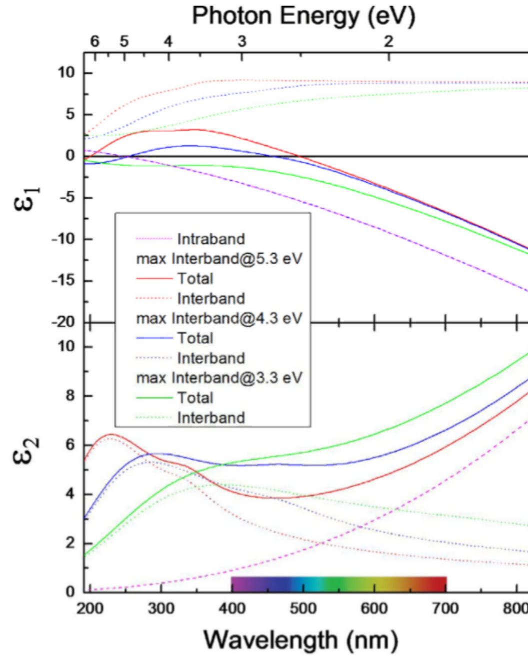

Fig. 1.5: Simulation of the real (ϵ_1) and imaginary (ϵ_2) part of TiN dielectric function showing the effect of different extent of overlapping between Lorentz (interband) and Drude (intraband) contributions to the model. The red line is referred to $1:1$ $B1-TiN$. Taken from [10].

feature ω_{ps}^2 in the ultra-violet range, TiN screened plasma frequency takes value in the visible range, at ~ 2.65 eV for a stoichiometric film [24], opening up to many different applications in the low energy spectrum, as discussed in section 1.2.
One of the main parameter that may affect the dielectric function, thus the optical response of TiN, is the stoichiometry. In particular, it modifies the extent of overlapping between the interband and the intraband contribution. For example, in figure 1.5, the blue and green dotted lines represent hypothetical Lorentz contributions lower in energy and more overlapping with respect to those related to the stoichiometric film, that generate two new ϵ_1 and ϵ_2 functions. With respect to the stoichiometric film, the ϵ_1 function represented by the blue solid line crosses crosses the zero line with a less steep slope, while the green one does not event features a crossing point, at least in this spectral window. On the other hand, the resulting ϵ_2 functions feature higher value in the visible range, hence higher optical losses. These functions resemble those for Ti and Ti_2N and make clear the optimal optical behaviour, with less overlapping interband and intraband transitions, of $Bi - TiN$ with respect to other phases[10].
Titanium nitride rock-salt phase is thermodynamically stable even changing the ratio between titanium and nitrogen, in particular, the more titanium is present the higher is the electronic density (n), since the number of $d-$electrons increases [10]. The electronic density is strictly correlated to the unscreened plasma frequency (section A.1), in particular ω_{pu}^2 increases linearly with n. In other words, increasing the nitrogen content, the metallic character is reduced and the plasma frequency red-shifted. As a matter of fact, ω_{pu}^2 influences ω_{ps}^2 [4] and, indeed, its value is considered a reliable parameter to asses the stoichiometry of TiN, where samples with $1:1$ nitrogen to titanium ratio present $E_{ps} = 2.65$ eV [24]. This value is in the visible range, meaning that the colour of the sample will be influenced directly by it. When TiN becomes over-stoichiometric the plasma frequency red-shifts, giving a reddish brown dye to the sample [10].

Patsalas and Logothetidis in [22] studied further the modification of the optical properties introduced by the variation of the stoichiometry. Indeed, besides the electronic density, the stoichiometry effects also the cell size (section 1.1), modifying further the optical properties. In fact, this effect, together with the variation of the cell size caused by the internal stress state, alters the Brillouin zone and, consequently, the symmetry of the crystal cell and the electronic structure. These variations directly affects the interband transitions, represented by the Lorentz terms in the dielectric function, and consequently the energy of the oscillators ω_{01} and ω_{02}, as explained in figure

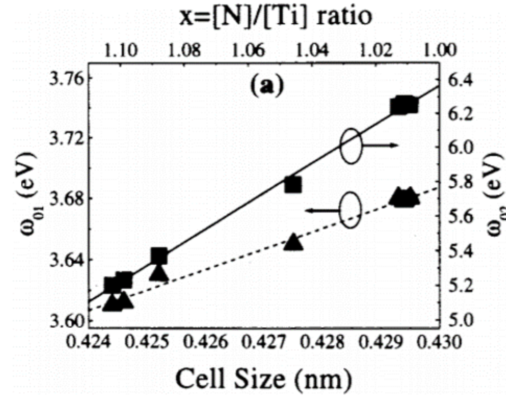

Fig. 1.6: Dependence of the interband transition frequency ω_{01} and ω_{02} on cell size and stoichiometry. Taken from [22].

1.6. According to Patsalas and Logothetidis [22], one of the most sensitive parameter to structural changes is γ_j, that determines the broadening of the Lorentz oscillators. Its behaviour is quite complicated to be analysed and seems to depend on many parameters, such as: defects, stoichiometry, grains size and orientation. In general, γ_1 was reported to decrease and γ_2 to increase as the cell size and stoichiometry were augmented, showing a monotonous, but not linear, behaviour. Their dependence on the grains size and orientation is more complicated. The interband transitions occur along defined direction of the Brillouin zone: L transitions along [111] direction and X along [001] (fig. 1.4). So, the higher is the volume fraction of the grains [002] oriented, the more $X_5 \rightarrow X_2'$ transition is strong and, vice-versa, for [111] oriented grains and $L_3 \rightarrow L_3'$ transition. This causes a variations in the contribution in eq.1.1 of the two oscillators, represented by a modifications in f_{01} and f_{02}.
To evaluate the total effect on the dielectric function, the variations of the Drude part of the model should be taken into account too, considering the variations of the intraband transitions. In particular, the affected variables are ω_{pu} and Γ_D, the first depends strongly of the conduction electronic density and, thus, on the stoichiometry, while the second, being the damping factor, depends on grain boundaries, defects and in general on the mean free path of the electrons.
As example, the case of two 100 nm TiN films deposited by reactive sputtering is reported in figure 1.7 from [4], highlighting the effect of the variation of the sputtering bias. It is evident that to a higher bias corresponds a blue-shift in ω_{pu}. Indeed, in this case, higher momentum of the impinging

particles favoured [002] direction, forcing f_2 to increase, with an overall effect of shifting upward the L_2 blue line and the whole graph. Moreover, higher energy particles guaranteed a more stoichiometric film, with higher carrier density and larger cell size, resulting in a blue-shift of ω_{pu} (D blue line), ω_{01} and ω_{02} (L_2 blue lines). Furthermore, the higher bias favoured a more crystalline and denser film, resulting in a higher mean free path and a smaller Γ_D, highlighted by the steeper D blue line.

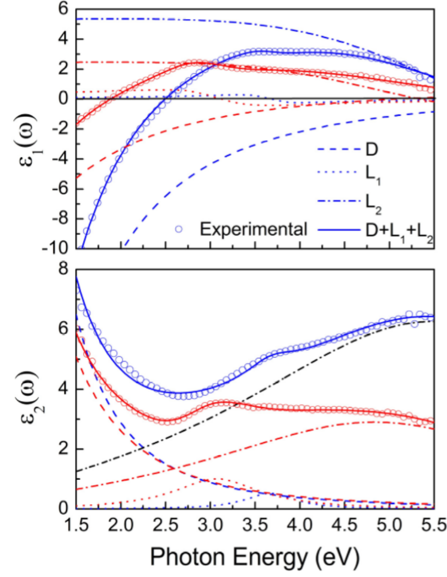

Fig. 1.7: Experimental dielectric function (circle) showing real (ϵ_1) and imaginary (ϵ_2) part of two 100 nm thick film obtained by sputtering with $V_b = -40$ V (red) and $V_b = -120$ V (blue). The dotted and solid lines are the theoretical fitting from eq.1.1 of Drude (D) and Lorentz (L_1, L_2) contributions. Taken from [4].

The electronic features of the film are strictly connected to the optical properties. Indeed, Patsalas and Logothetidis in [22] proposed a straightforward evaluation of the electronic mean free path and the resistivity from ω_{pu} and Γ_D, with the possibility to compare these results with to grain size, obtaining important information on the electron scattering phenomena.
To evaluate the mean free path (L_g), it is possible to use the following expression that relates it to the Fermi velocity (v_F) and the relaxation time ($\tau_D = \hbar/\Gamma_D$):

$$\frac{1}{\tau_D} = \frac{1}{\tau_{bulk}} + \frac{v_F}{L_g} \tag{1.2}$$

where τ_{bulk} is the bulk relaxation time. Since in nanocrystalline materials $\tau_{bulk} \gg \tau_D$, this term can be neglected, giving: $L_g = \tau_D v_F$. As far as the Fermi velocity is concerned, it is possible to use the free electron model corrected by the effective mass (m_e). In the case of TiN, m_e is between ~ 1.1 and ~ 1.4 times the electron mass [22, 25, 26]:

$$v_F = \hbar \left(\frac{3\pi^2 \epsilon_0}{(m_e e)^2} \right)^{1/3} \cdot \omega_{pu}^{2/3} \tag{1.3}$$

Once all this quantities are known, the mean free path can be compared to the grain size obtained from direct observations (i.e. X-Ray Diffraction, XRD). The mean free path is expected to increases with the grains size since the grain boundaries are an unavoidable major source of scattering. Thus, it should improve with deposition temperature, annealing steps or other processes that somehow favour bigger grains. On the other side, vacancies and defect increase the scattering probability, hence reducing the mean free path. Some defects are always present in the film, but they are increased by oxidation and strain, and, vacancies may form in sub- and over-stoichiometric films, but, in general, are intrinsically present in TiN.
If the mean free path is shorter than the grain dimension means that most of the electrons are not scattered by the boundaries, but by some defect inside the grain. In the study of Patsalas and Logothetidis [22], the samples that feature a short mean free path are those not stoichiometric, but the difference from the grain size is small enough to suggest that the vacancies are more concentrated closer to the boundaries.

The resistivity (ρ) of the film depends on the carrier mobility (μ) and carried density (n), following this equation:

$$\rho = \frac{1}{n\mu e} \tag{1.4}$$

Since the mobility is affected again by the mean free path, that is intimately connected to the damping parameter (Γ_D), and the carrier density to ω_{pu}, it is clear that any variation in resistivity is well evident in the optical response, and vice versa. As reference, typical values for the resistivity in TiN are in the range of 6×10^2 µΩ cm [22] and 10 µΩ cm [25], while the mobility is approximately between 0.4 cm/V s, measured for a non reactive sputtering film by Yu et al. in [27], and 36 cm/V s, reported by Xiang, Liu, and Zhang [28] for heteroepitaxyal PLD TiN deposited with substrate heated at 700°C.

1.3.2 Film growth and residual stresses

Titanium nitride is a highly versatile material that can be deposited with a wide range of deposition methods, both physical and chemical deposition based, maintaining the stable $B1-$structure. The most cited in the literature are: Magnetron sputtering [29, 30], Cathodic Vacuum Arc [31, 32], Atomic Layer Deposition [33, 34], Chemical Vapour Deposition [35, 36] and Pulsed Laser Deposition (PLD) [37, 38], the technique used during this thesis work. Since the main applications of TiN imply the deposition of films on different substrates, the knowledge of the internal stress state and the understanding of how the material grows during the deposition are of paramount importance. The internal stress state in the film results from a superposition of effects related to the presence of defects, the growth mechanism, the deposition process and the microstructure of the film [10]. The presence of residual stress in the films may deeply affect the adhesion to the substrate, the integrity of the sample and, since they are often related to defects, even the electronic and optical characteristics. Thus, it is important to understand the origin and try to minimize the formation of the internal stress.
Besides the residual stress, it might be interesting to have some control on the direction of growth of the grains too. As discussed in section 1.1, we are interested in the direction [001], that shows lower electric resistivity. In this perspective, an interesting feature reported by many groups [39–42] is the presence of a cross-over in the grains orientation during the growth of TiN films: while at the beginning of the deposition the grains are oriented in [001] out-of-plane direction, after a threshold thickness, the prevailing direction becomes [111].

Structure Zone Model (SZM)

To understand and predict the growth mechanism and the structure of thin film obtained through Physical Vapour Deposition techniques, it is possible to use the Structure Zone Model (SZM). This model, introduced in 1969 by Movchan and Demchishin [43], relates the structure of polycrystalline films to the homologous temperature $T_h = T_s/T_m$, where T_s is the substrate temperature and T_m the melting temperature of the deposited species. In this initial model only three zones were accounted. The first one, for $T_h < 0.3$, due to the low temperature is characterized by negligible adatom mobility, resulting in a columnar morphology with voided boundaries. The second zone, confined between $T_h = 0.3 - T_h = 0.5$, is still columnar, but the grains are now

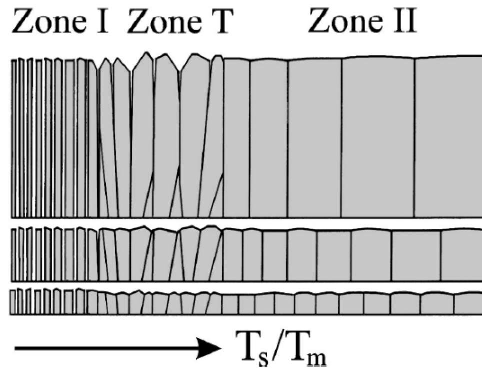

Fig. 1.8: Schematic representation of the grains structure in the first three zones of the *Structure Zone Model*. Taken from [44].

separated by metallurgical boundaries and bigger, because the surface diffusion is now considerable. In this situation the growth direction is governed by the minimization of the surface energy. The third zone is reached when the temperature increases further and it is characterized by larger grains, favoured by the activation of the bulk diffusion.
However, this model was not enough to cover all the possible cases encountered, for this reason Thornton [45] introduced a supplementary zone between the first and the second called *zone T* (fig.1.8), characterized by poorly defined fibrous grains. In this region, roughly contained between $T_h = 0.2 - T_h = 0.4$, the surface diffusion, already considerable, is limited by the competitive process of grain growth until a prevailing direction is defined, thus the shape of the grains is faceted and not entirely columnar, resembling a V.
Even if the *SZM* is a powerful tool, it is not suitable for deposition processes that feature high energetic particles. For this reason, the model was extended to other deposition methods, as sputtering and PLD, taking into account also the effects of plasma and ions. For example, Anders in [46] replaced the homologous temperature with an effective one ($T^{\star}$) considering the potential energy of the impinging particles (e.g. heat of sublimation, cohesive energy and ionization energy) and the pressure with a logarithm scale of a normalized energy ($E^{\star}$), combination of thermal and kinetic energy of the particles. The scheme obtained is presented in figure 1.9. According to this scheme, being the kinetic energies reached during a PLD deposition of some tens of electronvolt [47], and considering the substrate at 300 K, thus $T_h \sim 0.25$, it is likely that the growth of TiN films during a room temperature PLD deposition is completed under *zone T* conditions.

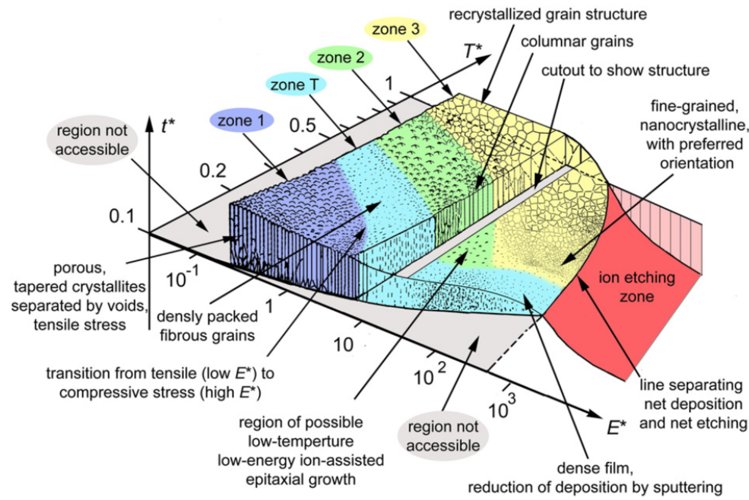

Fig. 1.9: Extended *SZM* taking into account energetic particles through a generalized temperature $T^{\star}$ and a normalized energy $E^{\star}$. Taken from [46].

Residual stresses

The residual stress reported in literature for thin TiN films deposited by sputtering and PLD are usually compressive of few GPa [39, 41, 42, 48]. Some of the possible origins of this type of stress state have been summarized by Patsalas et al. in [10], where it has been studied how the stress state can be modified changing the parameters during a reactive sputtering deposition of TiN from a titanium target. In particular, in this study, it is reported that the internal stress state can be modified varying the flow of the nitrogen that enters in the chamber or increasing the bias voltage. In the first case, it is observed a shift from compressive to tensile as the flow of nitrogen is decreased (fig.1.10), while, in the second, the resulting higher energy of the impinging particles causes the stress to become less tensile. Finally, they concluded that the residual stresses in these films are mainly related to the sum of two different contributions: a tensile component due to the attraction between columns, that increases with thickness, and a compressive contribution due to the bombardment of the film by energetic particles (*atomic peening* effect). This latter effect may create defects in the sub-surface region when

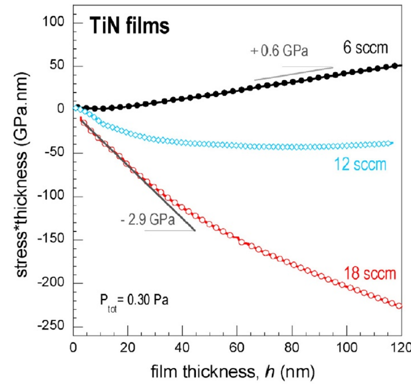

Fig. 1.10: Stress evolution of reactive sputtering TiN films as a function of the thickness depending on the nitrogen flux. Taken from [10].

the incoming particles exceed the *subplantation* energy. This energy, in the case of TiN, is roughly $\sim$ 50 eV [10], a value easily reachable during sputtering and PLD depositions [47]. Even if the experiments were conducted using reactive sputtering deposition, the main principles are rather general and could be consistent for other deposition techniques, such as PLD, since the films were grown under *zone T* conditions of the *Structure Zone Model*. In the same review [10], Patsalas et al., specified that additional compressive stress may result from the accumulation of defects in the grain boundaries, the preferential site for the formation of vacancies, substitution or other type of defects, as the incorporation of bigger interstitial atoms. The accumulation of such high number of defects leads to an in-plane state of compressive stress. It is thus clear how easily the overall stress state becomes compressive, as observed in the vast majority of literature on TiN.

An important role in the determination of the stress state in the films is played also by the growth mechanism. There are basically three different types of film growth: *(i) Frank-Van der Merwe* where the material is deposited layer by layer; *(ii) Volmer-Weber* in which the growth of the films starts at some enucleation points (islands), that eventually coalesce (fig.1.11). It is a very common mechanism for deposition on dissimilar materials [49], especially for metal films when the superficial mobility of the adatoms is low, as in the case of titanium [50]; *(iii) Stranski-Krastanov* where the film initially grows layer by layer then, due to the accumulated strain, continues with the formation of islands.
In literature many works observed that the growth of TiN films deposited via

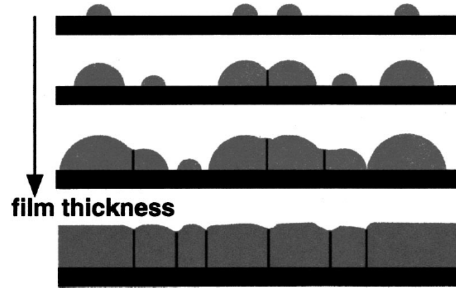

Fig. 1.11: Scheme of *Volmer-Weber* growth mechanism. Taken from [50].

reactive sputtering is discontinuous up to a coalescence thickness [23, 25, 51]. A 3-D islands growth characteristic up to a few nanometers has been reported even for TiN films obtained by Atomic Layer Deposition (ALD) [52]. However, up to now, no one has submitted studies of the initial growth behaviour of TiN films deposited by PLD. The presence of a threshold thickness for the coalescence of the islands is a consequence of the *Volmer-Weber* growth mechanism [23]. This type of growth is related to a well-defined and characteristic evolution of the residual stresses, from compressive to tensile and then compressive again as the film thickness increases (fig.1.12) [50, 53, 54]. This characteristic trend is rather general because it results from the superposition of two common mechanisms, as explained by Floro et al. in [50]. In this study it was observed that the thin films of silver, aluminium, titanium and germanium, deposited via electron beam evaporation on SiO_2, showed the same compressive-tensile-compressive behaviour typical of the *Volmer-Weber* growth. They justified the observations considering separately two different sources of internal stress. The first one is the island coalescence, associated with the formation of grain boundaries, that implies the generation of tensile stress. The second ons, is the capillarity induced stress during the island growth, that may develop either before and after the islands coalescence and are compressive. This stress is a consequence of the interaction between film and substrate, that prevents the lattice parameter from adjusting itself to the equilibrium value. The superposition of these two effects determines the stress evolution in the film, with a tensile peak associated with the islands coalescence process (fig.1.12). Moreover, in the same paper it was shown that this growth mechanism does not depend on the crystallinity, as, for example, amorphous germanium follows the same stress trend.
In conclusion, even if a study on the growth mechanism of TiN during a PLD deposition has never been done, the expected growth mechanism of TiN is *Volmer-Weber* as it was reported reported for other deposition techniques.

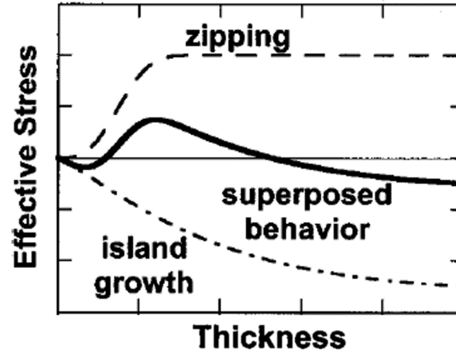

Fig. 1.12: Simulation of the stress trend in a *Wolmer-Weber* growth, the tensile peak is associated with the formation of grain boundaries related to the islands coalescence. Taken from [50].

Indeed, it is a very common growth mechanism, often featured when the surface mobility of the deposited species is not particularly high.
To validate this hypothesis, during this thesis work an investigative study on the stress state of TiN PLD films as a function of the thickness was carried out, the results are presented in section 4.1.

1.3.3 Grains growth orientation

In titanium nitride films, an anisotropy in the Young's modulus between [111] and [001] crystalline out-of-plane growth directions is observed. This difference causes the first direction to features a lower strain energy and the second a lower surface energy [55]. The anisotropy in the Young's modulus was used to explain the preferential growth direction and, in particular, the reason why it changes during the growth of the film, by many authors [42, 56]. Chen, Yu, and Huang in [56] modified the state of stress in hollow cathode discharge ion plated stoichiometric TiN films by biasing the substrate (between ~ 3 V and -300 V) to control the energy of the impinging ions. Initially, a [001] growth direction was observed, followed, as soon as the stress level increased, by a prevailing [111] growth direction. As anticipated, this result was explained using the anisotropy in the Young's modulus, since the out-of-plane [111] preferential growth direction minimizes the strain energy level in the film. Also Oh and Je in [42] justified the different growth direc-

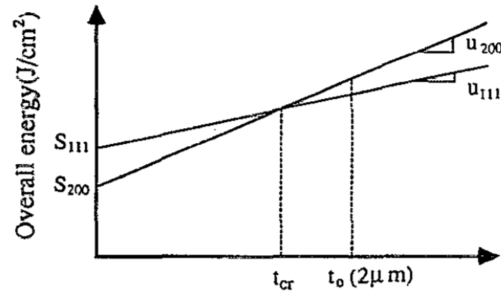

Fig. 1.13: Dependence of the strain and surface energy on the film thickness. The threshold thickness is indicated as t_{cr}. Taken from [42].

tions observed in a Plasma Enhanced Chemical Vapour Deposition (PECVD) and in a reactive magnetron sputtering TiN film with the anisotropy of the Young's modulus, but with a focus on the role of the surface energy. Both films were 2 μm thick, the PECVD sample was deposited at 400°C, while the sputtering specimen at room temperature. The orientation of the grains was measured in-situ, to detect any possible variation of the growth direction during the deposition. The PECVD film showed grains oriented preferentially along [002] direction during the whole duration of the fabrication process. This out-of-plane growth direction was explained with the minimization of the surface energy. In fact, the PECVD deposition implies low momentum of the impinging particles, thus lower stress level in the film, and an increased surface mobility of the deposited species thanks to the higher deposition temperature. On the other hand, the sputtering films reported an initial [001] growth direction, followed by [111] orientation. In this case, due to the higher momentum of the impinging particles and the lower deposition temperature, it was assumed that the accumulation of strain proceeded linearly with the thickness. Thus, while, at an initial deposition stage, the surface energy minimizations prevailed and [001] direction was favoured, at a certain threshold thickness, the driving force became the strain energy and [111] orientation took over (fig.1.13).
Some years later, Abadias, Tse, and Guérin [41], studied the stress in stoichiometric TiN films deposited by reactive magnetron sputtering from a Ti target on a Si substrate with ion beam assistance of Ar and N_2 with acceleration voltage between 25 and 150 V. They observed that in their samples the [111] direction presented higher residual stresses with respect to [001], an observation that was considered inconsistent with the idea of strain energy minimization. For this reason, they ascribed the change in the growth

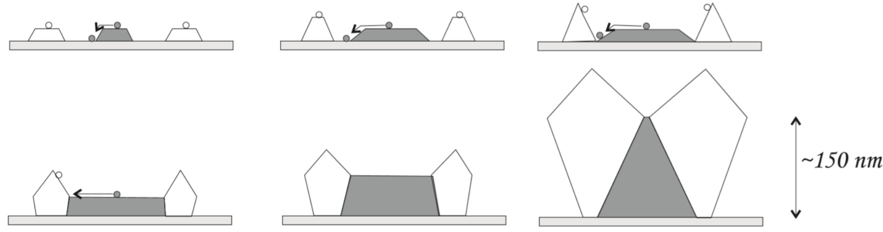

Fig. 1.14: Evolution and stages of TiN film growth under *zone T* conditions. Dark grains are [002] oriented and white grains [111] oriented. Taken from [57].

direction to a renucleation mechanism favoured by the high defect density and the ion bombardment. Even though this explanation applies only to this specific case, it is clear that the energy equilibrium argumentation may be incorrect or, at least, not enough to explain the change in growth direction. Indeed, later on, Mahieu et al. [40, 57] presented a more general model that explains the preferential orientation of TiN in the *zone T* of the *structure zone model*. This model, based on the models for the metals, is particularly suited for a reactive sputtering deposition, but can be cautiously extended to other techniques, as far as the deposition is carried out under *zone T* conditions.

The general idea is the existence of a geometrically fastest growing direction that, since the grains that feature this orientation expand faster at the expense of the others, once a threshold thickness is reached, prevails (fig.1.14). This direction depends on the crystal habit of the material, determined by the crystallographic plane with the slowest perpendicular growth. This plane, that can be found identifying the plane that offers the lowest number of nearest neighbours, depends on three parameters: the lattice structure, the composition of the impinging particles and the state of the reactive gas, namely if it is composed by atoms or molecules (compounds); the role of these parameters is summed up in table 1.1. Considering the case, represented in figure 1.15, of a titanium target sputtered in presence of a N_2 atmosphere, thus with atomic adparticles and molecular gas, the slowest perpendicular growth rate is featured by $\{001\}$ plane. Thus, the grains will be than faceted $\{100\}$ (looking from the top) and the fastest growing direction will be [111], as can be seen in the middle section of figure 1.15. In this particular case, the grains with out-of-plane [002] growth orientation have the slowest perpendicular growth, but, on the other side, they feature the highest lateral growth. Thus, the growth of the TiN film could be, thus, divided into two different stages, as it is shown in figure 1.14. Initially the film presents a

Tab. 1.1: *TiN* growth direction depending on adparticles and reactive gas composition in a magnetron sputtering deposition. Taken from [40]

Structure	Adpart.	Reactive gas	Number of nearest neighbours on:			Crystal habit	Fast. geom. growth dir.
			{100}	{110}	{111}		
Rocksalt	Atomic	Molecular	1	2	3	{100}	[111]
	Atomic	Atomic	5	4	3	{111}	[001]
	Comp.	Molecular	2	4	3	{100}	[111]
	Comp.	Atomic	2	4	3	{111}	[001]

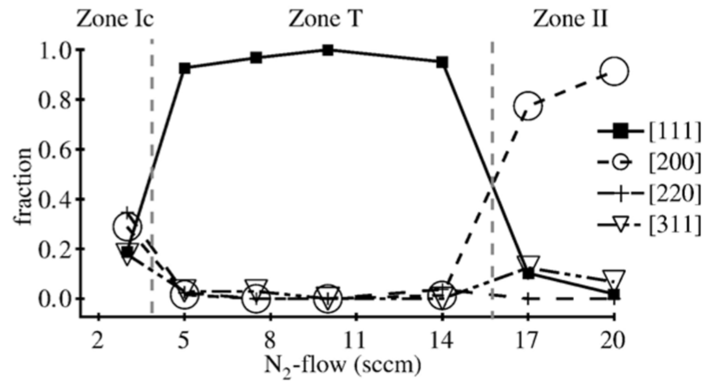

Fig. 1.15: Out of plane growth direction of the grains (volume fraction) depending on the N_2 reactive gas flow that modify the sone of the *SZM* under which the deposition is carried out. Taken from [40].

predominant [001] growth direction, than, since [111] oriented grains grow geometrically faster, the film will present a predominant [111] out-of-plane orientation. Arguably there is a sort of threshold thickness at which this transition happens. This thickness is not fixed, it changes depending on the experimental conditions, but it can be estimated in ~ 150 nm [57].
It is very difficult to understand whether this model is suited for a PLD deposition or not. Indeed, in a reactive sputtering deposition the target is made of titanium. Hence, a metal-based model is more easily accommodated for the purpose. While, in the PLD used for this thesis, the target was made of TiN, consequently the nitrogen plays a more important role in the deposition. Nevertheless, since the deposition conditions are likely to be comparable to those of the *zone T*, it is possible that the mechanism is similar to the one described in this model.

As anticipated, it may be interesting to obtain films that feature a preferential [001] direction, but, so far, there are no studies which have demonstrated that the threshold thickness can somehow be avoided in sputtering and PLD depositions. Nevertheless, some specific arrangements during the deposition may help to increase the fraction of [002] oriented grains or shift the crossover thickness.
Patsalas, Gravalidis, and Logothetidis in [58] summed up three methods to achieve this goal in a sputtered film. The first is to improve the mobility of the adatoms, as a matter of fact, this would favour the [002] oriented grains since they feature the highest lateral growth. While, the second and the third imply the modification of the intrinsic stress or the management of the strain energy. Focusing on the PLD, Lackner et al. [39], depositing TiN films at room temperature, assumed that particles with a high kinetic energy may improve the mobility on the surface, thus favouring [001] orientation. They also suggested that the ion bombardment, at which the film is naturally subjected during the deposition, would favour [111] direction due to the additional deformation strain caused by the penetration of these particles. In fact, another way to modify the growth direction is to use an assistance ion source that strikes the growing film. However, there is not general agreement in literature on the effectiveness of the method and to what extent the [111] direction is favoured. This particular method will be addressed more in detail in section 1.3.5. Even though, the observations of Kim et al. in [59] suggest that a better way to improve mobility in a PLD process would be a combination of thermal energy and kinetic energy of the particles. Indeed, they observed that the best crystallinity and the highest fraction of [002] oriented grains were obtained with a deposition carried out at 450°C. While, increasing the pressure in the chamber, thus decreasing

the momentum of the particles, the film showed only [001] direction, but an extremely low crystallinity too.
In general, it is clear, that, to improve the crystallinity and the volume fraction of [002] oriented grains, the more straightforward way is to increase the substrate temperature during the deposition. Nevertheless, it was pointed out that high energetic particles and ions may sort some effects on the growth orientation, but the results are debatable. The exploration of this possibility is one of the objectives of this thesis, that will try to shed some light on the role of the assisting ions on the compositional and structural properties of thin PLD TiN films.

1.3.4 Oxidation of TiN

A major issue to be considered for the deposition of TiN films, or during additional thermal treatments, is the oxidation. Indeed, the affinity of titanium with nitrogen is actually lower than the one that it has with oxygen [60]. This means that it is necessary to avoid any oxygen impurity during the deposition. Moreover, even to increase the deposition rate or to exploit the bombardment with ions may help to reduce the extent of oxidation. In fact, the use of assisting ions should reduce the porosity, that may trap residual gasses and, in general, should favour $N-Ti$ bonds at the expense of the oxygen [61]. The effects of the ion assistance will be further analysed in section 1.3.5.
After the deposition, the oxidation of the film may continue when exposed to air or during some heat treatments. The kinetic of the oxidation reaction of TiN was experimentally found by Tompkins [62] to be $y^2 = kt$, where y is the penetration depth, t the time and k the rate constant that depends on the temperature following an Arrhenius law. It is, thus, evident how the temperature heavily determinates the speed and the extent of oxidation. At room temperature, independently from the oxygen pressure, only an unavoidable superficial oxidation is reported, with the formation of Ti_2O_3 or TiO_2 [63]. To have oxygen diffusion towards the bulk, higher temperatures are needed. The temperature at which this process starts does not seem to depend on the pressure and it is in the order of a few hundreds of Celsius degrees, 250°C according to Glaser et al. [63]. When the oxygen starts to diffuse into the bulk, an intermediate layer of oxynitride separates the titanium oxide surface layer and the bulk titanium nitride [62–64]. Moreover, during the formation of the oxide phase, some N_2 molecules may appear on the surface due to the

reaction: $TiN + O_2 \rightarrow TiO_2 + (1/2)N_2$ with possible outgassing of nitrogen [62, 65].
Thus, it is clear that, once the film is deposited, the passivation of the surface prevents any further oxidation at room temperature. However, if the temperature reaches a few hundreds of Celsius degrees, the oxidation of the film may proceed further. Hence, it is important that any successive thermal treatment is performed under controlled atmosphere, without any possible oxygen impurity.

1.3.5 Ion Beam Assisted Deposition (IBAD)

To modify the compositional, structural and crystalline properties of the samples, the growing film is often bombarded by an ion beam. This technique is called Ion Beam Assisted Deposition (IBAD) and it is commonly applied to improve the characteristics of the fabricated film. The parameters of the beam that can be controlled are the ion species, the current, i.e. the number of ions colliding with the sample per unit time, and the kinetic energy of the ions. On the other hand, the film properties changed by the assisting ion beam are those related to residual stress, crystallinity and stoichiometry [41, 66–68].
Zhang et al. [67], using a flow of 1.5 $sccm$ of N_2 and 0.5 $sccm$ of Ar to supply the ion source, found that the crystallinity is improved when a certain equilibrium between current and energy of the ions is found. Fixing the ion energy at 200 eV, the best improvement was achieved with 4 mA, while, going up to 500 eV, the film showed a lower enhancement at the same current (fig.1.16a and 1.16b). In a subsequent article of the group [66], the highest value of crystallinity was obtained for energy values of 100 and 200 eV with a flux of N_2 and Ar (1.2 $sccm$ and 0.2 $sccm$) and a current of 10 mA, in agreement with the previous observations. Thus, it is evident that an excessive ion bombardment, both in energy or in current, may cause too many dislocations and defects, reducing the overall order of the film. This effect is particularly evident if the threshold energy for atomic displacement is overcame ($\sim$ 25 eV for TiN [10]). Furthermore, in both the articles, [111] crystalline direction is by far the most favoured by the ion assistance, while direction [002], already barely visible in normal depositions, is often abstent in films deposited with assisting ions. However, on this last point, there is not agreement among the authors: Abadias, Tse, and Guérin in [41], studying the effect of $Ar - N_2$ assisting ions (both fluxed at 1 $sccm$), showed that both [111] and [001] XRD

peaks got higher changing the acceleration voltage from 25 V to 150 V and maintaining the current fixed at 80 mA (fig.1.16c). Nevertheless, it was found that the thickness at which the ratio between the intensity of the [111] peak and the intensity of peaks of all the other directions assumes the same value that would have had in a reference TiN powder, shifted upward as the ion energy was increased (fig.1.17). In other words, the [111] crystalline orientation was favoured as the energy of the assisting ions was enhanced. However, even if the crystallinity seemed improved, the ion bombardment resulted in a rougher surface and grain coarsening at 150 eV due to resputtering of particles from the film. Comparing the works of Zhang et al. [66] and Abadias, Tse, and Guérin [41], it may be hypothesized a correlation between the ratio of argon and nitrogen ions, the current and the increase in the intensity of [111] XRD peak, but the deposition conditions were rather different and the information not enough to make a reliable comparison.
In addition to the grains orientation, Abadias, Tse, and Guérin in [41] extensively studied the residual stresses introduced by the bombardment. In general, the assisting ions created point or cluster defects inducing a lattice expansion. This phenomena resulted in a hydrostatic stress, that appeared to be higher along [111] direction, with a related biaxial in-plane component that featured a well negative value between -5.5 and -8 GPa.
These changes in the structural and morphological features affects the electrical and optical properties too. In fact, Zhang et al. in [66] reported a monotonic increase of the resistivity, as the assisting ions energy was enhanced, explained with the enrichment effect of the impinging nitrogen atoms, that made the film over-stoichiometric, reducing the carrier density. Moreover, they also hypothesized that the films changed morphology, passing from layered to columnar, thus increasing the number of grain boundaries and thus the resistivity. The effect on the optical properties is strictly correlated to the electronic ones. Indeed, the red-shift in the plasma frequency, described by Zhang et al., can be explained with the decrease in the electronic density.

The effect of the ion bombardment is well visible on many properties of the films. Indeed, besides the introduction of defects, also the stoichiometry, the electrical and the optical properties are affected. The management of these effects can be very useful in the exploitation of TiN in the plasmonic field. Indeed, the ability to tune the optical response of the material may guarantee a very high versatility, covering the requirements of many different technological applications, from the low energy optical range to the near infrared.

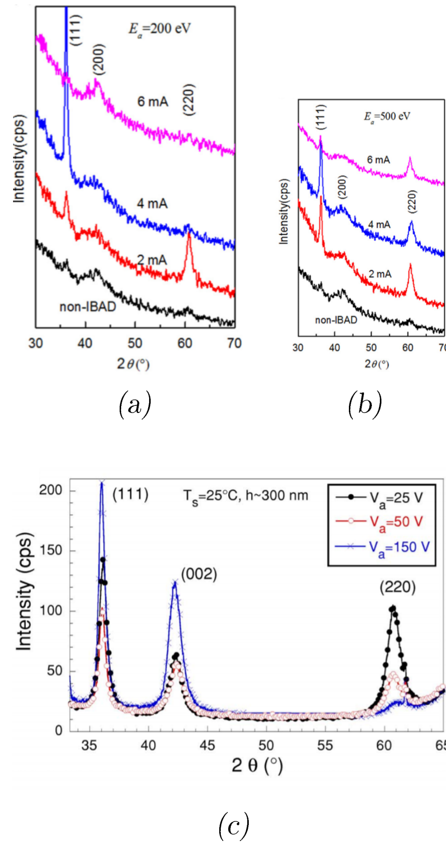

(a) (b)

Fig. 1.16: XRD spectra of TiN films deposited with different assisting ions energy and current. (a) and (b) taken from [67], (c) taken from [41].

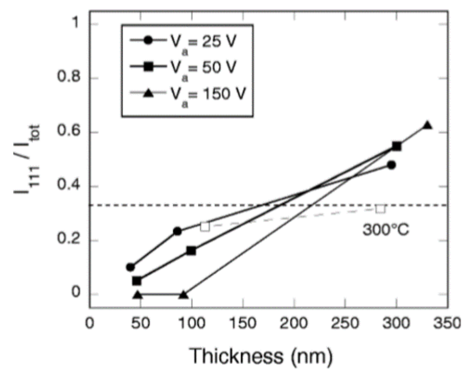

Fig. 1.17: Intensity ratio between the XRD peak associated to the [111] crystalline direction and all the other (I_{111}/I_{tot}) as a function of the accelerating voltage (V_A) applied to the ions. The dotted line represents the expected intensity ratio in a TiN reference powder. Taken from [41].

1.3.6 Ultrathin TiN films

To exploit the enhancement of the light-matter interaction caused by the appearance of quantum effects [26], the dimension of the system, thus the thickness of the film, must be decreased to few nanometers, in particular somewhat below 10 nm [26]. However, reducing the thickness of the films, many properties are largely affected and the deposition becomes rather complicated. Indeed, deposition temperatures of some hundreds Celsius degrees and specific substrates that features a rock-salt structure and a reticular parameter close to TiN, e.g. MgO, are often needed [25, 26]. The resulting conditions allow to approach almost epitaxial growth, achieving depositions of very regular single crystal films, with low superficial roughness and continuity already at very initial stages. For example, Ingason et al. [51], in a deposition through reactive sputtering on thermal silica at 650 °C, reported coalescence thickness at ~ 2.2 nm.

When it comes to consider the effect of the thickness reduction, the most important parameter is the electron mean free path (λ). In fact, most of the properties of the film show remarkable modification as soon as the film thickness approaches the mean free path [26]. Indeed, the decrease of the thickness determines an increase in the surface to volume ratio, that is reflected in an enhanced contribution of the surface scattering, determined by the higher defects density, the presence of an interface and the unavoidable oxidation. In fact, the interaction with substrate, at the bottom surface, and, with the defects created by the atomic oxidation, at the top, results in a surface scattering roughly completed diffusive in nature [25, 51], hence inelastic. Moreover, the overall increase of defects has the effect of reducing the carrier density [26]. The total result of these variations is a general decreasing of the mean free path and an increase of the resistivity, well visible in figure 1.18 below 10 nm, where the measurements made on a ultrathin TiN film deposited by plasma-assisted atomic layer deposition by Langereis et al. in [33] are reported.
To predict the resistivity behaviour some model are available, in particular, both Chawla, Zhang, and Gall in [25] and Ingason et al. in [51], adopted, for reactive sputtering ultra-thin TiN films, the *Fuchs-Sondheimer* model:

$$\rho = \rho_0 \left[1 - \frac{3}{2\kappa}(1-p) \int_1^\infty \left(\frac{1}{t^3} - \frac{1}{t^5} \right) \frac{1 - e^{-\kappa t}}{1 - p e^{-\kappa t}} dt \right]^{-1} \tag{1.5}$$

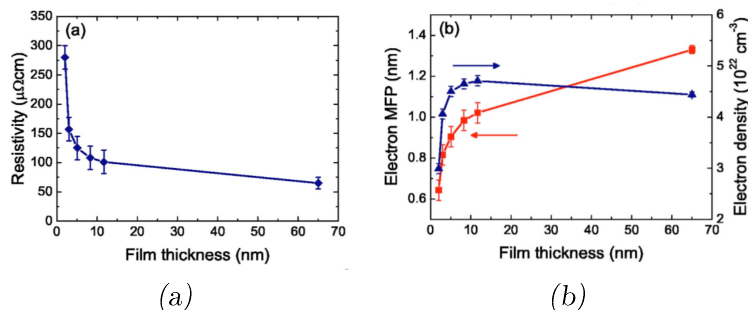

(a) (b)

Fig. 1.18: Resistivity (a) and electron free mean path (b) depending on the thickness of ultrathin TiN films deposited via PA-ALD. Taken from [33].

where t is the integration variable, ρ_0 is the bulk resistivity, $\kappa = d/\lambda$ the ratio between the characteristic length and the electron mean free path. p is a factor to take into consideration the nature of the scattering, it can take value from 1 to 0 where $p = 1$ means completely reflective scattering, while $p = 0$ completely diffusive. Both the groups, to carry out the calculations, considered $p = 0$. In figure 1.19, Chawla, Zhang, and Gall [25] compared the model with the experimental results from a reactive magnetron sputtering single crystal [001] TiN film deposited at 700°C and analysed at 77 K and 298 K. Assuming for the calculation $\lambda = 45$ nm and $\lambda = 217$ nm, reasonable values for a single crystal TiN at 298 K and 77 K, a perfect agreement between the model and the experimental results was found. Nevertheless, other authors [26, 33] reported that the model struggles approaching thickness of the order of 2 nm. This issue was explained assuming a widespread oxidation of the films, more likely composed by some form of TiO_xN_y rather than of TiN.

The modifications of the electronic characteristics and the presence of the substrate have a huge influence on the optical properties of the ultrathin films, even at thickness of some tens of nanometers [24].
Shah et al. in [26] investigated how the optical properties changed as a function of thickness of the sample in ultra-thin TiN films deposited by reactive magnetron sputtering on MgO substrate heated at 800°C. They observed that, as the thickness was decreased, both the real and imaginary part of the dielectric functions were red-shifted, due to the decrease of the carrier density (fig.1.20). The effect was particularly evident at ~ 2 nm thickness, probably due to the presence of a widespread oxide phase.
A more detailed study was carried out by [33] in Langereis et al., where the differences in the parameters of the Drude-Lorentz model (section A.2) in two TiN films deposited by PA-ALD and 12 nm and 65 nm thick were investi-

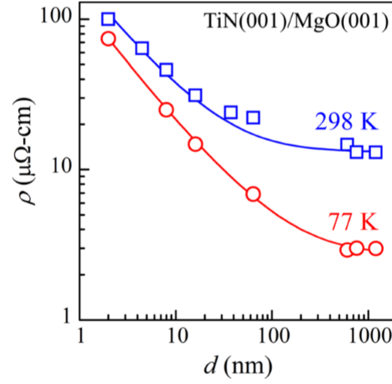

Fig. 1.19: Experimental values of resistivity (squares) as a function of the thickness of a single crystal TiN [001] film analysed at 298 K and 77 K compared to the Fuchs-Sondheimer model (solid lines). Taken from [25].

gated. The results are summarized in table 1.2. First of all, it can be noted a red-shift of ω_{pu} and ω_{02} as the thickness was decreased, that can be explained by the reduction of the electron density. At the same time, Γ_D increased, it is, indeed, proportional to the inverse of the mean free path, that decreased when the thickness was reduced. ω_{01} is associated to the interband transition along the [001] grain direction (section 1.3.1). Since the volume fraction of the grains with this orientation is higher at lower thickness (section 1.3.2), the higher values that ω_{01} and f_1 featured at 12 nm can be related to it.
In conclusion, it is clear that the decrease of the thickness down to few

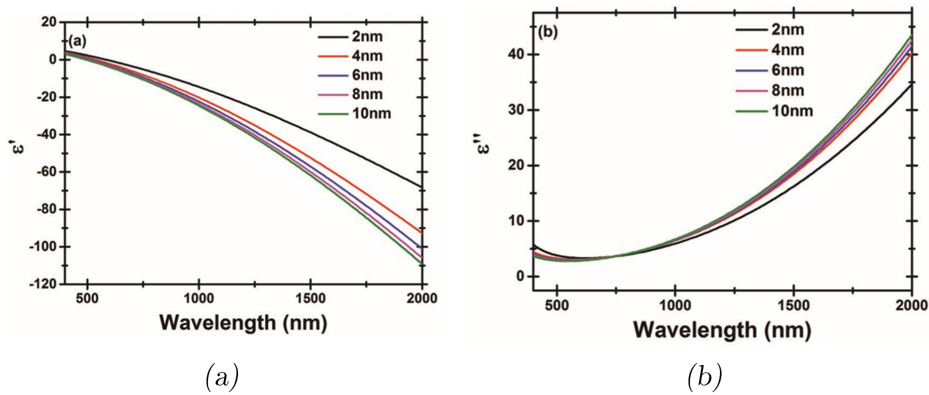

(a) (b)

Fig. 1.20: Real (a) and imaginary (b) part of the dielectric function of a TiN films obtained by magnetron sputtering depending on the thickness. Taken from [26].

Tab. 1.2: Dielectric function parameters of 12 nm and 65 nm thick *TiN* films deposited by PA-ALD. Taken from [33].

	12 nm	65 nm
Drude		
$\hbar\omega_{pu}$ (eV)	7.22 ± 0.05	7.29 ± 0.03
Γ_D (eV)	0.86 ± 0.05	0.61 ± 0.01
Lorentz		
f_1 (eV)	0.8 ± 0.2	0.2 ± 0.1
$\hbar\omega_{01}$ (eV)	3.8 ± 0.1	3.6 ± 0.1
γ_1 (eV)	01.6 ± 0.1	0.7 ± 0.1
f_2 (eV)	3.5 ± 0.3	5.8 ± 0.1
$\hbar\omega_{02}$ (eV)	5.6 ± 0.1	6.4 ± 0.1
γ_2 (eV)	2.3 ± 0.3	4.7 ± 0.2
ϵ_∞ (eV)	3.0 ± 0.1	1.5 ± 0.1

nanometers affects many properties of the films. In particular, when thicknesses of the order of the mean free path of the electrons are reached, the electronic characteristics of the samples are affected. This causes modifications in the optical response too, in addition to those from the crystallinity differences between thin and ultra-thin films (mainly in the crystalline orientation of the grains). All these possible variations are to be taken into account when it comes to the deposition of ultra-thin films. For this reason, in this thesis a preliminary study on the modifications of residual stress and electrical properties as a function of the thickness was carried out. The results are presented in section 4.1.1 and 4.2.1.

1.4 Previous results from the research group: a starting point

This thesis has to be seen in continuity with the work of Garattoni [1], that addressed the deposition of compact films of TiN with the long term aim of possible applications in the plasmonics field. This work was the first one of the research group where the PLD was applied to deposit TiN. The main goal was to find the optimum deposition conditions to obtain a homogeneous thin films of titanium nitride. For this scope many process parameter were varied, starting from the laser fluence and the background pressure and atmosphere. The fluences tested spanned from 11.5 to 1.7 J/cm^2, while the background pressure between vacuum ($\sim 5 \times 10^{-3}$ Pa) and ~ 10 Pa of N_2. The films were fabricated starting from a 99.9% pure TiN target and deposited on glass and silicon [100] substrates.
From the beginning, the EDXS and Raman analysis clearly highlighted that all the films were sub-stoichiometric and rich in oxygen. The situation was even worse in the films deposited with a high background pressure, where the resulting porous structure favoured an even widespread oxidation. To solve this problem the background gas was changed and a reducing atmosphere, composed by $N_2 - H_2$ ($95 - 5\%$), employed, but with poor results. In fact, the lowest oxygen content was still featured by the films deposited in vacuum conditions. Moreover, an additional issue occurred in the films deposited on the glass substrate, that showed evident signs of poor adhesion to the substrate. This issue was addressed using Ar ion bombardment as cleaning procedure to eliminate any possible contaminant or trace of moisture.
After these preliminary analysis the best deposition conditions were selected, namely in vacuum or with a background pressure of 1 Pa of $N_2 - H_2$, and with fluences between 1.7 and 3.1 J/cm^2. After the selection of the best conditions, the films were subjected to a thermal treatments at 550°C with the aim to improve the crystallinity and to investigate the response of samples to a thermal stimulus. The annealing treatments were performed both in vacuum and with an overpressure of the reducing atmosphere $N_2 - H_2$. Moreover, due to the high thermal coefficient mismatch between silicon and TiN, that caused the formation of holes in the film during the thermal treatments, the substrates were changed to thermally grown SiO_2 that, moreover, being an insulator, allowed to perform electrical measurements on the films.
The analysis conducted on the annealed films investigated the compositional, structural, electrical and optical properties of the samples, comparing the different effects of the thermal treatments atmosphere and deposition con-

ditions. X-ray Diffraction analysis showed that all the deposited samples featured [111] grain growth direction. This preferential direction of growth was expected, since the films deposited were at least 200 nm thick. The thermal treatments did not changed the preferential orientation, however, it seemed that they may have caused the recrystallization of a small amount of domains in different crystallographic directions ([001] and [110]), and improved the overall crystallinity of the samples and the dimension of the grains (from 4 to 9 nm). There were no visible differences between the samples annealed in vacuum and with the reducing atmosphere, but it seemed that lower fluence of deposition could have favoured a higher degree of crystallinity.
The differences in the annealing atmosphere were more evident in the Raman spectra. In fact, even if all the spectra of the annealed sample showed a blue-shift of the band at ~ 400 cm^{-1}, this shift was more evident in those treated in $N_2 - H_2$ atmosphere (fig.1.21). This blue-shift was attributed to an increase in the nitrogen concentration. Indeed, it was more consistent in the films that "saw" more nitrogen during their life, namely those deposited and annealed using the reducing atmosphere. In general, the annealing treatments caused some evidences of further oxidation and a better signal-to-noise ratio, that can be explained either with a more ordered structure or with a higher amount of material.
The effect of the thermal treatments on the electrical quantities could not be completely understood because it was not possible to measure the carrier density and mobility. Nevertheless, the results of the resistivity showed a slight increase in the values after the annealing that, however, where already

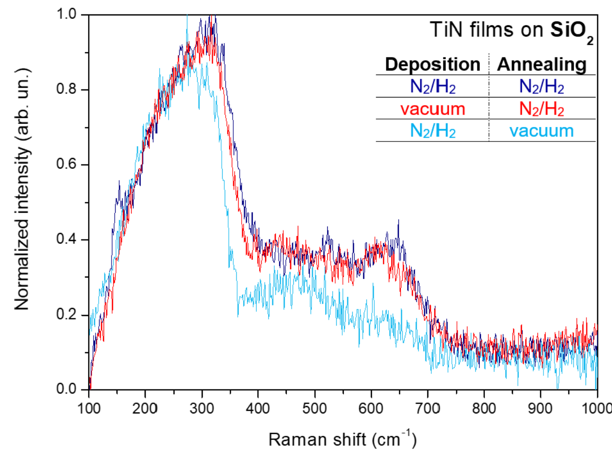

Fig. 1.21: Raman spectra of PLD-TiN depending on the annealing and deposition atmosphere. Taken from [1].

high with respect to the best numbers found in literature.
The optical analysis showed a red-shift in the reflectance minimum for the samples deposited with $N_2 - H_2$ with respect to those deposited in vacuum. A similar shift was experienced also by the films annealed with the reducing atmosphere, but in this case it came together with a lowering in the reflectance at the dip and in the near-infrared region of the reflectance curve. This phenomena were related to a lowering in the electronic density and oxidation issues, respectively. In general, it was noted that the annealing conditions had a greater influence on the films properties then the deposition ones (fig.1.21), but still lower than expected.

In conclusion, the open issue from the thesis of Garattoni, that will be addressed during this thesis work are:

- Poor nitrogen concentration and high oxygen content in the films, especially if deposited with a background atmosphere.
- Electrical measurements of the films, in particular those related to the electronic density and mobility.
- Improving the understanding of the oxidation and of the stoichiometry on the properties of the films, in particular the optical ones.
- Exploring different annealing temperature and conditions to improve the knowledge on the response of the films at a thermal stimulus.

All the samples deposited in my thesis work were fabricated using the best conditions highlighted by Garattoni. Thus, all the deposition were performed in vacuum, with fluneces that spanned from 1.7 to 3.1 J/cm^2 and on thermally grown SiO_2 substrates. Even the thermal treatments were performed in vacuum to avoid any possible source of oxygen, that, indeed, could be present in the injected gas as impurity.

1.5 Thesis objectives

The thesis of Garattoni [1] let open several issues, in particular related to the low stoichiometry of the films, the high oxygen content and the effectiveness of the thermal treatments. The long term aim remains the fabrication of thin films of TiN suitable for applications in the field of plasmonics, but the problems addressed in the previous works necessitate a different approach. Indeed, since the use of a background pressure of nitrogen or $N_2 - H_2$ in the chamber did not bring the desired results, different techniques must be investigated to face the low stoichiometry problem. The technique selected to deal with these issues is the Ion Beam Assisted Deposition (IBAD), already tested by the research group in the work of Mazza [69], but just at a very exploratory level. The results from this first attempt were encouraging though and, moreover, according to the literature (section 1.3.5), the use of ion assistance may result in several advantages, in particular, it may favour the reduction of the oxygen content in the films.
As far as the thermal treatments are concerned, due to the questioned effectiveness of those presented in the thesis of Garattoni [1], during my work higher temperatures were tested. Indeed, since the annealing treatments at 550°C resulted in just minor modifications, the most straightforward path to see if something would ever changed was to increase further the temperature.
To assess the effectiveness of the IBAD and of the annealing treatments, several analysis on the structure, the composition, the Raman spectra, the optical response and the electrical properties were conducted and consequentially compared.
Besides these two main objectives, other two preliminary studies were conducted. The first one tried to understand the extent of the residual stress in the films deposited with the assistance of the ions and without it. The scope of this study was to create the basis for further investigations with aim of reducing the internal stress in the samples and understand the growth mechanism of the early stages of the film deposition. The second minor study was a briefly research on how the thickness of the film affects the electrical quantities. They were a starting point to understand and explore whether it is possible or not to deposit ultra-thin films with room temperature PLD to take advantage of the possibility of the exploitation of quantum effects.
The experimental work can be divided into three different parts:

- Initially the focus was on the effects of the nitrogen ion bombardment on growing films, thus on the IBAD technique. Starting from the knowl-

edge of the PLD setup defined in the previous work of the group [1], the idea was to compare the results of three different fluences of deposition (from 1.7 to 3.1 J/cm^2). For each deposition fluence, the films were deposited in three different IBAD conditions. The first one, as reference, without any ion assistance; the second and the third with ion bombardment at 200 and 350 V acceleration voltages, respectively. These conditions were chosen to have a wide spectra of possibilities, but still comparable one another.

- The second step investigated the impact of the thermal treatments on the films. The basic idea was to increase the temperature and possibly modify the duration of the treatments with respect to the work of Garattoni [1]. The conditions chosen for the annealing were three. Each thermal treatment was composed by a ramping with a rate of 10°C/min followed by a dwell time. Two annealing were conducted with a dwell time of one hour at 700 and 865°C. While, the third one was shorter, it last only 15 minutes at 865°C, and the purpose was to observe the effects of a quicker treatment. All the deposited samples were tested in all the possible annealing conditions. The aim of the annealing treatments was to improve the electric, optical and structural characteristic of the films. In particular, the interest was in any possible healing mechanism of the lattice that may be activated at high temperature. Thus, the higher the temperature the more improvements should have been seen. However, if the temperature was too high, side effects may have appeared, as an extensive oxidation or phase changes.

- The last analysis made during this thesis work were carried out to explore the modifications in the residual stresses and in the electrical properties as a function of the thickness. The basic idea was to deposit two series of samples, one with ion assistance and one without it, each one composed by four couples of specimens with different thickness, from ~ 50 to ~ 350 nm. These samples were subsequentially analysed seeking for a trend in the internal stress and electrical properties values as a consequence of the different thickness.

All the samples were deposited via PLD starting from a 99.9% pure TiN target in vacuum. The experimetal setups needed for all the analysis mentioned before, and the PLD technique, are explained in the next chapter.

2. EXPERIMENTAL METHODS

2.1 Pulsed Laser Deposition (PLD)

Pulsed Laser Deposition (PLD) is a Physical Vapour Deposition (PVD) technique. Its basic concept consists in the production of a plasma plume from a solid target through irradiation with an intense laser pulse. Subsequentially, the recondensation on a substrate of the material from the plume guarantees the growth of the film. Almost any condensed matter material can be ablated by laser pulse and deposited, with a rate that can be finely tuned down to epitaxial growth regime [47]. Moreover, under optimal conditions, the PLD has the ability to transfer the exact stoichiometry of the target on the substrate (*congruent transfer of material*), allowing the deposition of complex stoichiometry films [70]. Furthermore, being the PLD an intrinsically out of equilibrium technique, it allows the fabrication of novel and metastable materials, impracticable under equilibrium conditions [47]. In vacuum, the range of the kinetic energy of the impinging species on the substrate is in the order of some tens of electronvolts, such range of energy favours the adatoms mobility, but avoids bulk displacements [47]. There are two main drawbacks in the use of this technique: the first one is the possible formation of solid particulate with dimensions ranging from 0.1 µm to 10 µm that may affect the homogeneity and the microstructure of the film. The second is a direct consequence of the shape of the plume that, being particularly peaked in the forward direction, reduces the area of thickness homogeneity to some centimeters square. This latest issue, in particular, reduces the scalability of the PLD and its feasibility as industrial technique and, indeed, the main applications of the PLD are in the research field.
In figure 2.1 the scheme of a PLD system is presented: the whole deposition process is carried out in a vacuum chamber that can be filled with inert or reactive gasses at specific pressures. In the same chamber, the target and the substrate are placed, one in front of the other, some centimetres apart. To homogenize the ablation and the deposition thickness, they move one respect to the other during the whole deposition. In the setup used during this the-

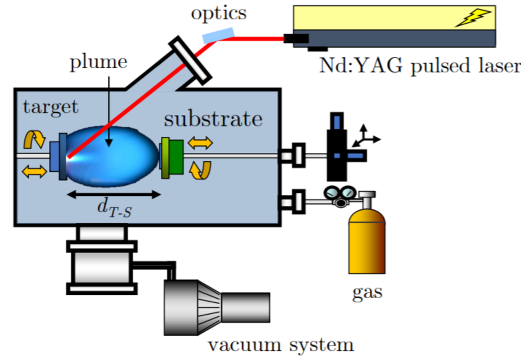

Fig. 2.1: General scheme of a PLD apparatus. Taken from [71].

sis work, the laser beam enters the chamber through a proper window and strikes the target with a 45° angle.
The presence of a reactive gas in the chamber modifies the deposited species, in this way from the same target several compounds can be deposited, e.g. oxides or nitrides. A second main effect of the presence of a background gas in the chamber, either reactive or not, is the changing in the dynamic of the plume formation and expansion that results in a modification of the deposition process. When the process is completed under vacuum the travel of the vaporized species from the target to the substrate can be considered collisionless. On the other hand, considering the presence of a gas in the chamber, the plume expansion can be schematized as a travelling shock wave front, identified as its further limit in the normal direction. The scattering between the vaporized species in the plume and the gas molecules slows down the wave front until it stops at the so called *stopping distance*. This dynamic, that results in a confinement in space of the plume, together with an additional cooling effect of the gas that may lead to oversaturation, favours the nucleation of clusters. Indeed, the aggregates that may originate during the plume expansion can be transferred in the gas phase where the velocity and the deposition energies are decreased. This situation favours the aggregation in clusters and lefts their structures and properties almost unchanged during the impact with the substrate.
To schematize the different dynamics of deposition, it is possible to introduce a new parameter, called *stopping distance*, defined as the time integrated length of the visible part of the ablation plume (l_p), i.e. the distance from the target reached by the shock front. If we compare this distance with the one between the target and the substrate (d_{TS}) we can define a new quantity:

$L = \dfrac{d_{TS}}{l_p}$. We can distinguish three cases (fig.2.2):

- *L<1 (substrate in plume)* the impinging species travel almost exclusively in the plume, the kinetic energy is thus high and the probability of cluster formation low. The film appearence is very compact and dense;
- *L∼1 (substrate at the plume edge)* with respect to the previous case the kinetic energy is expected to be reduced and the cluster number to increase;
- *L>1 (substrate out of plume)* the scattering with the gas molecules increases drastically due to the increased length of the path outside the plume and, thus, the kinetic energy is very low. The number of cluster in the film is very high and cluster-assembled nanostructured materials may form.

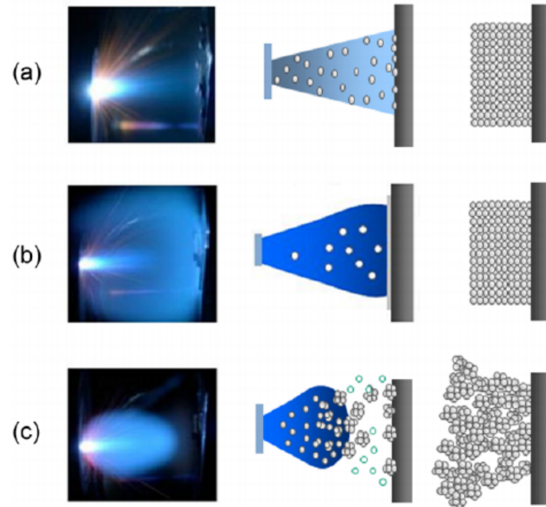

Fig. 2.2: PLD deposition of tungsten, it is well visible the plume in the three different configurations: (a) *substrate in plume*; (b) *substrate at the plume edge*; (c) *substrate out of plume* where the deposited film is porous. Taken from [72].

All the depositions in this thesis work were carried out under vacuum conditions (between 5×10^{-3} and 7×10^{-3} Pa) from a 99.9% pure TiN target, hence the dynamic of deposition corresponds to the first case. For this reason,

the expected structure of the films is compact for all the samples fabricated. In [1] it was pointed out that, when the deposition was completed with a nitrogen background pressure, the film was sub-stoichiometric and, without it, the situation was even worse. In this work, the problem of the stoichiometry was faced introducing the bombardment of the films with nitrogen ions during the deposition (for further details the reader is referred to section 1.4 and 1.5). This was made possible thanks to the implementation in the PLD setup of the Radio Frequency (RF) Ion Gun described in the next paragraph.

2.1.1 Radio Frequency (RF) Ion Gun

The RF Ion Gun is a source of ion beams designed to work in Ultra High Vacuum (UHV) or High Vacuum (HV) conditions when the PLD is operating. The Ion Gun used during this thesis work is the *RFMAX60* Ion Source (fig.2.3) from *Mantis Deposition Ltd*. The source of ions for the beam is a plasma generated directly in a ceramic discharge tube in the gun: RF power of 13.56 MHz is applied to a coil wrapped around the tube while the gas, of the same species of the ions wanted, is injected. The so obtained charged particles are then accelerated by two grids located at the end of the tube at which a potential different is applied. Since the plasma has intrinsic potential itself that depends on the gas flow and increases with the RF power, the lower limit to the energy of the ions can not be set freely. On the other hand, the upper limit is theoretically unbounded, however it is practically limited both by the sputtering phenomena that occur on the grids due to the impact with the accelerated ions, and by the instrumental limit of 1000 V. For nitrogen pumped with a flux of 15 *sccm*, that are the conditions used for all the samples, the upper limit is $\sim$ 360 V. The beam that emerges from the grids has a current that can range between 10 and 150 mA, divergence (with flat grids) of 7° and strikes the growing film with an angle of $\sim$ 45°. During this work the Ion Gun has been used primary to modify the chemical composition and the morphology of the films deposited, however, other effects are expected due to the bombardment with highly energetic particles, such as the modification of the residual stresses and the creation of defects and dislocations.

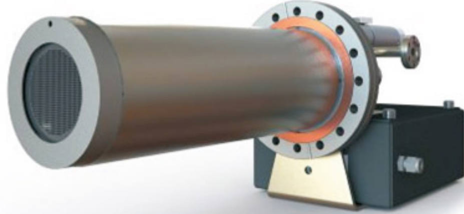

Fig. 2.3: RFMAX60 RF Ion Source.

2.2 Scanning Electron Microscopy (SEM)

Scanning Electron Microscopy (SEM) is a technique that utilizes electrons to acquire images, thus with better resolution (up to 1 nm) with respect to the optical microscope that works with photons. The imagine is obtained by bombarding the sample with an electron beam and causing the ejection of several particles, among them the secondary electrons that are subsequently collected by a dedicated detector. The number of electrons collected, thus the intensity of the secondary electrons, varies depending on the morphology and the composition of the area allowing the software to elaborate a detailed imagine in greyscale of the substrate. The general scheme of the SEM is presented in figure 2.4. The primary electron beam, generated through an electron gun, or Field Effect Gun (FEG), is highlighted in yellow. The sample beneath it can be moved thanks to a controller operated manually, in this way it is possible to scan the whole area of interest. The energies required to the primary electrons to allow the formation of a high resolution picture range between 1 and 30 keV. These energies are obtained by exploiting potential differences that accelerates the electrons. To collimate the the beam the electrons passes through a series of capacitors and deflectors prior the ingress in main chamber. The chamber, where are located also the samples to be analysed, is kept under vacuum conditions ($5 - 10$ mbar) to increase the free mean path of the electrons.
The SEM is, in general, a non-destructive tool to gain intuitive and fast information concerning external morphology, composition, crystalline structure and orientation of the specimen. Moreover, the interaction between the electrons of the gun and the samples originates many different effects besides

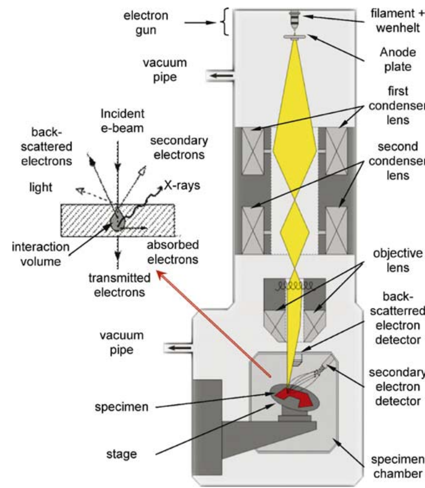

Fig. 2.4: Scheme of a Scanning Electron Microscopy (SEM). Taken from [73].

the ejection of secondary electrons, as the emission of x-rays. By collecting this radiation it is possible to interfere further characteristics of the sample, as its atomic composition. The technique that exploits this effect is the Energy Dispersive X-ray Spectroscopy (XRDS) and it is explained in the next section. Indeed, the SEM utilized, a Field Emission Zeiss SEM SUPRA 40 based on a GEMINI column, was equipped with an XRDS detector (by Oxford Instruments) that was extensively used during this thesis work.

2.2.1 Energy Dispersive X-ray Spectroscopy (EDXS)

The SEM used in this thesis work is equipped with a detector for the Energy Dispersive X-ray Spectroscopy (EDXS). The EDXS basic principle relies on the generation of x-rays as result of the collision between the electrons from the primary beam and the core electrons of the atoms in the sample: this interaction can result in the ejection of the core electrons and the subsequent formation of a hole that is rapidly occupied by a second electron, previously in a outer shell, with a related emission of energy. The energy of this transition is in the x-ray region of the spectrum and, since the energy of this electromagnetic wave is determined by the energetic levels of the atom, it is characteristic of the element. It is clear that, by using a collector able to distinguish the energy of the incoming x-rays, it is possible to understand which

are the elements contained in the sample. Moreover, considering the intensity, it is even possible to have quantitative information about the species present. Thus, it is possible to understand the composition of the sample with an accuracy of some percent. However, it has to be said, that this technique loses accuracy as the atomic number of the element decreases, so, in this thesis work, since we are dealing with some light elements, such as nitrogen and oxygen, the values obtained using the EDXS are to be taken as an indication of a trend more than a precise indication of the composition of the samples. Moreover, the situation is worsened by the fact that the corresponding x-ray energies of titanium, nitrogen and oxygen are all within 0.13 keV.

2.3 Raman Spectroscopy

Raman spectroscopy is a non-destructive and contactless technique that exploits the inelastic scattering between light and lattice or molecular vibrations. It can be used to interfere many properties of the material through the determination of the vibrational modes of the samples, in particular: the chemical composition, the crystallinity, any polymorphisms and interaction with molecules. When a monochromatic light (e.g. a laser beam), strikes the sample, the system is excited to a higher vibrational level, which can be either real or virtual. The excess of energy is soon released by emission of a photon causing the de-excitation of the system. The exchange energy is given by the difference in energy of the two vibrational levels. In the case of a crystal this energy is defined by a phonon, the quantum of a normal vibrational mode, whose energy is given by $\hbar\omega_{ph}$.
The working principle of this technique relies on the fact that the de-excitation can follow three different paths (fig.2.5):

1. *Rayleigh scattering*: the system comes back to the previous vibrational level, this means that there is not any net exchange of energy and the scattering is considered elastic. This path is by far the most probable and it is the origin of the gigantic peak in intensity in figure 2.5 at ν_0: the intensity of the peak is, indeed, five to six orders of magnitude greater than the inelastic scattering

2. *Stokes scattering*: the final vibrational level of the system is higher in energy than the initial one: the emitted photon has, thus, lower energy with respect to the incident. The energetic difference is the same present between the initial and the final level of the system

3. *Anti-Stokes scattering*: in this case the initial level is an excited vibrational level of the system, higher in energy than the final one. Thus, the resulting photon is more energetic than the incident one. When these two levels correspond to the final and initial one of the *Stokes scattering* case, the exchanged energy is the same, but with the opposite sign. The anti-Raman scattering is the less probable path, thus the less intense transition, because it requires the system to be excited prior the transition and, at room temperature, this is an unlikely situation since the phonons follow the *Bose-Einstein* statistic.

To be effectively observed by the Raman spectroscopy, a normal vibrational mode of the molecule or of the lattice must satisfy two requisites: the polarizability of the system must change during the interaction and the wave

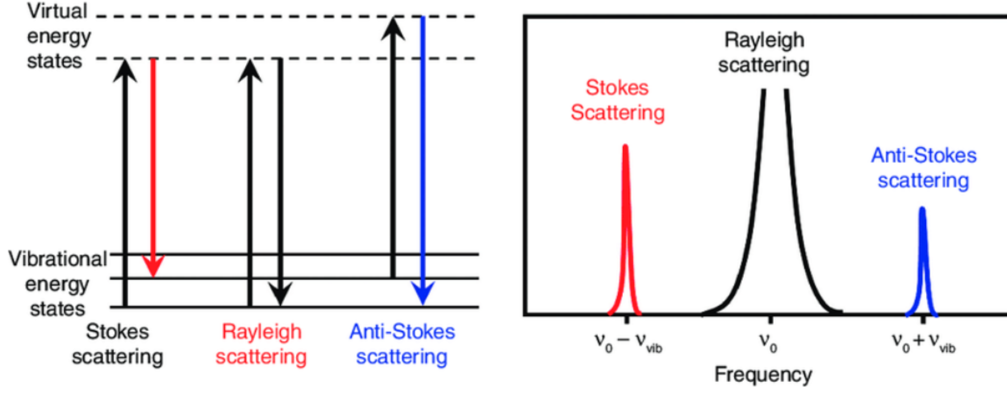

Fig. 2.5: In the left figure, scheme of the three different de-excitation mechanism during Raman spectroscopy. In the right figure, intensity peaks from the three different de-excitation paths. To be noted the difference in height between them, with the Rayleigh one extremely bigger then the other two and the anti-Stokes peak smaller then the Stokes peak. Taken from [74].

vector ($\mathbf{q}$) must be ~ 0. This selection rule originates from the requirement of the following momentum conservation

$$\boldsymbol{k_L} = \boldsymbol{k_{ph}} + \boldsymbol{q} \tag{2.1}$$

where $\boldsymbol{k_L}$ and $\boldsymbol{k_{ph}}$ are respectively the wave vector of the incident and scattered photon. Being $\omega_L \approx \omega_{ph}$, $\|\boldsymbol{k_L}\|$ and $\|\boldsymbol{k_{ph}}\|$ are almost identical. This implies that $\boldsymbol{q}$ is required to be approximately zero, condition satisfied only for optical phonons at the centre of the Brillouin zone. However, this selection rule does not hold when it comes to consider not perfectly periodic lattices. Indeed, if we apply the uncertainty principle

$$\Delta x \Delta p \geq \frac{\hbar}{2} \tag{2.2}$$

as soon as the distance over which the system is periodic (Δx) is reduced, the knowledge of the momentum value decreases and the selection rule relaxes. For this reason, while the Raman spectra for perfect crystal or single molecules presents well defined peaks, as soon as the periodicity is reduced, the peaks become wider bands. This effect is particularly evident in amorphous material. In fact, in this case $\Delta x \to 0$ and almost all the normal

modes are visible by Raman spectroscopy. Moreover, it may happen that the Raman spectrum is visible due to the presence of defects in the lattice, e.g. vacancies. Since the defects are intrinsically non-periodic, the Raman spectra observed is composed by bands, as for an amorphous material. This particular phenomenon, at the base of the Raman spectrum of TiN, is explained further in the next paragraph.

The Raman spectra acquired during this thesis work made use of a Renishaw InVia micro Raman spectrometer and, as excitation source, a green Laser ($\lambda = 514$ nm), with a power of 0.93 mW. The measurements required ten accumulation, each one with a scanning duration of 10 s.

2.3.1 Raman Spectroscopy of TiN

The crystalline structure of the TiN, since is perfectly symmetric, does not satisfy the requirements concerning the polarizability, so it should not feature a Raman spectra. However, as explained by Chowdhury et al. in [37] in the TiN lattice are intrinsically present some vacancies of nitrogen and titanium that break the perfect symmetry allowing the TiN to be Raman active. Due to the fact that the vacancies are intrinsically local defects, without spacial periodicity, the requirements on the conservation of the momentum is greatly relaxed and the Raman spectra that are observed are composed by wide bands and not by well separated peaks. The widening of the the bands is further enlarged by the small dimension of the grains ($\sim$ 10 nm), that increases the reduction of the periodicity.
In figure 2.6, it is presented the Raman spectra of a stoichiometric sample 2 µm thick obtained by Pulsed Laser-Scattered Ballistic Deposition (PL-SBD) using a KrF excimer laser at 280 nm in $N_2 - H_2$ $(95 - 5\%)$ atmosphere from [75]. There are basically two different bands that can be distinguished: the first one, around 200 and 300 cm^{-1} is related to the acoustic modes of the Ti^{4+} ions due to the presence of nitrogen vacancies; the second one, the band between $500 - 600$ cm^{-1}, is referred to the optical modes related to the vibration of the N^{3-} ions caused by titanium vacancies. More in details, the band below 400 cm^{-1} is separated in two peaks, the first at $200 - 215$ cm^{-1} is referred to the longitudinal acoustic mode, while, the second, at $300 - 330$ cm^{-1}, to the transverse acoustic one. At $440 - 450$ cm^{-1}, it can be observed a very small peak related to second order transverse acoustic modes and, higher in energy (not visible in fig.2.6) it would be possible to find peaks

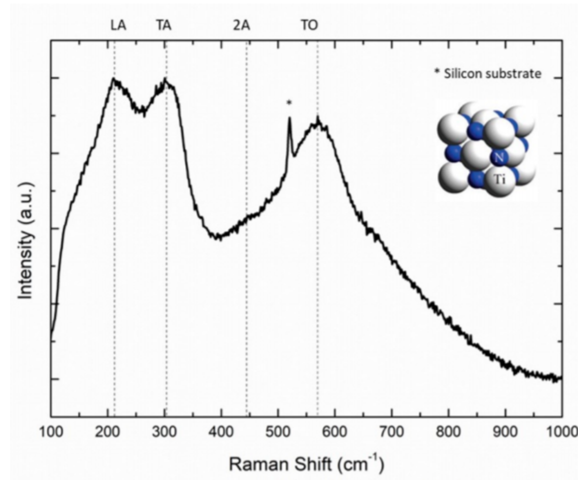

Fig. 2.6: Raman spectra of a *TiN* film obtained via Pulsed Laser-Scattered Ballistic Deposition. Taken from [75].

originating from two-phonon scattering (TA+LO) at $820 - 825$ cm^{-1}. Even higher, at ~ 1100 cm^{-1}, there would be other peaks from second order optical modes. For further details the reader is referred to the previous thesis of the research group [1, 69].

2.4 Electrical and Hall measurements

The electrical characterization of the films has been carried out using the Van der Pauw setup. This apparatus is a practical and fast measurement method that utilizes four gold probes to assess the resistivity (ρ), the carrier density (n) and mobility (μ) on films with simple geometry, without the necessity to have a knowledge of the dimensions of the specimen. Indeed, compared to different setups, this method effectively solves the issues that arise when the resistivity has to be measured on samples that host a non one-dimensional current flow. The scheme is rather simple and there are just a few requirements:

1. the samples to be measured must be geometrically simple (common geometries are: squares, circles and Greek cross) and simply connected;

2. the four probes must act as ohmic contacts and be placed on the edges of the sample;

3. the probes should be as close as possible to the concept of point contact. Indeed, as it will be explained later, the ratio between the area of contact and the dimension of the samples is strongly related to the accuracy of the measurement.

Resistivity measurements

To perform the measurements of the resistivity, the probes are placed on the film as to create a square (fig.2.7). The basic idea is to assess the voltage difference experienced between two contacts, while a current flow is imposed between the other two. The measurement is carried out twice, the second time reversing the current, in this way it is possible to remove any thermo-electric voltages. Once the data are collected, using the following equation it is possible to evaluate the resistance referred to the first configuration represented in figure 2.7, denoted as $R_{21,34}$:

$$R_{21,34} = \frac{V_{34}(I_{21}^{+}) - V_{34}(I_{21}^{-})}{I_{21}^{+} - I_{21}^{-}} \tag{2.3}$$

Solving the same equation for the second set of contacts in figure 2.7, it is possible to evaluate $R_{32,41}$ and then, with the following equation, the sheet resistance ρ^{A}_{sheet}:

$$\rho^{A}_{sheet} = \frac{\pi f}{ln(2)} \frac{(R_{21,34} + R_{32,41})}{2} \tag{2.4}$$

where f is a factor function of $R_{21,34}$ and $R_{32,41}$.
Finally, repeating all the steps using the two other combination of contacts to find ρ^{B}_{sheet}, it is possible to evaluate the total sheet resistance (ρ_{sheet}) as:

$$\rho_{sheet} = \frac{\rho^{A}_{sheet} + \rho^{B}_{sheet}}{2} \tag{2.5}$$

Once the sheet resistance has been calculated, if the thickness (d) of the film is known, the resistivity is easily assessed multiplying the two quantities:

$$\rho = \rho_{sheet} d. \tag{2.6}$$

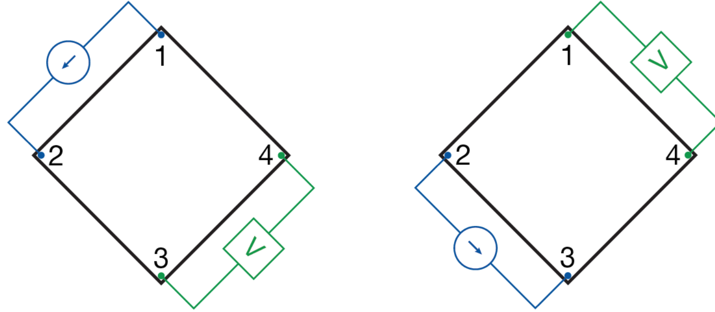

Fig. 2.7: Connection scheme for a resistivity measurements on a 2D sample with van der Pauw method. Taken from [76].

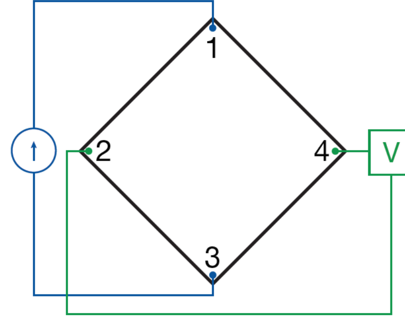

Fig. 2.8: Connection scheme for Hall effect measurements on a 2D sample with van der Pauw method. Taken from [76].

Hall effect measurements

The setup for the Hall measurements is very similar to the one for the resistivity, but this time the current and the voltage measurements are carried out along the diagonal of the film, as shown in fig.2.8, while the sample is immersed in a magnetic field, to exploit the Hall effect. For each measurement, the the data are collected in the two possible configurations (Configuration A: voltage measured between point 2 and 4, configuration B: between 1 and 3) and for each configuration with the current flowing in both the two possible directions, as for the resistivity. The measurements are taken three times. Firstly without any magnetic field, as reference, then, both with the positive (V^{B+}) and negative magnetic field applied (V^{B-}), to avoid any possible misalignment voltages. Finally, once all the data are collected, the Hall voltage (V_{Hall}) is calculated using the following equations:

$$V_{AHall} = \frac{V^{B+}_{13,42} - V^{B-}_{13,42}}{2} \tag{2.7}$$

$$V_{BHall} = \frac{V^{B+}_{24,31} - V^{B-}_{24,31}}{2} \tag{2.8}$$

$$V_{Hall} = \frac{V_{AHall} + V_{BHall}}{2} \tag{2.9}$$

Once the Hall voltage, together with the value of the magnetic field (B), the film thickness (d) and the current (I), is known, it can be used to determine

both the carrier density and mobility using the following equations:

$$n = \frac{IB}{qdV_{Hall}} \tag{2.10}$$

(2.11)

$$\mu = \frac{dV_{Hall}}{IB\rho} \tag{2.12}$$

To asses the reliability of the measurements of the mobility and the carrier density, it is possible to define a parameter, called Figure of Merit (FoM), calculated as follows:

$$FoM = \frac{zero_check}{V_h} \tag{2.13}$$

where V_h is the sum of V_{AHall} and V_{BHall} and $zero_check$ the average of the potential measured in all the possible probes configurations without any magnetic field. In theory, $zero_check$ should be zero or, at least, much smaller than V_h. Thus, to be reliable, the measurements must feature a very low Figure of Merit. In this thesis work, the threshold value of the FoM, to decide whether to discard or not the measurement, was set to ± 1.
The most important parameter that affects the accuracy of the measurements is the ratio between the contact lateral size δ and the sample size a. Considering both of them squared, if the probes are placed in the corners, the error can be limited to 10% if δ/a is less than 0.1. To reduce further the maximum error, the contacts can be located at the midpoint of the sample sides, or the geometry changed. Indeed, in general, a Greek cross geometry assures better accuracy of the measurements [76].

The instrument setup used during this thesis was composed by a Keithley 2400 SourceMeter, as current source, and a Keysight 34972A LXI connected to a PC, for the data acquisition, while the different contact configurations were selected by a custom manual switch. The obtained data were analysed by a $MatLab$ code written for the purpose.

2.5 Optical reflectance measurements

The measurement of the optical reflectance were carried out at the Centre for Nanoscience and Technology (CNST) of the Italian Institute of Technology (IIT) in Milan using a LAMBDA 1050 UV/Vis/NIR spectrophotometer. This instrument is based on the *Ulbricht's integrating sphere* (fig.2.9) that, as the name implies, consists in a sphere with two openings, one in front of the other. The sample, with the film inward, is placed on one opening, while, through the second one, a light beam is projected on it. The light reflected back or diffused is trapped in the sphere and eventually collected by the detector that evaluates the intensity. This procedure is carried out scanning over a wide wavelengths range to obtain a dependence between the reflectance and the incoming light energy. The same operation is done with the bare substrate to have a reference. Indeed, a portion of the detected radiation could be light reflected by the substrate, affecting the measurements. To avoid this possibility, the software compares the results obtained with the bare substrate and with the samples, allowing to determine with more accuracy the reflectance of the film.
The measurement of the reflectance of a sample can give several information, in particular about the position of the plasma frequency and the lattice quality of the film. During this thesis work the reflectance has been used extensively and, for this reason, in the next paragraph, the key features of the reflectance of TiN will be presented.

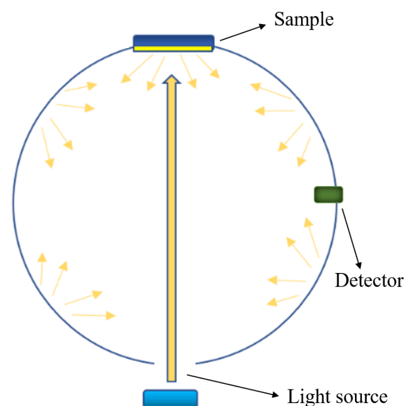

Fig. 2.9: General scheme of a Ulbricht's integrating sphere setup.

2.5.1 Reflectance behaviour of TiN

It may be useful to make a brief overview on the reflectivity of a metallic material, as TiN, to better understand the results of the optical measurements. A further discussion about some quantities here introduced (e.g. the refractive index) and plasmonics in general will be presented in section A.1 and A.2.
When the reflectivity from a normally incident beam is considered, the governing equation is:

$$R = \frac{(n-1)^2 + \kappa}{(n+1)^2 + \kappa}. \tag{2.14}$$

that depends on the imaginary (κ) and real (n) components of the refractive index ($\tilde{n}$).

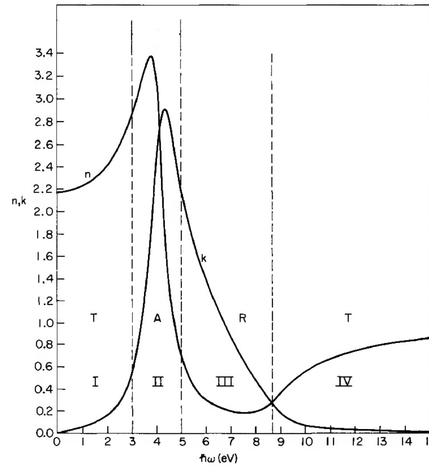

Fig. 2.10: Real n (broken line) and imaginary κ (solid line) components of the refractive index $\tilde{n}$. The spectra considered can be divided into four different regions where the material is in turn mostly absorbing (A), transmitting (T) and reflecting (R). ω_p corresponds to the frequency at which $n = \kappa$ (~ 8.7 eV).Taken from [77].

In figure 2.10 is presented the overall behaviour of a metallic solid depending on the value of the components of the refractive index. As it can be seen, the graph can be divided into four different parts, where different responses prevail. The region of our interest is close to the plasma frequency (ω_p), that corresponds to the point of transition between region III and IV, where $n = \kappa$. At the interface between these two regions the optical behaviour of the

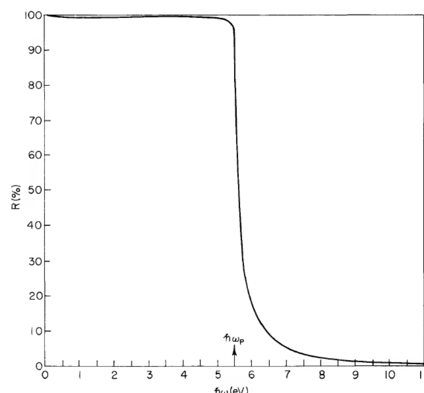

Fig. 2.11: Theoretical reflectance edge of a hypothetical Drude metal. Taken from [77].

material changes abruptly from complete reflectance to total transmittance (fig.2.11). This phenomenon causes an exponential drop in the reflectance curve that starts exactly at the plasma frequency and that goes under the name of reflectance edge. This happens, according to the Drude model, because the free electrons in the material are not able to absorb energy higher than $\hbar\omega_p$. Thus, an electromagnetic waves with higher frequency can get through the material freely. However, in reality the reflectance edge does not have such abrupt decay: it starts with a more gentile slope and the plasma frequency is placed somewhere in the middle of the edge, as it can be seen in figure 2.12 where an experimental curve of a reactive sputtering TiN film is shown. Actually, since we are dealing with real systems, we should use the screened plasma frequency ($\omega_{ps} = (4\pi ne^2/\epsilon_\infty m_e)^{1/2}$), that takes into account the dielectric behaviour of the material, namely the interband transitions, and corresponds to the frequency at which $\epsilon_1 = 0$. The frequency at which the curve reaches its minimum value corresponds to the frequency at which the refractive index equals the one of air (or the medium in which the material is immersed) [78], that goes under the name of ω_{min} and it is slightly blue-shifted with respect to ω_{ps}, approximately at 400 nm for TiN [10]. This frequency can be calculated starting from ω_{ps} using this equation [78]:

$$\omega_{min} = \sqrt{\frac{4\pi ne^2}{(\epsilon_\infty - \epsilon_{air})m_e}} \tag{2.15}$$

Thus, it is clear that any modification in ω_{ps} changes the position of the reflectance edge and of the minimum. In particular, since the plasma frequency depends on the square root of the concentration of electrons (n), a

higher electronic concentration means a blue-shift in the minimum (and in the reflectance edge) and vice-versa when the concentration decreases. The two main causes of the reduction of the electronic density are an increase of the content of nitrogen and the oxidation of the film [10], but it could be related to lattice defects or traps too.

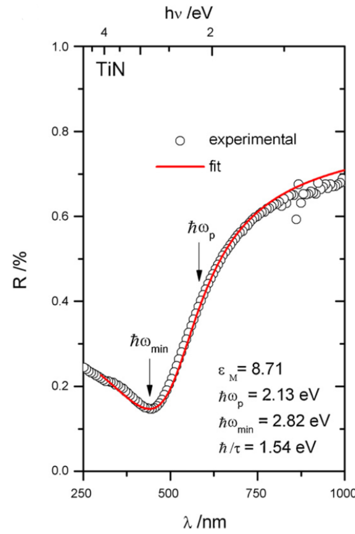

Fig. 2.12: Reflectance curve of TiN is the plasmonic edge region. It can be seen that the experimental data (circles) fit well the theoretical plot obtained with the Drude-Lorentz model (red line) that takes into account the dielectric losses. Taken from [79].

The steepness of the edge, thus the slope of the curve, depends on the quality and the composition of the film, more in general on the relaxation time of the Drude model (τ), the shorter is τ, the less steep the edge. For example, in [79] it is shown that, in a TiN film obtained by reactive sputtering, the slope decreases as the oxygen concentration augments. The same effect is obtained in [80] inserting carbon or modifying the stoichiometry: the curve is less steep both for sub-stoichiometric and over-stoichiometric films. In [81] the reduction in the steepness is caused due to the lowering in the substrate temperature during the deposition that translates in a more defective film. There are other features of the curve that can be related to the quality of the films too, for example the reflectance value in the long wavelength limit. In theory it should be 100% and it decreases as the quality is lowered [81]. However, the reflectance values can be influenced also by the electronic density: if all the other characteristics are identical, the higher is the concentration of electrons, the more light can be effectively reflected and the higher the

reflectance value will be [82]. Even the reflectance value of the reflectance dip is influenced by these factors, but also the interband transitions play a major role [10], increasing its reflectance, thus it is very difficult to understand which effect is the most important in each situation. In general, it can be said, that a deviation from the ideal behaviour of the curve it is easily associated to a lower quality of the films, but the exact origin of the modification is very difficult to identify due to the high number of possibilities.
As can be seen in figure 2.11, at energies higher (thus at shorter wavelength) than the reflectance edge the reflectivity should be zero. However, this holds only in theory, indeed, as soon as the interband transitions are activated, the reflectance increases, as it is well visible in figure 2.12 at $\lambda < \lambda_{min}$. In the case of TiN, these transitions are excited roughly for $\lambda < 500$ nm and are between $N - p$ and $Ti - d$ bands [4] (section 1.3.1).

It is evident that from the reflectance measurements many information about the film can be obtained, at least from a qualitative point of view. Indeed, the characteristics of the material influences many aspects of the reflectance curve. However, as far as the plasmonics is concerned, from these measurements, it is only possible to obtain an indication of the range of frequencies in which the screened plasma frequency is located: to obtain more precise values for plasma frequency we need more sophisticated tools, such as ellipsometry.

2.6 Thermal treatments

The heater used during this thesis work for thermal treatments is a custom made setup presented in figure 2.13. It consists in a vacuum chamber containing the sample holder that can be filled with gas at the occurrence. The vacuum is achieved through a turbo pump connected in series with a rotary pump and can reach values down to $\sim 4.5 \cdot 10^{-5}$ Pa. A heater controller (Tectra HC3500 Heater Controller), connected to the PC, manages the heating of the sample holder through electrical resistance. The temperature is measured both with a thermocouple and a pyrometer.
During this thesis work the heater was used to perform vacuum annealing at different temperatures and dwell times. The ramping rate, the speed at which the annealing temperature is reached, was set to 10 °C/min for all the thermal treatments performed.

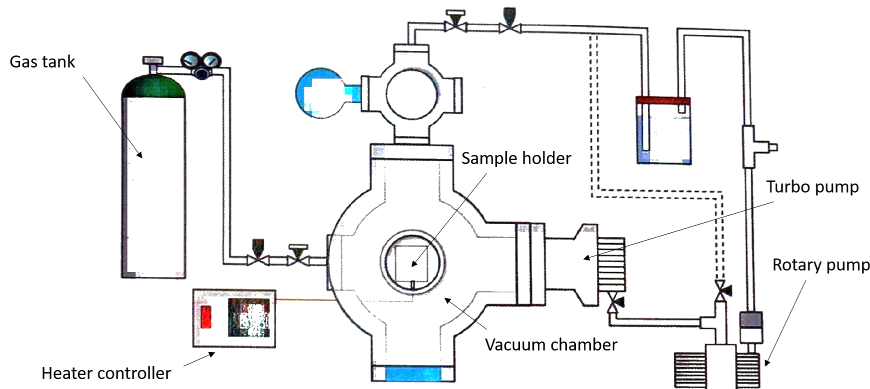

Fig. 2.13: Scheme of the heater setup.

2.7 Residual stresses measurements setup

To investigate the residual stresses present in the deposited films a custom setup (fig.2.14) that relies on the Stoney equation (eq.2.16) was used. The basic idea is to measure the the radius of curvature of the substrate (s) before and after the deposition. Indeed, assuming perfect adhesion between the two layers, the stress accumulated by the film (f) will be compensated by the one in the substrate modifying the curvature radius, to maintain the overall equilibrium of the system. The difference between the two curvature radii, under the rather strong assumption of homogeneous stress distribution in the two layers, will be a direct indication of the stress in the film σ_f. This stress can be evaluated through the Stoney equation, an extremely powerful method that does not require any knowledge of the elastic properties of the film, here presented:

$$\sigma_f = \frac{E_s}{1-\nu_s}\frac{t_f}{t_s^2}\frac{1}{6}\left(\frac{1}{R} - \frac{1}{R_0}\right) \tag{2.16}$$

Where R is the curvature radius of the substrate after the deposition and R_0 prior the deposition, E_s and ν_s are respectively the Young modulus and the Poisson ratio of the substrate, and t the thickness. This equation holds when the film can be considered much less thick than the substrate, as in the case of this work where the silicon substrate are 300 µm thick and the film hundreds of nanometers. It is extremely powerful since it does not require to know the elastic properties of the film.
The procedure to evaluate th residual stress with the experimental setup (fig.2.14) requires two measurements: the first one on the substrate to calculate R_0, the second on the film to assess R. As it will be soon clear, both the substrate and the film must be reflective. To proceed, the specimen is placed on the sample holder and, through an optical path, four laser beams, arranged as a rhombus, are projected on it. The reflected beams are collected by a CMOS sensor and converted into frames of a video. Subsequentially, a program analyses the frames to obtain the reciprocal distances between the laser spots and, then, calculate the curvature radius. The two calculated radii are inserted in a *MatLab* code together with the elastic properties of the substrate and the thickness of the two layers. With all these information, the program is able to calculate the residual stress in the film thanks to the Stoney equation.

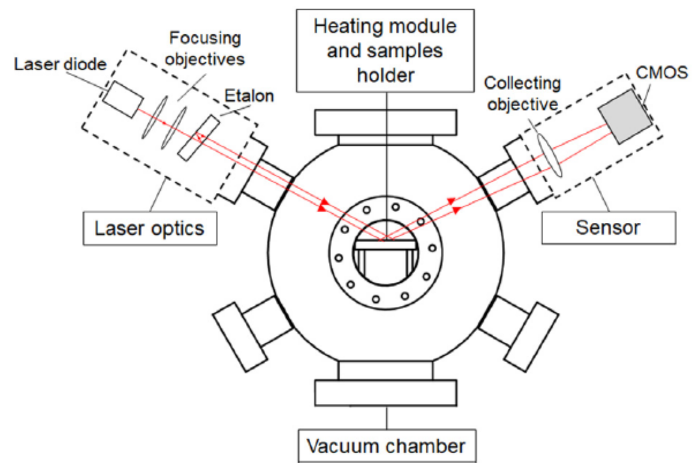

Fig. 2.14: Scheme of the experimental setup to measure the residual stress. Taken from [83].

3. TITANIUM NITRIDE THIN FILMS DEPOSITED VIA ION ASSISTED PLD

In this chapter the results of the analysis conducted on the samples will be presented. The first part of experimental results will deal mainly with the effect of the Ion Beam Assisted deposition at different ion energies and fluences, the analysis of the morphology and the structure of the samples, the electrical properties, the Raman spectra and the composition of the specimens. Then, the effect the thermal treatment will be considered, too. The annealing purpose was to increase the grain dimension and to activate healing processes of the lattice to favour the electron mobility of the samples. The analysis will be carried out by comparison between the results prior (as-deposited) and after the thermal treatments to highlight any possible improvements in the quantities of interest. A better comparison, especially for what concern the crystallinity and the grains dimension of the samples, would be possible thanks to X-Ray Diffraction (XRD) measurements. However, they were not available at the time this thesis work was done. Thus, the analysis of these properties will be carried out only by hypothesis and inferences through data from different measurements.

3.1 As-deposited samples analysis

The samples in this thesis work have been fabricated by Pulsed Laser Deposition (section 2.1) under vacuum conditions ($\sim 6 \times 10^{-3}$ Pa), starting from a 99.9% pure target of TiN. The fluence conditions were selected among the best found in the previous thesis of the group [1, 69], and the chosen ones are 1.7, 1.9 and 3.1 J/cm^2. The main differences expected in the films deposited at different fluences are in the structure. Indeed, higher fluence means more energetic impinging species that, in principles, is translated in higher surface mobility. This should result in a more compact columnar structure. The Ion Beam Assisted Depositions were carried out using a RF Ion gun (section 2.1.1). The energy of the impinging ions was limited by the instrument itself and varied from 200 to 350 V. The nitrogen flux entering the RF Ion

Tab. 3.1: Deposited samples and fabrication conditions.

Name	Fluence (J/cm^2)	Lenses distance (mm)	Thickness (nm)	IBAD voltage (V)
TiN_1.7	1.7	40	485	No-IBAD
TiN_1.7_200	1.7	40	459	200
TiN_1.7_350	1.7	40	375	350
TiN_1.9	1.9	55	495	No-IBAD
TiN_1.9_200	1.9	55	512	200
TiN_1.9_350	1.9	55	470	350
TiN_3.1	3.1	55	452	No-IBAD
TiN_3.1_200	3.1	55	412	200
TiN_3.1_350	3.1	55	420	350

Gun was set at 15 *sccm* for all the depositions. All the samples (prior to the thermal treatment) and the conditions at which they were fabricated are summarized in table 3.1. Before the IBAD depositions, a calibration without assisting ions was made to evaluate the deposition rate of the three fluences. The resulting values were 8 nm/min, 10 nm/min and 17 nm/min respectively. Knowing the rate of deposition, the thickness of all the films was set to 500 nm. However, the actual thicknesses measured with the SEM resulted, in general, lower (tab.3.1). In particular, the height of the film was more reduced when the bombardment with ions was active. The cause of this effect is not clear, it could be an effect of material removal, maybe through a sputtering effect of the deposit, an effect of deflection and scattering of the impinging species, or an effect of compaction of the deposit under the action of the ions. It is difficult to give a definitive answer to the question with the available information, besides the thickness of the films does not seem to follow a well defined trend with the energy of the ions.
Cross-section SEM imagines were taken for all the samples using the apparatus described in section 2.2. The obtained pictures of some of the samples are presented in figures 3.1 and 3.2. These films are here reported as example to compare the two opposite deposition conditions: no-IBAD and ion assistance at 350 V, as the samples deposited at 200 V show intermediate features. The characteristics of the films are very similar for all the deposition conditions, with a compact and rather irregular columnar structure of the grains. The regularity and the continuity of the columns seems to be better in the films deposited at 3.1 J/cm^2, probably for the presence of more energetic species that should have higher surface mobility. The effect of the ion bombardment on the structure seems completely absent in the samples

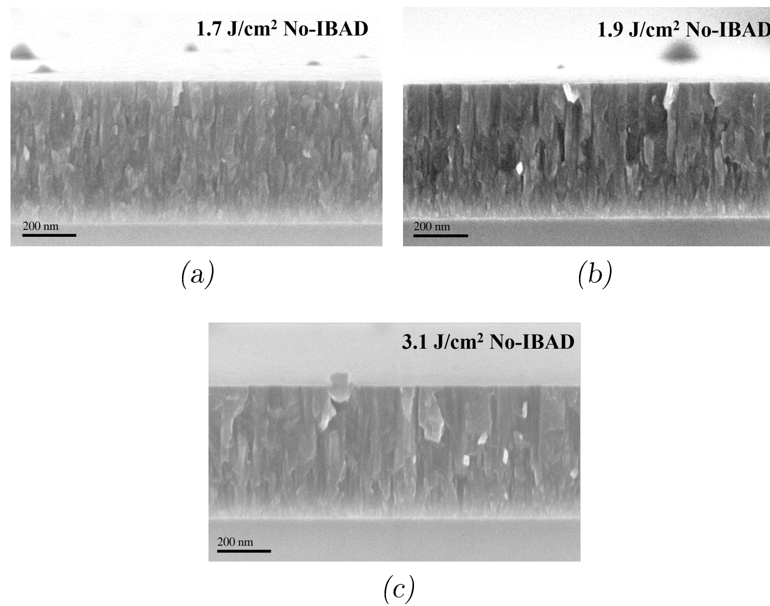

(a) (b) (c)

Fig. 3.1: SEM imagines of the cross-section of the samples deposited without ion assistance at 1.7 (*a*), 1.9 (*b*) and 3.1 J/cm^2 (*c*).

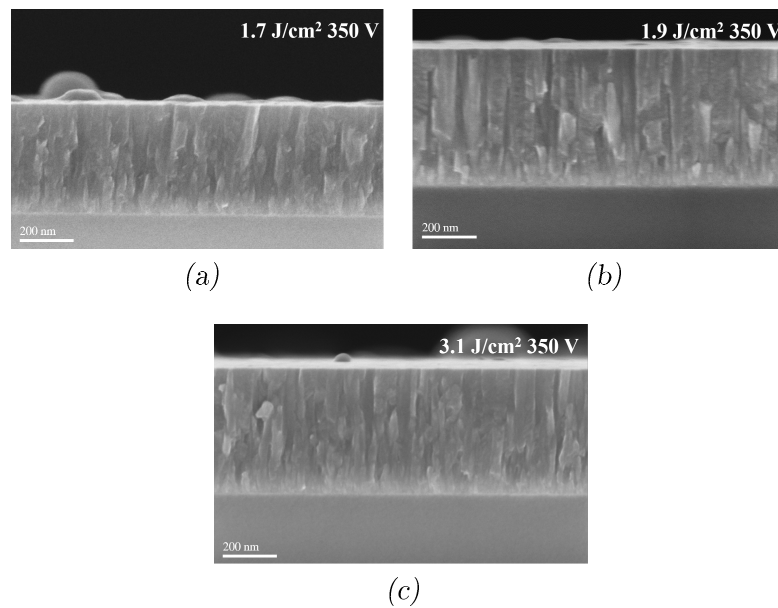

(a) (b) (c)

Fig. 3.2: SEM imagines of the cross-section of the samples deposited with ion acceleration voltage of 350 V at 1.7 (*a*), 1.9 (*b*) and 3.1 J/cm^2 (*c*).

deposited with this fluence. On the other hand, the films deposited at 1.7 and 1.9 J/cm^2 appear to be slightly affected by the impinging ions. It can be observed that the columns of the samples deposited at 350 V resemble those of the films deposited at the highest fluence, with the borders rather more smooth. Thus, from this preliminary and qualitative observations, it seems that the assisting ions may have an effect similar to the increase of the fluence, probably caused by an enhancement of the mobility of the deposited species. However, it should be considered that such small differences may be determined just by the quality of the cut made in the film to analyse the cross-section.

3.1.1 EDXS measurements

The EDXS measurements (section 2.2.1) allow to get information about the atomic composition of the samples. However, due to small atomic number of nitrogen and oxygen and the vicinity in energy of the x-rays related to these two elements and titanium (all of them are within 0.13 keV), the values obtained through EDXS analysis are not enough reliable to make precise comparisons, for the purpose more accurate techniques, e.g. X-ray Photoelectron Spectroscopy (XPS), are needed. Nevertheless, it is possible to define a trend in the concentration of the atomic species as the IBAD voltage or the fluence are modified. The concentration of nitrogen and titanium can give information about the stoichiometry of the film, while the oxygen is important to evaluate the extent of oxidation. However, it must be considered, that the oxygen content is influenced by the unavoidable superficial oxidation and by the silicon oxide on which the films are deposited. Assuming that the oxygen from beneath the film "seen" by the instrument is proportional to silicon measured, a comparison with it may help.

Oxygen concentration

The first result obtained through the EDXS measurements is a qualitative information on oxygen content. As reference, the EDXS oxygen concentration value of the target is 18.4%. This oxygen is probably adsorbed or present on the surface of the target as an oxide phase and can be taken as a threshold: it is very unlikely that the deposited films will show a lower figure. However, as anticipated, the value of the oxygen content is greatly influenced by the

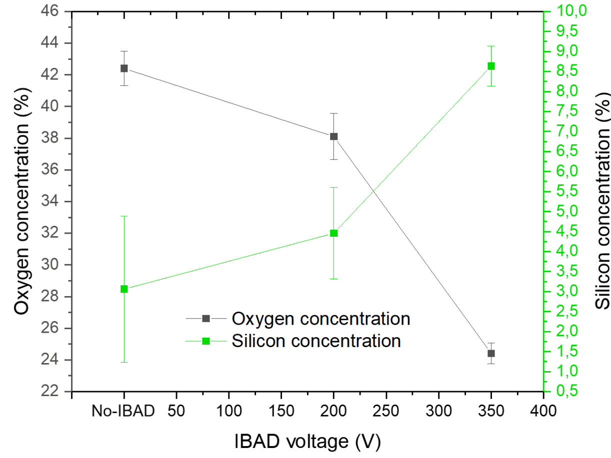

Fig. 3.3: EDXS measurements of oxygen concentration (black) and silicon concentration (green) in the samples deposited at 1.7 J/cm^2. More silicon means more silica "seen" by the instrument, hence more oxygen is expected.

silica of the substrate. Indeed, if the concentrations of oxygen were equal in all the samples, those with a lower thickness should feature higher oxygen content since the influence of the substrate is more remarkable. In figure 3.3 the EDXS concentration of oxygen in the films deposited at 1.7 J/cm^2 is reported together with the silicon one as example. It is possible to see how the silicon concentration is far from being constant in all the samples. Thus, the oxygen detected from the substrate is expected to be different depending on the specimen. For this reason, to have an idea of the EDXS concentration of the elements, that does not depend on the amount of silica detected, the atomic content was qualitatively recalculated eliminating the silicon and the oxygen that is supposed to come from the substrate. In particular, it was assumed that the stoichiometry of the amorphous silica of the substrate was SiO_2, thus the oxygen removed was two times the silicon measured. In addition, a supplementary contribution to the oxygen concentration detected by the instrument may come from the surface. It can be found both as a consequence of the oxidation of the first layers of material, or as adatoms. However, in principle, also the target should present a comparable amount of oxygen related to the presence of a surface, so it should be already considered within the 18.4% found in it.
In the graph in figure 3.4 the concentrations in the samples are presented. First of all it is immediately evident that the oxygen concentration is reduced

as the acceleration voltage increases, especially at low fluences. When the films are deposited without ion assistance, the oxygen concentration is lower in the films deposited at higher fluence, probably because they are more compact due to the higher surface mobility of the adatoms. The situation changes at 350 V, where the content of oxygen in the sample deposited at 3.1 J/cm^2 is the highest, and very similar to the one of the specimens fabricated at 1.9 J/cm^2, while the sample deposited at 1.7 J/cm^2 and 350 V that features an oxygen concentration even below 18.4%, probably due to a more effectiveness in changing the properties of the film that the ion bombardment seems to have when the fluence is low.
The issue of the presence of oxygen in the films was addressed in [1] too, and in that case the main source was identified in the residual oxygen in the nitrogen used as background gas during the deposition. In my work, the same source of gas was used to feed the plasma, thus it is possible that a portion of the oxygen in the films came from the gas supply. However, the EDXS measurements showed that the films without ion assistance are actually richer in oxygen. This is an indication that the presence of oxygen may originate from the residual oxygen in the chamber and on the surface of the target, but a definitive answer can not be given.
The reduction of the oxygen content as a consequence of the ion bombardment may arise from different phenomena. It could be caused by a more compact structure with less voids that may trap oxygen, by a sputtering action of the nitrogen atoms or due to the higher reactiveness of the nitrogen ions that, saturating the bonds of the titanium, reduces the availability of binding sites for the oxygen [61]. Indeed, in general the titanium affinity with oxygen is higher than with nitrogen. This last possibility, at least for the two lower fluences, could be supported by figure 3.5 where it is evident how the concentration of oxygen decreases, while the nitrogen increases, as if oxygen and nitrogen compete in occupying the same binding sites.

Nitrogen-titanium ratio

The value of the ratio between the atomic concentration of nitrogen and titanium, nitrogen-titanium ratio, is an indication of the film stoichiometry. To have more reliable values, the nitrogen-titanium ratio of the target was measured: the resulting value is 0.8. This figure confirms that the EDXS is not enough precise, indeed the target is known to be stoichiometric and the measured number should be 1. For this reason, the data from the samples were normalized to 0.8, that is now taken as the value that a stoichiometric film should feature.

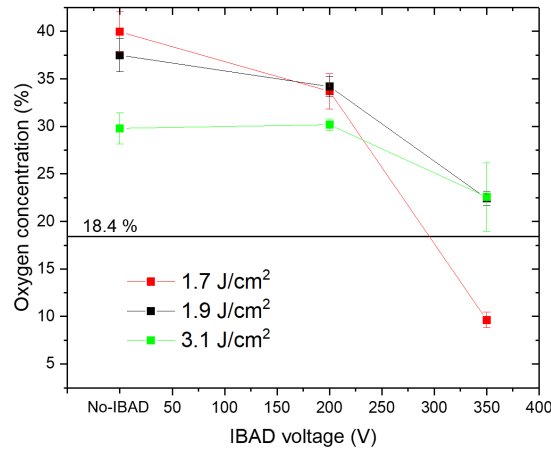

Fig. 3.4: EDXS measurements of the oxygen concentration in the as-deposited samples. The data were recalculated eliminating the oxygen from the substrate using the procedure explained in the text.

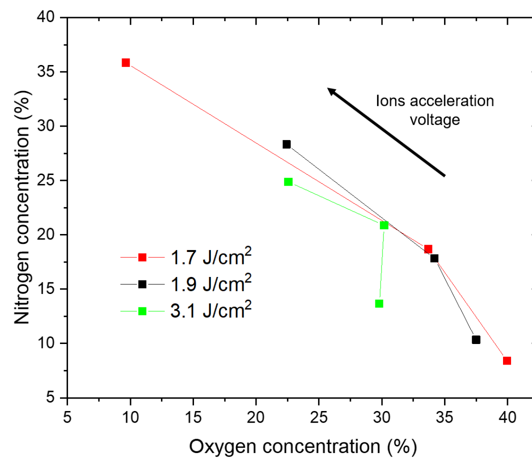

Fig. 3.5: Correlation between the nitrogen-titanium ratio and the oxygen concentration in the as-deposited samples.

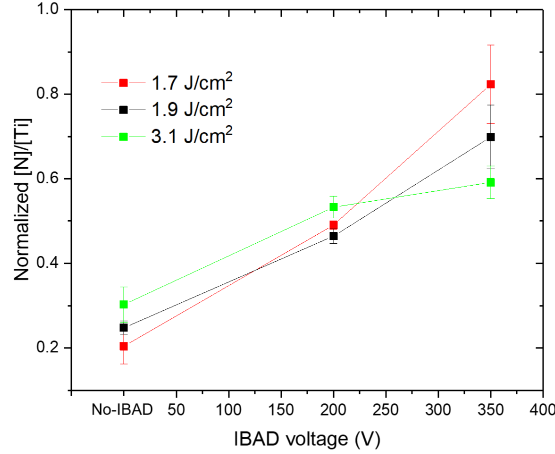

Fig. 3.6: EDXS measurements of the N/Ti ratio in the as-deposited samples normalized to 0.8, the ratio featured by the target.

In figure 3.6 the trend of the ratio between nitrogen and titanium in the nine samples is shown. First of all, it is evident that the measured ratio are lower than 1 for all the samples, in particular those deposited without ion assistance featured a very low nitrogen-titanium ratio between ~ 0.2 and ~ 0.3. These extremely low values could be related to a wider angular expansion in the plume of the light species, i.e. nitrogen, with respect to the heavy one, i.e. titanium [84]. In general, increasing the energy of the assistance nitrogen ions the ratio raises, but the behaviour changes with the fluence, probably because a lower fluence guarantees more effectiveness to the ion bombardment. Indeed, while the ratios of the samples deposited at lower fluences greatly enhance together with the ion acceleration voltage, the ratio of the samples deposited at 3.1 J/cm^2, between 200 and 350 V, increase less than between no-IBAD and 200 V.
The increase in the nitrogen-titanium ratio can be explained with many mechanisms. It could be an enrichment caused by the implantation of the nitrogen ions in the growing film, but it can also be a more complicated phenomenon resulted from the activation of the nitrogen from the plume by the impinging ions. This last mechanism would increase the reactiveness of the species in the plume favouring titanium-nitrogen bonds. To shed light on the mechanism that led to this enrichment, a complementary deposition of a film with argon ion assistance was carried out. The EDXS results were comparable to a film deposited without assisting ions (in the same conditions),

hence it is reasonable to assume that the effect of nitrogen enrichment is a direct consequence of ion implantation and does not involve the activation of the species from the plume.

3.1.2 Raman analysis

The analysis of the Raman spectra of the samples can provide several information on stoichiometry, film quality and crystallinity. The explanation of the main features of the Raman spectrum of TiN are presented in section 2.3, together with a reference Raman spectra of a stoichiometric TiN film obtained through Pulsed Laser-Scattered Ballistic Deposition (PLSBD) from [75] (fig.2.6). As usual, the analysis are made by comparing different ion energy and different fluences.
In figure 3.7 the spectra of the samples deposited at different fluence are presented comparing the effect of the ion assistance voltage. First of all, it is possible to note the almost complete absence of the band associated to the nitrogen at 600 cm^{-1}, if compared to the spectrum of the PLSBD film, with the exception of the samples deposited with low fluence and with assisting ion voltage of 350 V. This absence can be explained as a shortage of nitrogen or as a shortage of titanium vacancies. It is hard to explain such great difference between the two deposition techniques, but it was observed by Garattoni [1] and Mazza [69] in their thesis works too. In the Raman spectra in figure 3.7, two main trends as the ion voltage increases could be recognized:

- The first one is a blue shift of the titanium peak. All the evidences from the EDXS measurements seem to agree on the rise of the nitrogen content as the voltage increases. Hence, it is easy to associate this shift to an increase in the nitrogen content. However, in literature some authors reported the opposite [79, 85] meaning that this phenomenon may have different origins, for example the size of the grains or the structure of the film.

- A further evidence of the increased concentration of nitrogen, as the energy of the assisting ions rises, is a slight growth of the nitrogen peak. The trend becomes more evident as the fluence decreases, since the assistance of the ions becomes more effective. This phenomenon is well visible in figures 3.7a and 3.7b, where the nitrogen band, completely absent with no ion assistance, at 350 V, is well defined. However, it is

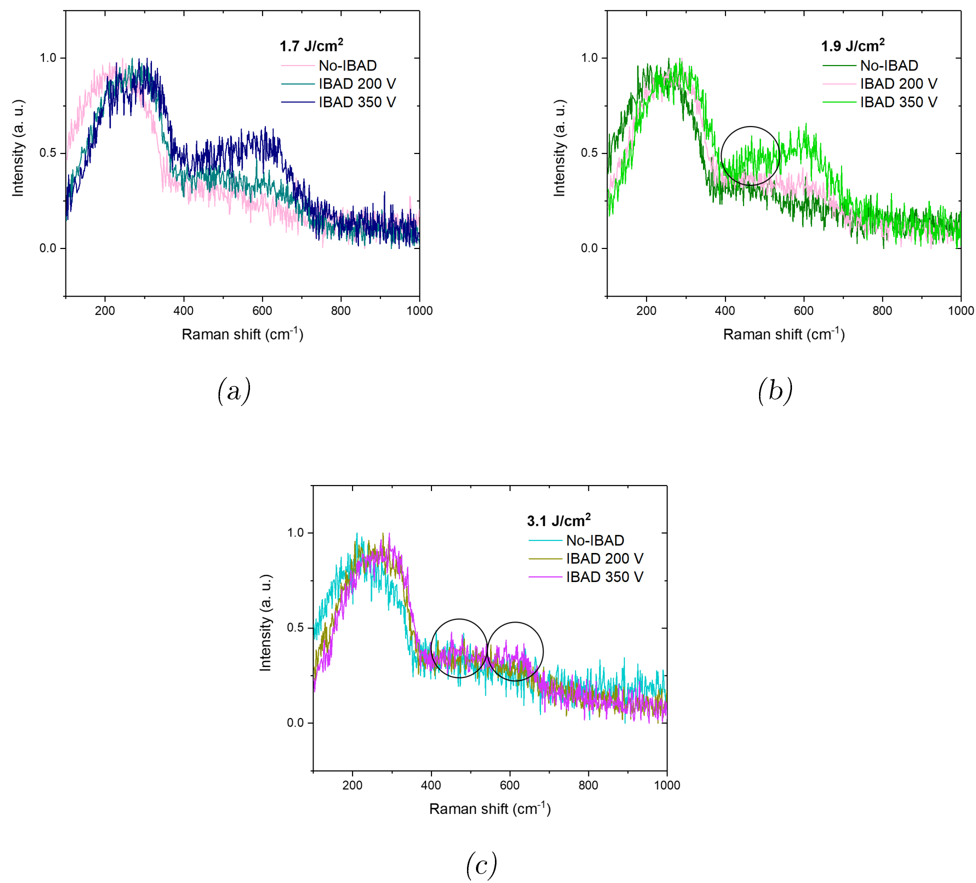

Fig. 3.7: Raman spectra depending on the assisting ion acceleration voltage of the samples deposited at 1.7 J/cm^2 *(a)*, 1.9 J/cm^2 *(b)* and 3.1 J/cm^2 *(c)*.

much lower and slightly blue-shifted with respect to the spectrum of the PLSBD sample (fig.2.6). Similar differences are reported by Trenczek-Zajac et al. in [79], where reactive sputtering TiN films were deposited with different oxygen fluxes. The Raman spectra obtained are shown in figure 3.8, and it can be seen that those associated to an oxygen flux of 0.46 and 0.66 *sccm* are very similar to the spectra of the samples fabricated at 1.7 and 1.9 J/cm^2 with 350 V. Thus, these modified spectra can be the result of the presence of an oxide phase of the type TiO_xN_y in the samples that, as the oxygen concentration increases, leads to the loss of all the features of the TiN Raman spectrum. It is reasonable to assume that this oxide phase is present in all the samples, but those deviations can not be observed due to the absence of the band.

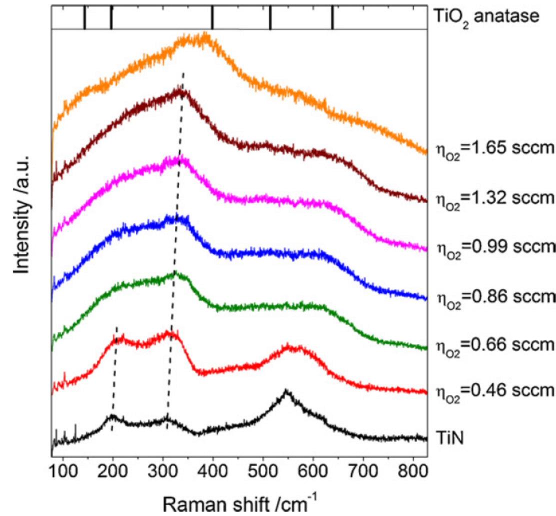

Fig. 3.8: Raman spectra of reactive magnetron sputtering TiO_xN_y depending on the flux of oxygen during the deposition. Taken from [79].

- The presence of an oxide phase in the films can be associated to the presence of two small bands that some samples spectra have, the first one between the nitrogen and titanium band, the second one slightly blue-shifted with respect to the nitrogen band of the TiN spectrum. These bands are in a very similar position to those circled in the Raman spectrum of amorphous TiO_x, presented in figure 3.9, and may be associated to it. Nevertheless, the second one can also be related to a higher nitrogen content, as very close in position to the nitrogen band of

TiN spectrum. Indeed, it could also be, that this TiO_x band influenced the nitrogen band, causing the blue-shift observed in the samples where the 600 cm^{-1} band is present. These small features are well visible in the films deposited at 1.9 and 3.1 J/cm^2 with 350 V (fig.3.7b and fig.3.7c), where they are highlighted with circles. However, the height of these bands can not be used for a quantitative comparison on the extent of oxidation. Indeed, taking as example the samples deposited at 3.1 J/cm^2, the bands are more visible in the film fabricated with the highest ion voltage that, according to the EDXS data, should feature the lowest oxygen content. Thus, their height is like to be related to other effects, probably linked with the crystallinity.

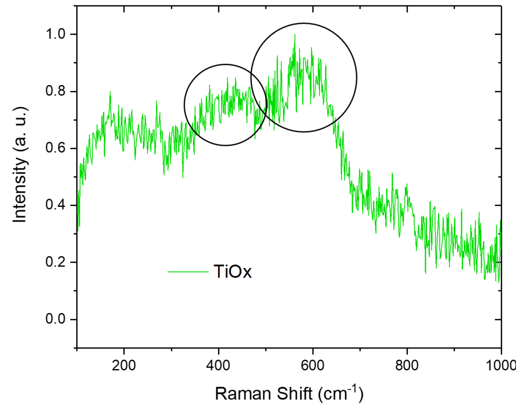

Fig. 3.9: Raman spectrum of an amorphous TiO_x film obtained by PLD by the research group. The black circles highlight the bands that may have influenced the Raman spectra of the TiN samples.

The spectrum featured by the sample deposited at 1.7 J/cm^2 with 350 V, highlighted in figure 3.10, has another peculiar feature. Apart from the rather high and well defined band at 600 cm^{-1} associated with higher nitrogen content, it is interesting the presence of a double peak in the band below 400 cm^{-1}, associated to the titanium. These peaks are clearly visible in the reference spectrum (fig.2.6) and are associated to the transverse and longitudinal acustic modes of titanium ions respectively. In the other samples only the second peak is present, the longitudinal one. Since the acustic vibrations of the heavy Ti^{4+} ions are activated by the nitrogen vacancies on the edges of the cubic structure [75], it is probable that the presence of these peaks is

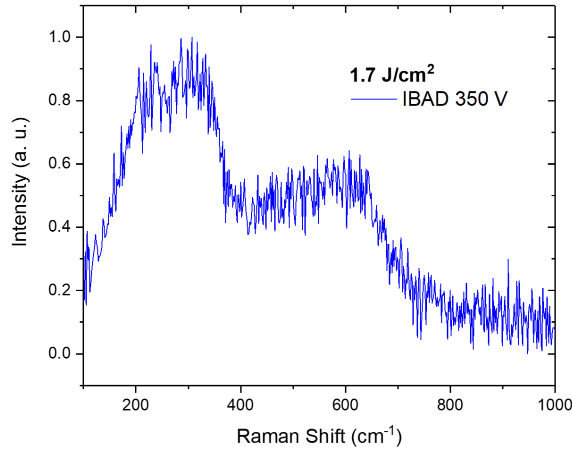

Fig. 3.10: Raman spectrum of the sample deposited at 1.7 J/cm^2 and ion acceleration at 350 V.

a qualitative indications that this sample features a more ordered structure with respect to the others, probably due to the higher stoichiometry and the lower oxygen content. Indeed, in figure 3.8, the double peak of titanium is visible only with low fluxes of oxygen.

Since the Raman spectrum of TiN relies on the presence of vacancies of titanium and nitrogen, thus local defects, it can not give information about the crystalline quality nor the disorder in the film. To have a more complete understanding of the overall crystalline quality of the film, in particular of the blue-shift of the band below 400 cm^{-1} and of the complete absence of the band at 600 cm^{-1} in the majority of the samples, XRD measurements are necessary.
According to Raman and EDXS analysis, the film that shows the best features, i.e. the band at 600 cm^{-1} and the double peak in the titanium band, is the one deposited at the lowest fluence and highest assisting ion voltage. However, even if it features both the bands, as the one deposited at 1.9 J/cm^2, the band at 600 cm^{-1} is very weak and blue-shifted, highlighting the presence of an oxide phase in the films.

3.1.3 Electrical measurements

The electrical properties that can be measured through the apparatus explained in section 2.4 are: the resistivity of the film (ρ), the density of electrons (n) and the mobility of the carriers (μ). For a plasmonic material, it is mandatory that the electron losses are as low as possible [10], thus, among all these quantities, the mobility is probably the most important. In fact, it is directly proportional to the mean free path through the mean time between two scattering events (τ):

$$\mu = \frac{q_e}{m_e}\tau. \tag{3.1}$$

In turn, the mean free path is related to the quality of the lattice. Indeed, it decreases as the density of the scattering centres, such as defects, grain boundaries, inclusions or stoichiometry variations, gets higher.
In figure 3.11, the mobility values of the as-deposited samples are shown.When the deposition is carried out without ion assistance, the smallest mobility is featured by the sample deposited at the lowest fluence. As the deposition is carried out with assisting ions, the mobility increases in all the specimens. While the mobility of the samples deposited at 3.1 J/cm^2 features its maximum at 200 V, increasing the voltage to 350 V, the mobility of the specimens deposited at 1.7 J/cm^2 and 1.9 J/cm^2 enhance further, up to approximately 0.4 cm^2/V s. The mobility of these samples is now higher than the one of the sample deposited at 3.1 J/cm^2. Unfortunately, due to instrumental limits, it was not possible to increase further the voltage to observe the following trend. The increase in the mobility may be associated to a less defective lattice of the film. This would be in accordance with the qualitative observations made on the cross section of the samples deposited at the lowest fluence, where the columnar grains seem to improve the smoothness as the voltage increases. A second possibility could be the better stoichiometry and the lower oxygen concentration in the films deposited with ion assistance (according to the EDXS measurements). Indeed, oxygen acts as a defect within the film and may increase the electron loss. However, without any information on the crystallinity of the films it is hard to define the origin of this trend in the mobility.
The values of mobility featured by the no-IBAD films are particularly low, in literature similar values are reported, as 0.15 cm/V s in [86], or even lower, as 0.04 cm/V s in [87], but for sub-stoichiometric films deposited by atmospheric pressure PVD and reactive magnetron sputtering, respectively. The values reported for stoichiometric films may range between from 0.4 cm/V s,

reported for a non reactive sputtering film by Yu et al. in [27], to 6.7 cm/V s, found in a monocrystalline reactive sputtering sample [88], or even 36 cm/V s measured for heteroepitaxyal PLD TiN deposited with the substrate heated at 700°C by Xiang, Liu, and Zhang in [28]. In conclusion, only the samples deposited with ion assistance have mobility values that are close to those reported for stoichiometric films, but still low, probably due to a defective structure of the films.

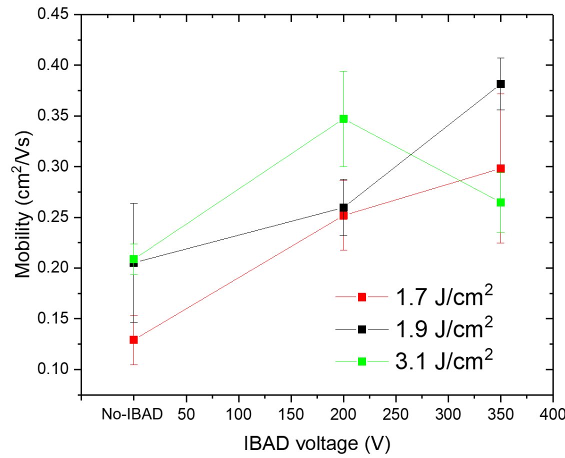

Fig. 3.11: Mobility data depending on the fluence and the assisting ion acceleration voltage.

While the mobility is affected by the crystalline quality, the electronic density depends primary on the stoichiometry: as explained in section 1.3, the more nitrogen is present, the lower is the carrier concentration. However, defects in the lattice that act as traps for the electrons can effectively reduce the electronic density too. In figure 3.12 the data about the electronic density in the films are presented. It is observed a decreasing trend as the assisting ion acceleration is increased, with the exception of the samples deposited at 3.1 J/cm^2 and 350 V. The nitrogen-titanium ratio and the electronic density are correlated in figure 3.13. The simple use of ion assisted deposition appears to be more efficient in reducing the electronic concentration than the enhancement of the voltage. Indeed, the difference between the No-IBAD and the IBAD-200V conditions, in terms of density of electrons, is much higher than between IBAD-200V and IBAD-350V, even if the concentration of nitrogen increases in both cases. In particular, the concentration of elec-

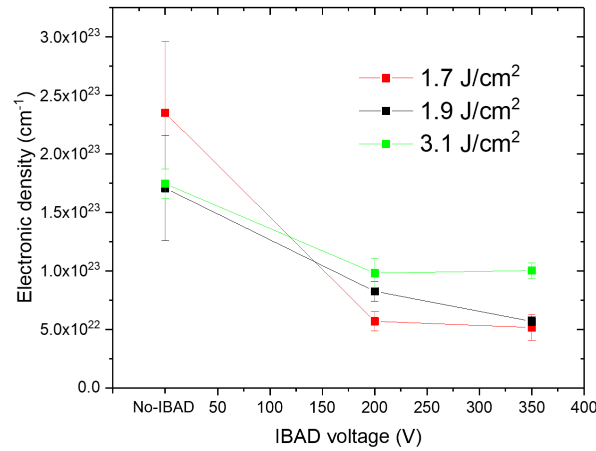

Fig. 3.12: Electronic density data depending on the fluence and the assisting ion acceleration voltage.

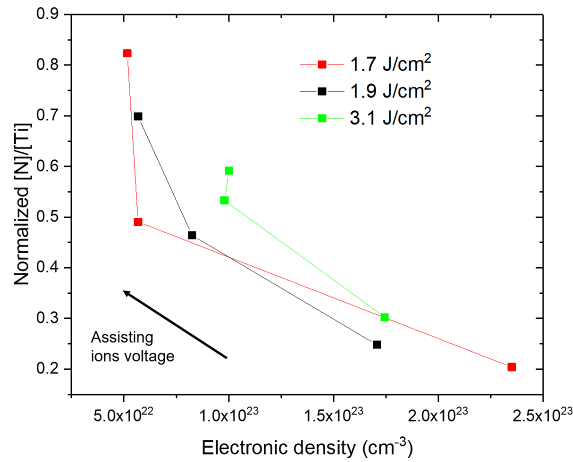

Fig. 3.13: Correlation between the nitrogen-titanium ratio and the electronic density in the films depending on the assisting ion voltage and the fluence.

trons in the sample deposited at 3.1 J/cm^2 and 350 V slightly increases with respect to the one at 200 V, despite the enhancement in the nitrogen content. Even if the correlation between nitrogen and electronic concentration seems to be in general valid, it must be considered that the enhancement in the $[N]/[Ti]$ is achieved through a bombardment with energetic ions, hence arguably with further modifications, especially in the lattice defects (e.g. traps, vacancies and grain boundaries), that in turns have influences on the density of electrons. Thus, as shown in figure 3.13, the correlation with the stoichiometry is not linear as one could imagine.
For a stoichiometric film deposited by reactive sputtering and substrate heated at 600°C Patsalas and Logothetidis in [22] reported 5.5×10^{22} cm^{-3}, while for a high-quality single crystal sputtering film Johansson et al. found 5×10^{22} cm^{-3} in [88]. Thus, the films deposited with high ion energy and low fluence, showing values close to these, are more likely to be stoichiometric, or even slightly over-stoichiometric. However, for a quantitative discussion on the stoichiometry reliable and direct measurements are needed, as already discussed for the EDXS measurements.

The resistivity (ρ) of the samples depends on the mobility (through τ) and on the concentration of carriers according to the equation:

$$\rho = \frac{m_e}{n_e e^2 \tau}. \tag{3.2}$$

Thus, the trend presented in figure 3.14 is a combination of the previous. Indeed, focusing on the samples deposited at 1.7 and 1.9 J/cm^2, the lower value of the resistivity featured at 350 V, with respect to 200 V, can be explained observing that increasing the voltage the mobility is enhanced, but clearly this effect is not completely balanced by the decrease in the electronic density. On the other hand, for the samples fabricated at 3.1 J/cm^2, the mobility at 350 V decreases compared to the one observed at 200 V, while the electronic density remains substantially constant: as expected this results in a higher resistivity at 350 V. Regardless of the possible combination of electronic density and mobility, in general, it can be observed that the resistivity increases as the fluence decreases.
The values obtained for the films deposited without ion assistance are quite high but in accordance with the literature. Indeed, while Chowdhury et al. in [85] reported, for PLD films grown under vacuum at room temperature, values as low as 0.32×10^{-4} $\Omega\,$cm, Patsalas, Kalfagiannis, and Kassavetis in [4] reported for stoichiometric films thicker than 100 nm, deposited in

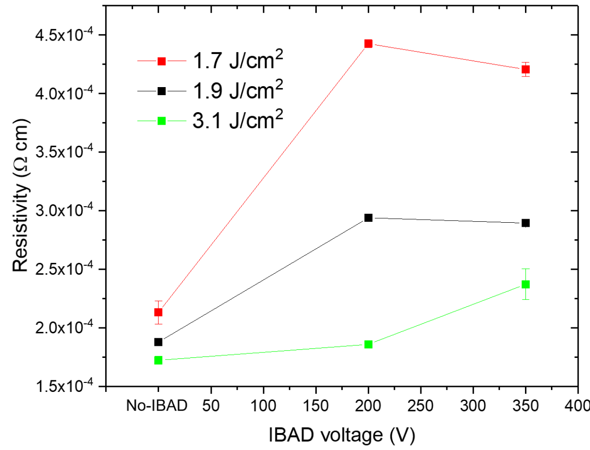

Fig. 3.14: Resistivity data depending on the fluence and the assisting ion acceleration voltage.

the same conditions, values of $\sim 1.16 \times 10^{-4}\ \Omega\,\mathrm{cm}$, just slightly lower than resistivity measured during this thesis work. However, the values obtained for the films deposited with the ion assistance are much higher, especially at low fluences. Nevertheless, it is possible to find some authors that reported similar values, as Patsalas and Logothetidis in [22] that claim a value of resistivity of $5.27 \times 10^{-4}\ \Omega\,\mathrm{cm}$ for a film deposited by reactive sputtering at room temperature and with a bias voltage of -40 V that features a nitrogen-titanium ratio of 1.1. Even if the high resistivity featured by this film may suggest to use the resistivity as a mean to understand the stoichiometry, this is very complicated to be done, especially if the conditions of fabrication are different. The resistivity can be influenced by many factors and the only way to know the exact nitrogen-titanium ratio remains a more accurate measurements of this quantity.

3.1.4 Reflectance measurements

The reflectance measurements, together with a more extensive discussion on how the quantities analysed in the following are influenced by the TiN films characteristics are explained in section 2.5. The curve represented in figure

3.15 corresponds to the sample deposited with fluence 1.7 J/cm^2 and no ion assistance and can be used as example. Indeed, the general features and the shape are comparable for all samples, with a minimum ("dip"), that in accordance with the literature, is in the region approximately between 300 and 600 nm [79–81, 89]. The characteristics of the reflectance curve taken into account for the analysis are: the value and the position of the minimum (λ_{min}), the slope of the reflectance edge after the dip and the value of the reflectance at the long wavelength limit (1200 nm). To analyse the curve dip a polynomial fitting, highlighted in red in figure 3.15, was carried out. In the same figure, in green, it is also pointed out the region where a linear interpolation of the reflectance edge was performed to measure the slope. As example, in figure 3.16 the reflectance curves of the samples deposited at 1.9 J/cm^2 are compared to highlight the dependence on the ion energy, while in figure 3.17 those of the films deposited at 200 V are grouped to evidence the differences due to the fluence.

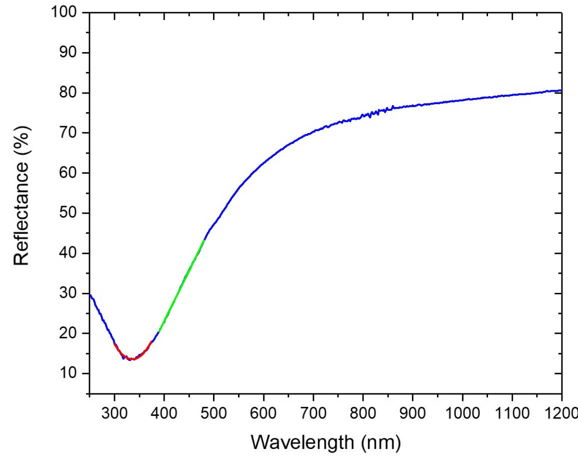

Fig. 3.15: Reflectance curve of the sample deposited at 1.7 J/cm^2 and no ion assistance. The polynomial interpolation of the dip is highlighted in red, while the linear interpolation of the reflectance edge at $\lambda > \lambda_{min}$ in green.

The positions of the minimum measured for the annealed samples are summarized if figure 3.18. The density of electrons is strictly related to the screened plasma frequency of the material; a red-shift of the ω_{sp} is observed when n decreases. Since λ_{min} is related to it, the dip is expected to red-

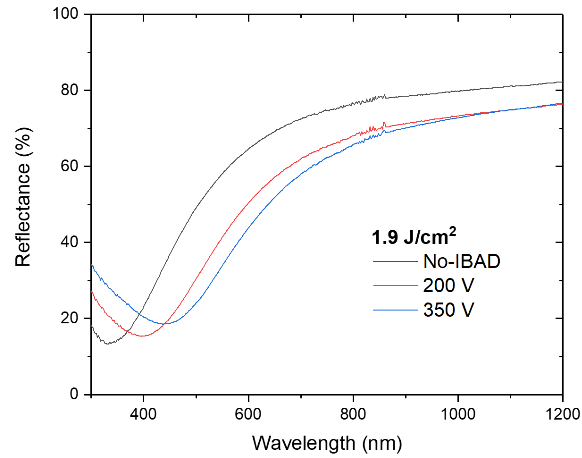

Fig. 3.16: Reflectance curves of the samples deposited at 1.9 J/cm^2, depending on the ion energy.

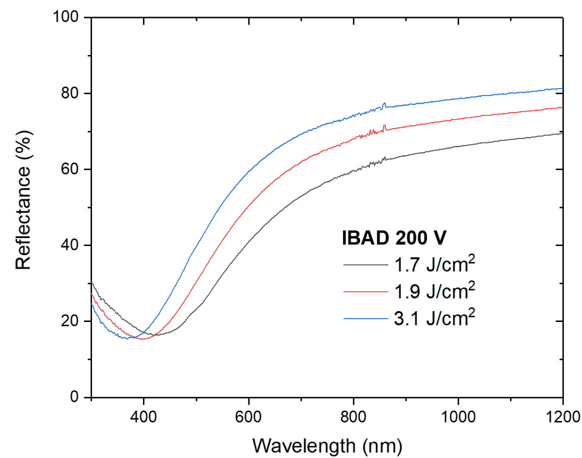

Fig. 3.17: Reflectance curves of the samples deposited at 200 V, depending on the fluence of deposition.

shift as well. Thus, the trend observed in figure 3.18, 3.17 and 3.16 can be interpreted with the values observed in figure 3.12. However, the decrease of the electronic density is not enough to explain the trend of the minimum of reflectance. Indeed, while the electronic density can be considered roughly constant between the samples deposited at 200 and 350 V, the reflectance minimum evidently continues to red-shift, in particular in the low fluence films. Thus, it is clear that the shifting of λ_{min} can not be attributed to the electronic density only. An additional explanation to the red-shift in the dip could be the enhancement of the stoichiometry as the ion assistance voltage increases, observed with the EDXS measurements. This hypothesis is well represented in figure 3.19, where the nitrogen-titanium ratio is correlated to the position of λ_{min}. Indeed, as explained in section 2.5, the more nitrogen is present the more red-shift is the wavelength at which $\epsilon_1 = 0$, namely ω_{sp}. This causes a further red-shift of λ_{min}, even if n remains almost constant.

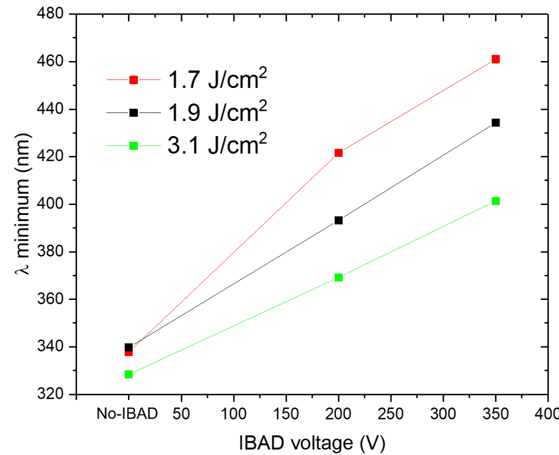

Fig. 3.18: Position of the minimum of reflectance (λ_{min}) in the as-deposited samples as a function of the ion energy and fluence of deposition.

The data on the slope, presented in figure 3.20, are important to assess the quality of the lattice and the composition of the films, indeed, a lower value of the slope is usually associated the presence of an oxide phase, inclusions or other type of defects (section 2.5). In figure 3.20 it can be observed how the slope steepness decreases as the fluence is lowered and the ion acceleration voltage increased. This is likely related to an enhancement in the defects density caused by the probable low surface mobility of the ad-species at low

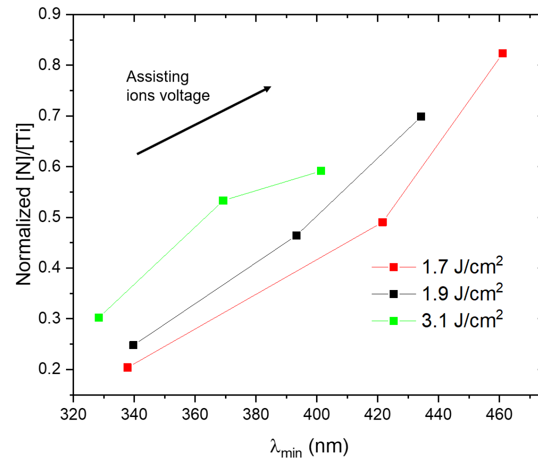

Fig. 3.19: Correlation between the nitrogen-titanium ratio and the position of the minimum of reflectance (λ_{min}) depending on the fluence of deposition and the assistance ion energy.

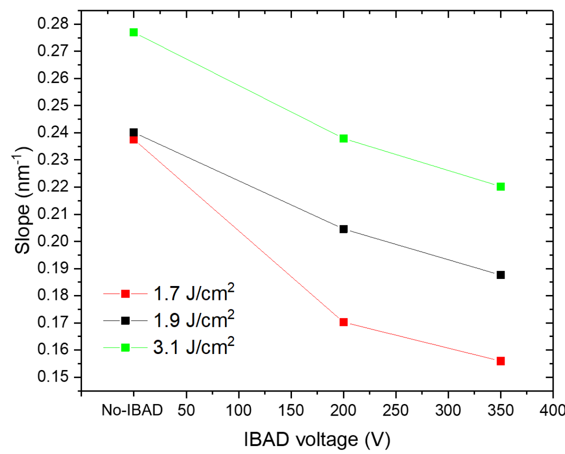

Fig. 3.20: Slope of the reflectance edge in the as-deposited samples as a function of the ion energy and fluence of deposition.

fluence and by the energetic ion bombardment. Nevertheless, it is improbable that this trend can be related to the oxygen concentration, as in [79], because the EDXS measurements show that the oxygen decreases enhancing the energy of the ions.
The higher defectiveness of the samples deposited at lower fluence and high ion energy seems to be to some extent confirmed by the values of the reflectance at 1200 nm reported in figure 3.21a, but also by the curves presented in figure 3.16 and 3.17. In theory, this value should be 100%, so, the further the data are from this number, the lower is the quality of the films. However, the reflectance value is influenced by the electronic density too: as it decreases, the light is less reflected because there are less electrons that can interact with it. Thus, the reflectance value at 1200 nm, summarized in figure 3.21a, can be explained with a combination of these two effects. In general the reflectance decreases together with the fluence. In the samples deposited with no assisting ions, it is likely that this is related to a lowering in the quality of the films, indeed the electronic density does not have such a defined dependence on the fluence (fig.3.12). On the other hand, the low reflectance of the IBAD samples is probably related to the lowering of the electronic density, but also to additional defects of the ion bombardment. However, it is hard to explain the rise in the reflectivity observed in the samples deposited at 1.7 and 1.9 J/cm^2 at 350 V. Indeed, in these sample the density of electrons slightly decreases with respect to those deposited at 200 V, hence it would be expected a lowering of the reflectance. A possible explanation to this observation could be the better stoichiometry featured by these samples with respect to the others, thus a more regular and less defective structure.
Similar concepts can be applied to explain the reflectance value at the dip (fig.3.21b), as a lower electronic density and a higher quality of the film can be related to a lower reflectance value. However, the strong influence of the interband transition in this region, red-shifted as the nitrogen content increases, makes very difficult to explain in detail the measured values (section 2.5.1). Nevertheless, it can be observed that these measurements are not in contrast with the slope results, indeed, the reflectance values at the minimum increase as the ion energy is enhanced and there is not a well defined trend with respect to the fluence.

Overall, the analysis of the reflectance curves suggest that the quality of the films decreases as the ion assistance is enhanced and the fluence lowered. However, these results partially disagree with the data on the mobility of the carriers. In fact, the mobility grows as the ion voltage is increased and this can be explained assuming less defective films. Nevertheless, the

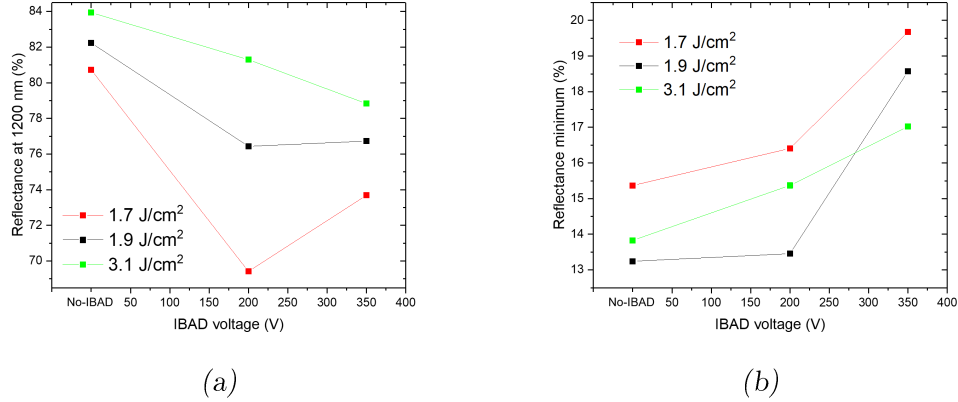

(a) *(b)*

Fig. 3.21: Reflectance value at 1200 nm *(a)* and at the minimum *(b)* of the as-deposited samples as a function of the ion acceleration voltage and the fluence of deposition.

enhancement in the mobility could be related to effects, e.g. improved dimension of the grains, that does not necessary have heavy consequences on the reflectance. On the other hand, the changes in the reflectance curve may be due to defects or impurities that does not affect greatly the mobility. These are just hypothesis, but without further information, especially on the crystallinity, it is difficult to make more accurate statements.

3.1.5 Conclusions

The effect of the ion bombardment is clearly to increase the concentration of nitrogen. Moreover, even if a modest concentration of oxygen is present in all the samples, the EDXS measurements highlighted that the nitrogen ion assistance had the side effect of reducing the oxygen concentration in the film. The values measured are well below those reported in the previous thesis of the group [1, 69]. Thus, the effect of the IBAD is twofold and resulted to be more effective in increasing the nitrogen content than the background gas during the deposition tested in [1].
For low fluences of depositions, increasing the energy of the ions, the mobility of the electrons is enhanced. However, under the same conditions the overall quality of the film seems to be lower, according to the reflectance data, where the best characteristics are found for the sample deposited with the highest

fluence and no-IBAD. The disagreement between these two analysis makes difficult to define which fluence and voltage is the best, that, on the other hand, was clear for the EDXS measurements. Nevertheless, the film deposited at 1.7 J/cm^2 and 350 V is the only one that features the best characteristics in more than one measurement technique. Indeed, it has the best stoichiometry, the lowest oxygen concentration and the highest mobility.

3.2 Effect of the thermal treatments

The aim of the thermal treatments on the deposited films is to improve the electrical and crystalline qualities of the samples. Phenomena like grain growth and defect healing, that may be activated upon thermal stimulus, can determine an improvement in the mobility of the carriers, increasing the mean free path of the electrons. This would lower the losses due to the scattering of the carriers guaranteeing better electrical and plasmonic behaviour.
The thermal treatments in the previous thesis work of the group [1] were carried out at 550 °C for one hour with a ramping rate oft 10°C/min. These treatments did not show any evidence of improvement. For this reason during this thesis work three different thermal treatments at higher temperature have been conducted. Two of them with the same ramping rate and time, but at 700°C and 865°C, and the last one at 865°C, but with a dwell time of 15 min. All the treatments were carried out in vacuum to avoid any possible contamination of oxygen from the background gas.

3.2.1 EDXS analysis

The EDXS measurements of the ratio between the atomic concentration of nitrogen, titanium and oxygen conducted on the annealed samples are analysed in this section. The data have been grouped by the fluence of deposition, in this way the effect of the thermal treatment is of more straightforward interpretation.

Oxygen concentration

In figure 3.22 the EDXS data of the oxygen concentration in the annealed samples are reported. As in the analysis of the as-deposited samples, the oxygen concentration was recalculated to have a more consistent comparison, removing the silicon and the portion of oxygen that should be bound to it (assuming the silica of the substrate to have SiO_2 stoichiometry). The concentration upon the thermal treatments increases in almost all the samples. At the same time, the enhancement of the oxygen concentration is more evident as the fluence increases, probably because the effect is more evident in those samples with a lower initial concentration (fig.3.4). As in the as-deposited samples, in the annealed ones, when no-IBAD depositions are

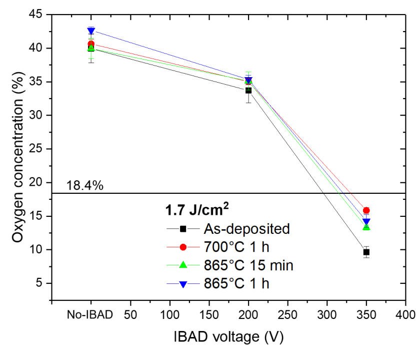

(a)

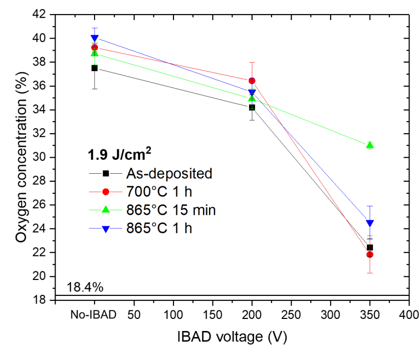

(b)

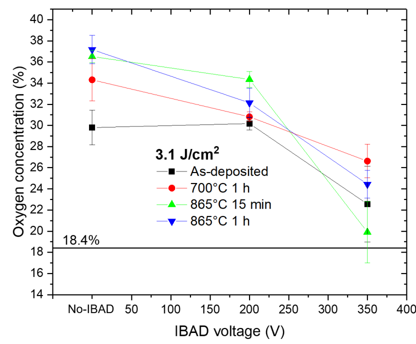

(c)

Fig. 3.22: EDXS data of the oxygen concentration depending on the thermal treatment, the deposition fluence and the assistance ion energy. The values of the as-deposited samples are reported in black

considered, the lowest oxygen concentration is featured by the films deposited at the highest fluence. On the other hand, at 350 V, the lowest oxygen concentration is recorded in the samples deposited at 1.7 J/cm^2, where it is even below 18.4% (the concentration of oxygen found in the target) whichever thermal treatment is considered. Among the samples deposited at 200 V the situation is chaotic and changes for each fluence of deposition.
In general there is not a thermal treatment that clearly limits the increase of oxygen concentration in the films. In fact, in the films deposited without ion assistance, the annealing at 865°C for one hour enhances more the content of oxygen with respect to the others, but this is no more true for the IBAD films, where the other thermal treatments cause a more consistent increment. It is interesting to note the oxygen percentage values of some samples annealed at 865°C for 15 minutes. In particular, the surprisingly high value of the oxygen concentration in the film deposited at 1.9 J/cm^2 and 350 V and, on the other hand, the low figure measured in the film deposited with the same voltage but at 1.7 J/cm^2. This trend is quite different from those of the other samples and it is difficult to explain.

Nitrogen-titanium ratio

Further important information about the effectiveness of the thermal treatments may be understood from the EDXS measurements of the ratio between nitrogen and titanium concentration in the films. As in the previous paragraph, the values were normalized at 0.8, the ratio featured in the target. In figure 3.23 all the data are summed up:

- For the samples deposited at 1.7 J/cm^2 (fig.3.23a), the effect of the thermal treatment is not particularly evident, except for the specimens annealed at 700°C. In these films the ratio appears higher with respect to the as-deposited ones in all the deposition conditions, from No-IBAD to 350 V. In this last case the ratio is even slightly higher than 1.

- At 1.9 J/cm^2 (fig.3.23b), the situation is less clear. The samples annealed at 865°C for 15 minutes have the highest ratio in the first two deposition conditions, but feature the lowest value at 350 V. This effect is probably related to the fact that the oxygen concentration is particularly high in this sample. As in the previous case, at 350 V the highest ratio is shown by the sample annealed at 700°C (~ 0.8). The samples annealed at 865°C for one hour, on the other hand, does not show any significant difference from the values of the as-deposited samples.

- The behaviour of the samples deposited at 3.1 J/cm^2 is shown in figure

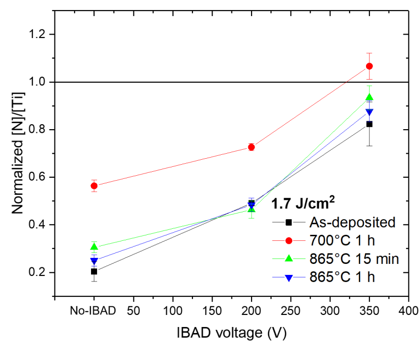

(a)

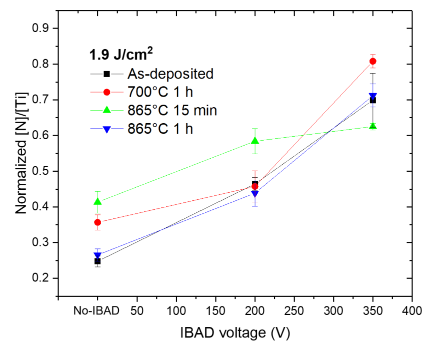

(b)

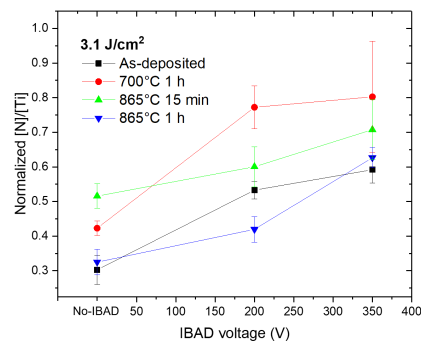

(c)

Fig. 3.23: EDXS data of the nitrogen-titanium ratio depending on the thermal treatment, the deposition fluence and the assistance ion energy. The values of the as-deposited samples are reported in black

3.23c. The samples subjected to thermal treatment at 700°C reported a remarkable increase in the nitrogen-titanium ratio (up to $\sim$ 0.8 in the IBAD samples), as at 1.7 J/cm^2. A considerable enhancement is featured by the samples annealed at 865°C for 15 minutes too, especially for those deposited without ion assistance. The thermal treatment at 865°C for one hour does not seem to have modified particularly the ratio between nitrogen and titanium in the samples, except for the sample deposited at 200 V where it decreases below the value of the as-deposited film.

Even if most of the samples changed the EDXS stoichiometry upon the thermal treatments, it is difficult to explain the increase in the nitrogen content. Indeed, there were no sources of nitrogen during the annealing, hence the atomic concentration should have been remained the same. Nevertheless, an explanation to this phenomenon is not straightforward, thus, to have a definitive answer, more accurate and reliable measurements must be carried out (e.g. XPS).
Having all considered, the samples annealed at 700°C and deposited at 1.7 J/cm^2 appear to be the most predictable and with the most homogeneous improvements in the nitrogen-titanium ratio, thus in the stoichiometry, of the films. Remarkable improvements are present in the samples deposited at higher fluence too, but are less constant as the acceleration voltage is changed. At 1.9 and 3.1 J/cm^2 also the samples annealed at 865°C for 15 minutes show some improvements, but not as homogeneous as the samples annealed at 700°C and deposited at 1.7 J/cm^2. The annealing carried out at 865°C for one hour surprisingly did not cause remarkable changes in the stoichiometry of the films. This behaviour is quite unexpected since it is the thermal treatments with the more severe conditions. Probably, such high temperature for one hour causes further modifications, with respect to the other two treatments, that may prevent any improvements in the stoichiometry.

3.2.2 Raman analysis

In general, with respect to the Raman spectra of the samples prior any thermal treatments there are just small differences. The differences, that can be associated to oxidation phenomena, are localized mostly on the transverse acustic peak of titanium ($\sim$ 300 cm^{-1}) and in the region between 400 and 700 cm^{-1}. The features appeared upon the thermal treatments are present

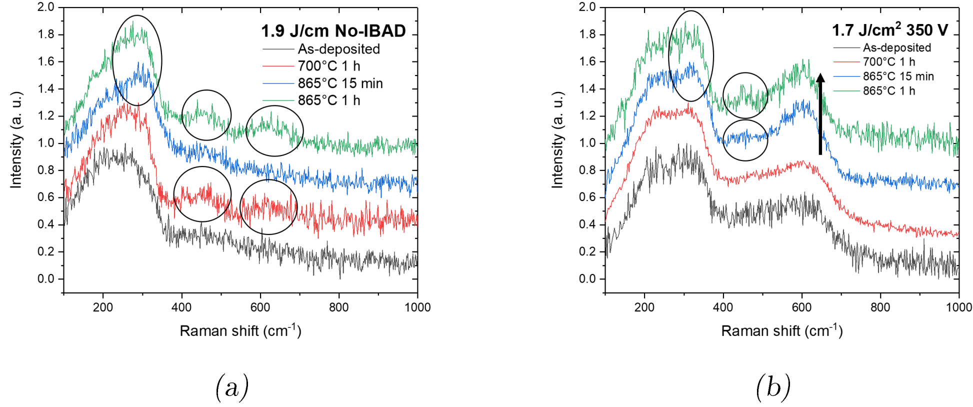

(*a*) (*b*)

Fig. 3.24: Raman spectra of the samples deposited at 1.9 J/cm^2 with no ion assistance (a) and at 1.7 J/cm^2 at ion assistance acceleration voltage of 350 V (b) depending on the thermal treatment carried out. The circles and the arrow highlight the differences with respect to the spectra of the as-deposited samples (in black).

with just small differences in all the samples. Thus, in figure 3.24, only the specimens deposited at 1.9 J/cm^2 with no ion assistance and 1.7 J/cm^2 with 350 V are reposted as significant examples.
Focusing on figure 3.24a, in the region immediately after the band of titanium it is possible to see two small bands at roughly 450 and 600 cm^{-1}. These bands were already distinguishable in some of the spectra of the as-deposited samples (figure 3.7), but only after the thermal treatment at 865°C with dwell time of one hour they become defined in all the spectra. As already discussed in section 3.1.2, the position of these two peaks is very similar to those circled in the Raman spectrum of the amorphous TiO_x in figure 3.9. However, while the first is probably associated to an oxide phase, the position of the second band is very similar to the one of the nitrogen band in TiN. Hence it is difficult to determine safely its origin: it could be either a sign of more oxygen as well as of a more stoichiometric film (as the EDXS measurements of the annealed samples confirm). The second feature highlighted in figure 3.24 is the enhancement of the peak associated to the transverse vibrational mode of titanium. A similar behaviour can be observed in figure 3.8, from [79], as the flux of oxygen is increased. However, in figure 3.8, it is observed a concurrent blue-shift of the titanium band that in figure 3.24 does not appear. Nevertheless, it is reasonable to assume that it is a consequence of oxidation of the film. In figure 3.24b, the arrow highlights another trend observed as

the annealing conditions become more severe. Indeed, it can be noted that the band between 400 and 700 cm^{-1} increases. However, since the second peak circled in the TiO_x spectra is located at approximately the same wave numbers, as for the previous samples, this growth can be explained with an increase in the oxygen content as well as with more stoichiometric films, thus with higher nitrogen content.

In conclusion, the Raman spectra are not able to define which annealing treatment is the best. Indeed, the comments made in section 3.1.2 for the two small bands, still hold. It would be very dangerous to make quantitative comparisons on the extent of oxidation based on the intensity of these features. Indeed, it could be related to many characteristics, for example to the crystallinity. Hence, the Raman results have to be taken simply as a confirm of the increase in the oxygen concentration, not as a quantitative analysis of the extent of oxidation.

3.2.3 Electrical analysis

Unfortunately, for the samples annealed it has not been possible to get direct information about the mobility and the electron density, the only information available is the resistivity. This issue is probably associated to a superficial oxidation of the specimen that altered the Hall measurements.
The resistivity recorded values are presented in figure 3.25 grouped by the fluence of deposition. It can be seen that in general the resistivity decreases after the thermal treatments. However, there are some differences depending on the fluence of deposition.

- Starting from the lowest fluence, 1.7 J/cm^2 (fig.3.25a), it is immediately evident that the only thermal treatment that increased the resistivity of the films is the one carried out at 865°C for one hour. In particular, this treatment caused a consistent increment in the film deposited at 200 V, from $\sim 4.4 \times 10^{-4}$ to $\sim 6.4 \times 10^{-4}$ $\Omega\,$cm, corresponding to the 45%. On the other hand, the other two annealing procedures caused a similar reduction of the values of the resistivity in the order of a few percent, approximately between 10 and 20%, depending on the sample. The decrease in the resistivity of the samples annealed at 700°C, that featured even an increase in the nitrogen-titanium ratio (fig.3.23a), could be related to the improvement of the regularity of the lattice. A similar explanation may be valid for the low resistivity measured in

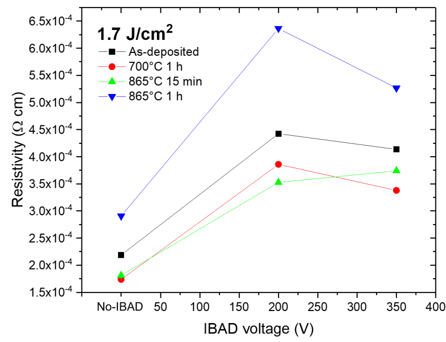

(a)

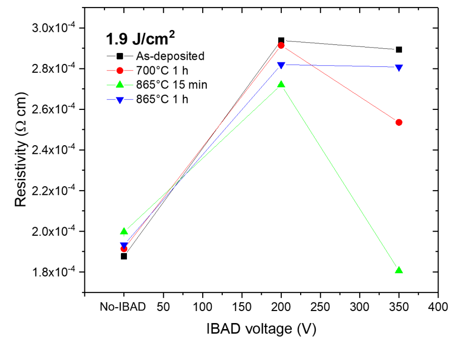

(b)

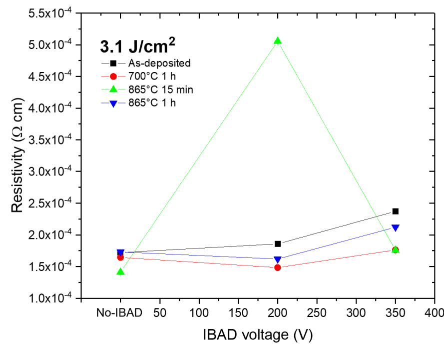

(c)

Fig. 3.25: Resistivity data after the thermal treatments of the samples deposited at 1.7 J/cm^2 *(a)*, 1.9 J/cm^2 *(b)* and 3.1 J/cm^2 *(c)* as a function of the annealing treatment and the assistance ion energy. The values of the as-deposited samples are reported in black

the samples annealed at 865°C for 15 minutes. On the other hand, the behaviour of the samples annealed at 865°C for one hour could have different origins. It could have been an oxidation issue, but the oxygen content in the film is comparable, and often lower (fig.3.22a), with respect to the samples annealed with a different treatment. Thus, it could be related to a decrease in the mobility, for example due to a highly defective lattice, or to a decrease in the electronic concentration. Indeed, even if the concentration of the carriers is mostly controlled by the stoichiometry (fig.3.13), it can also be modified by the presence of defects, such as traps. Unfortunately, without further information about the crystallinity of the samples (e.g. XRD measurements), a definitive explanation to such a different behaviours of the resistivity upon the annealing can not be given. Nevertheless, despite the decrease of the resistivity of some samples, in general, the samples deposited at 1.7 J/cm^2 still feature the highest resistivity compared to those fabricated at different fluence.

- At 1.9 J/cm^2 (fig.3.25b), all the annealed samples deposited with ion assistance feature lower resistivity with respect to the as-deposited samples. The difference becomes more evident for those deposited under the most energetic ions. Among these, the sample annealed at 865°C for 15 minutes shows a suspiciously low resistivity, with decreasing of $\sim 38\%$, from $\sim 2.9 \times 10^{-4}$ to $\sim 1.8 \times 10^{-4}$ Ω cm. In particular, it is interesting the fact that such a low resistivity corresponds to a sample that, according to the EDXS measurements, has a very high level of oxygen (fig.3.22b). On the other hand, also the samples annealed at 700°C presents a consistent decrease in resistivity between the film deposited with 200 and 350 V, but limited to $\sim 14\%$, however, this time, it could be related to the low level of oxidation. Nevertheless, we can affirm that the variations of the resistivity caused by the thermal treatments are much less consistent in the samples deposited at 1.9 than in those deposited at 1.7 J/cm^2, especially when it comes to the films fabricated without assisting ions.

- Figure 3.25c shows the resistivity of the samples fabricated at 3.1 J/cm^2. In general, it can be said that these samples continue to feature the lowest resistivity among the three different fluence of deposition with values raging roughly between 1.5×10^{-4} and 2.5×10^{-4} Ω cm, probably due to the higher electronic density derived from the low nitrogen-titanium ratio recorded (fig.3.23c). Overall, all the annealing procedure caused a lowering of the resistivity (apart from the sample annealed at 865°C

for 15 minutes) that appear to be roughly proportional to the energy of the ions during the deposition. Indeed, the percentage of decrease goes from an average −7%, for the samples deposited without IBAD, to an average −21%, for those fabricated at 350 V. As in the case of the films deposited at 1.7 J/cm^2, the samples annealed at 700°C show the lowest resistivity in most of the deposition conditions. The peak in the resistivity featured in the sample annealed for 15 minutes and deposited at 200 V does not have a straightforward explanation, indeed there is not any strange behaviour highlighted in the EDXS data for this sample.

The correlation between the EDXS measurements and the electrical resistivity has encountered some difficulties. In particular, the behaviour of the samples annealed at 865°C for 15 minutes has some singularities that hardly can be explained just using data of resistivity and atomic concentration. The decrease of the resistivity in many samples can be a consequence of a more regular structure, probably due to a more crystalline lattice. Nevertheless, information about electronic density and mobility and direct measurements of the films crystallinity are of utterly importance to give a more detailed explanation (some information may arise from the slope of the reflectance curve that will be presented later). Actually, an idea of the trend of the density of the carriers can be given by the stoichiometry of the film as explained in section 1.1 (and eventually the mobility through equation 3.2). However, figure 3.13 in section 3.1 shows the limits of this method and highlights the differences between the deposition with and without the ion assistance. Moreover, it is probable that the density of electrons is influenced by some modification or defects in the lattice that may have been introduced by the annealing treatments. Furthermore, since the missed electrical properties could not have been taken due to experimental issues, probably related to an extensive superficial oxidation, even the reliability of the resistivity can be debatable. However, with all this in mind, as highlighted by the EDXS measurements too, the thermal treatment at 700°C appears to be the most constant and reliable in improving the electrical properties. Indeed, in the case of deposition fluence of 1.7 and 3.1 J/cm^2, the samples annealed at this temperature show a better resistivity with respect to the non annealed samples, together with a higher nitrogen-titanium ratio. The trends shown by the samples annealed at higher temperature are less constant and of difficult interpretation, probably due to a different behaviour of the material at this temperature.
Nevertheless, the thermal treatments did not improve particularly the resistivity of the samples and can not be considered a successful strategy. Indeed, even though it was observed a decrease of the resistivity values in most of

the samples, the improvement was limited to a few tens of percentage points or less.

3.2.4 Optical analysis

The shape of the reflectance curves of reflectance after the thermal treatments have the same features of those of the as-deposited samples, as example the reflectance curves of the annealed samples deposited at 1.7 J/cm^2 and 350 V are reported in figure 3.26. The quantities of interest are the same analysed in section 3.1.4 and their dependence on the TiN films properties is explained in section 2.5.1.

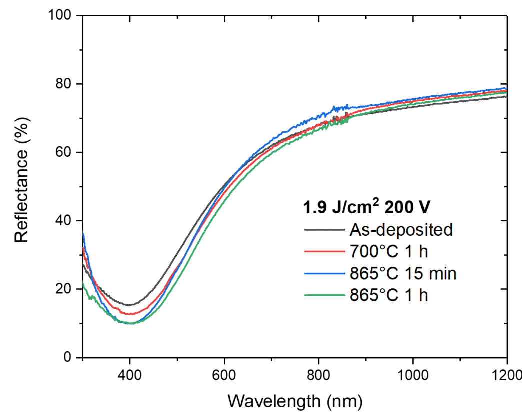

Fig. 3.26: Reflectance curves of the samples deposited at 1.9 J/cm^2 and 200 V depending on the thermal treatment. In black the curve of the as-deposited sample is reported.

In figure 3.27 the wavelength of the minimum of reflectance (λ_{min}) of the annealed samples sorted by their fluence of deposition is reported. In the graphs I compare the three different thermal treatments together with the values of the as-deposited samples to have a direct comparison. There is a general red-shift of the minimum of reflectance in almost all the samples, with the exception of the specimens deposited at 1.9 and 3.1 J/cm^2 with 350 V, but entity of the shift is smaller compared to the one caused by the ion energy or the fluence (section 3.1.4). The red-shift of the reflectance

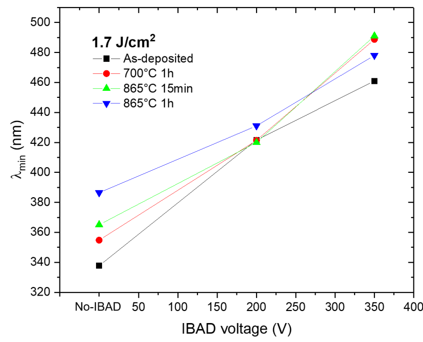

(a)

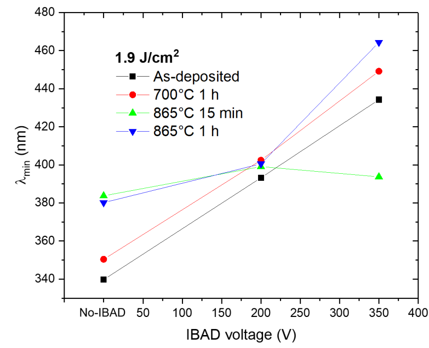

(b)

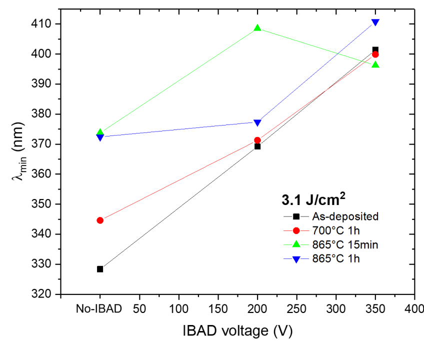

(c)

Fig. 3.27: Position of the reflectance minimum (λ_{min}) of the annealed samples deposited at 1.7 J/cm^2 *(a)*, 1.9 J/cm^2 *(b)* and 3.1 J/cm^2 *(c)* depending on the assisting ion voltage and the thermal treatment. The values of the as-deposited samples are reported in black.

minimum could be explained by a lowering in the electronic density. This would be in accordance with the increased oxygen concentration featured by almost all the films. Indeed, both nitrogen and oxygen reduce the overall density of carriers when their content increases. Moreover, it has to be said that, according to the EDXS analysis, many samples featured a higher nitrogen-titanium ratio after the annealing, that may have contributed to the red-shift. It is interesting to note, that the two samples annealed at 865°C for 15 minutes, that featured a strange behaviour in the analysis of the resistivity (fig.3.25), present singular values in the λ_{min} value too (fig.3.27b and fig.3.27c). For the first one, deposited at 1.9 J/cm^2 with 350 V, a high oxygen concentration is reported (fig.3.22b), but, for the sample deposited at 3.1 J/cm^2, the EDXS analysis are in accordance with the other specimens. However, focusing the attention on the analysis of the slope of the plasmonic edge reported in figure 3.28, it can be noted that this last film features a very low value, if compared to the others annealed samples. A low value of the slope can be a sign of major lattice defects (section 2.5.1) and can be an explanation of the strange behaviour of the specimen.
More in general, the slope of the films increases as a consequence of the thermal treatments for almost all the samples deposited with ion assistance, even if there is not a thermal treatment that causes the highest increase of the slope in all conditions. Such enhancement, that becomes more consistent as the voltage increases, can be associated to some extent to a healing effect of the defects caused by the bombardments of the energetic species. On the other hand, the slope decreases in samples deposited at 1.7 and 3.1 J/cm^2 without ion assistance (and in the sample annealed at 865°C for one hour deposited at 1.9 J/cm^2). The lowering registered for the samples deposited without the ion bombardment could be caused by some defects introduced by oxygen. These defects are likely present in the IBAD samples too, but their effect is outbalanced by the healing one. Indeed, since these films appear to be the most defective prior the thermal treatments, according to the slope values of the as-deposited value, it is likely that the healing effect is more consistent with respect to the no-IBAD films.
The measurements made on the value of the reflectance minimum are presented in figure 3.29. The IBAD samples feature a consistent lowering of the values, especially at high deposition fluences and high treatment temperature. On the other hand, the changes of the no-IBAD sample depend greatly on the annealing process carried out. Those heated at 700°C registered consistent increments, while those treated at 865°C tend to decrease the reflectance, with the exception of the samples annealed for one hour and deposited at 1.9 and 3.1 J/cm^2. As explained in section 2.5.1, a lower value of the reflectivity minimum can be associated to many factors, among these:

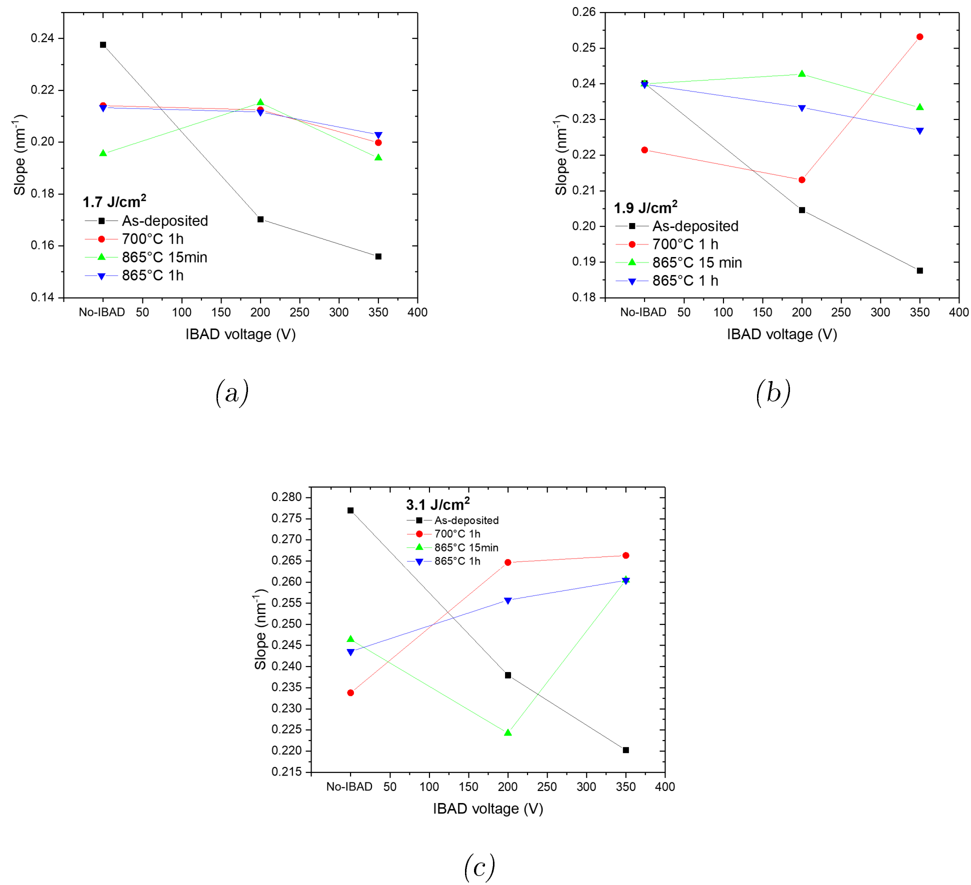

Fig. 3.28: Values of the slope of the reflectance edge after λ_{min} for the annealed samples deposited at 1.7 J/cm^2 *(a)*, 1.9 J/cm^2 *(b)* and 3.1 J/cm^2 *(c)* depending on the assisting ions voltage and the thermal treatment. The values of the as-deposited samples are reported in black.

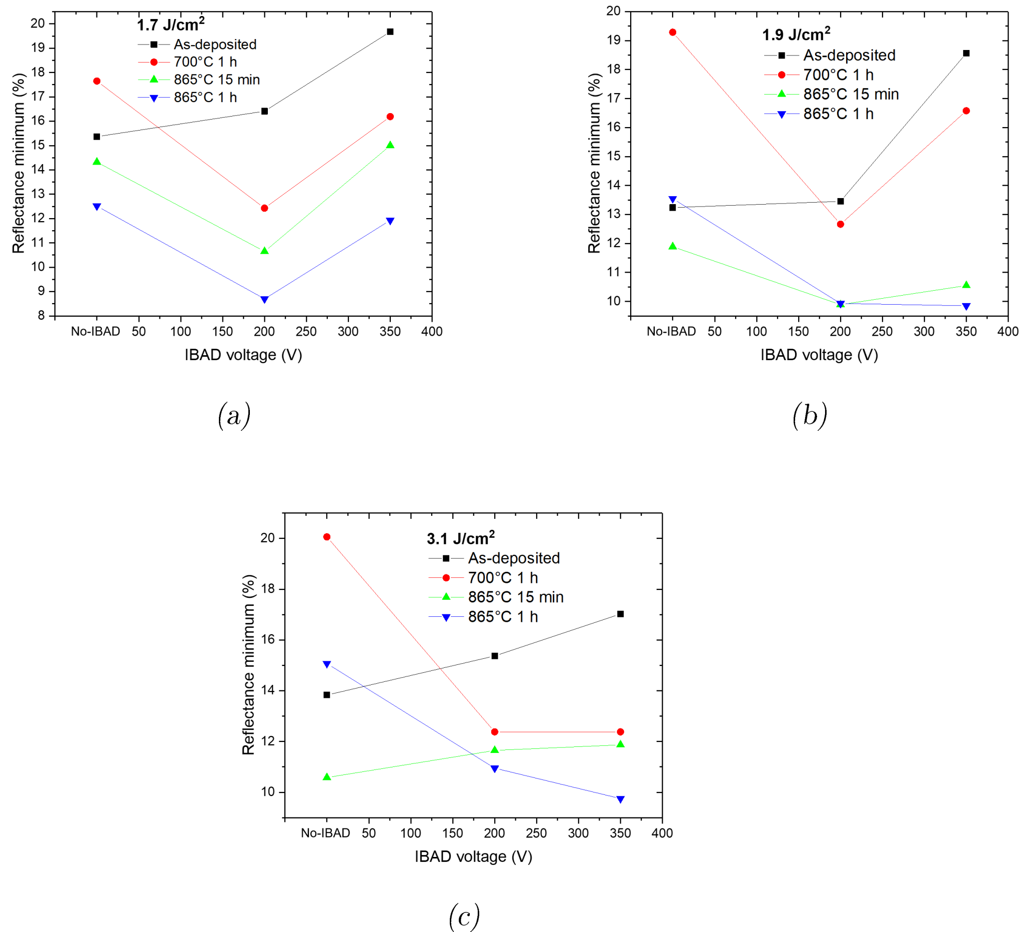

Fig. 3.29: Data of the values of the minimum of reflectance for the annealed samples deposited at 1.7 J/cm^2 *(a)*, 1.9 J/cm^2 *(b)* and 3.1 J/cm^2 *(c)* depending on the assisting ion voltage and the thermal treatment. The values of the as-deposited samples are reported in black.

a higher lattice quality and a lower carrier density, that would be in accordance to the increased stoichiometry and slope steepness.
Also the value of the reflectance at 1200 nm can be an indicator of the lattice quality and the electronic concentration of the films, in particular, the reflectance should increase together with them. The data are summarized in figure 3.30. The samples annealed at 700 and 865°C for one hour clearly improved the reflectance with respect to the as-deposited samples. This can be a consequence of a healing effect during the thermal treatments, in agreements with the previous observations on the other properties. On the other hand, the films annealed at 865°C for 15 minutes feature a trend of difficult interpretation, as it was already observed during the previous analysis. It is a confirmation that this thermal treatment is less predictable with respect to the other. The reason of this behaviour can not be easily explained as it could be either caused by the shorter dwell time or by some sort of issue occurred during the treatment.

To sum up, the optical measurements reported a general red-shift, with a few exceptions, in the annealed films with respect to the as-deposited ones. Typically, this behaviour is justified with a decrease of the electronic density, however, since it was not available for the annealed samples, this hypothesis can not be verified. The other optical features analysed, in contrast to the the resistivity measurements, seem to indicated the annealing treatments at higher temperature as those to be chosen. Indeed, the trends observed in the reflectance edge slope and in the reflectance value at the dip and at 1200 nm suggest that these treatment may favour a more extensive improvement of the film quality with respect to the annealing carried out at 700°C.

3.2.5 Conclusions

All the annealed films featured an increase in the oxygen concentration. Nevertheless, the thermal treatment that seems to have improved the most the characteristic of the film, from the point of view of the nitrogen-titanium ratio, is the one carried out at 700°C, especially when conducted on the samples deposited at 1.7 J/cm^2. Moreover, among the three, it is the one that appears to be more predictable and coherent over all the deposition conditions. On the other hand, the less foreseeable is for sure the annealing conducted at 865°C for 15 minutes, that seems to have caused evident modifications in some samples, probably due to an extensive oxidation.

Similar conclusions can be drawn when it comes to analyse the data on the resistivity of the samples, where the annealing carried out at 700°C guarantees more predictable results. Nevertheless, the limited improvement in the resistivity values suggests that the thermal treatments conducted might not be the right strategy to be endorsed to enhance the electrical characteristics of the films. Moreover, the results of the reflectance measurements disagree with the previous analysis. In fact, they indicate the thermal treatments conducted at 865°C as those that could favour a more consistent improvement in the film quality. Thus a precise indication on which annealing treatment is the best can not be given, and probably it could be different depending on which characteristic of the film is more important to improve.

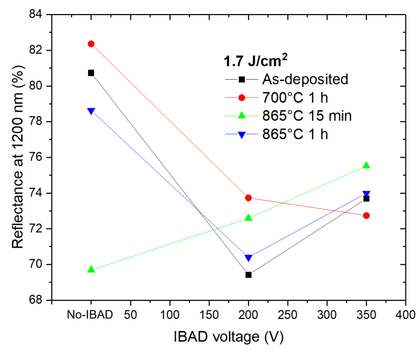

(a)

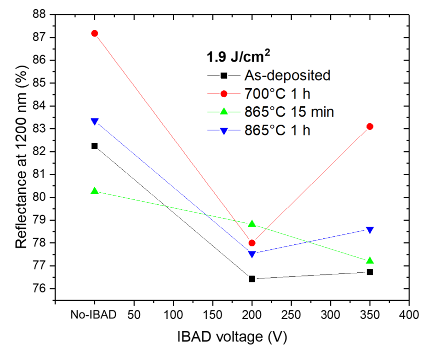

(b)

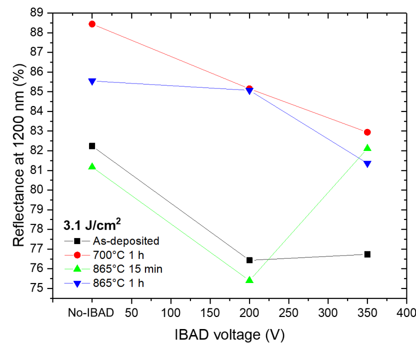

(c)

Fig. 3.30: Data of the value of the reflectance at 1200 nm for the annealed samples deposited at 1.7 J/cm^2 *(a)*, 1. J/cm^2 *(b)* and 3.1 J/cm^2 *(c)* depending on the assisting ion voltage and the thermal treatment. The values of the as-deposited samples are reported in black.

4. THICKNESS DEPENDENT ANALYSIS

4.1 Residual stress

The residual stress in the films can be source of defects and dislocations that act as scattering source for the electrons, reducing the electrical characteristics [10]. Hence, it might be very important to have a knowledge of the entity of such stress in order to reduce their value. Moreover, the study of the stress as a function of the sample thickness can provide information on the growth mechanisms of the films. The analysis of the residual stress in the films was carried out with the experimental setup described in section 2.7. The measurements were conducted on a total of 16 samples. Half of them were deposited without ion assistance and, the remaining, with ion acceleration voltage set at 350 V. All the films have been fabricated with a fluence of 1.7 J/cm^2 to maximize the differences between IBAD and no-IBAD samples (as noted in the previous chapter). The films were deposited in pair, to have a minimum of statistics, and with four different thickness, from $\sim$ 50 and $\sim$ 350 nm. As for the samples analysed in the previous chapter, the thickness of the films was measured from SEM cross-section imagines.

4.1.1 Results

The results of the analysis of the residual stress in the films are presented in figure 4.1. The state of stress that features a positive value is tensile, on the contrary, the negative one is compressive. A compressive state was measured in almost all the samples analysed, with a value of approximately -2 GPa, in accordance with the literature [39, 41, 42, 48]. However, when the thickness is decreased below 100 nm, the differences between the two deposition conditions start to appear. Indeed, below this thickness, the samples deposited with ion assistance feature the highest compressive stress measured, reaching

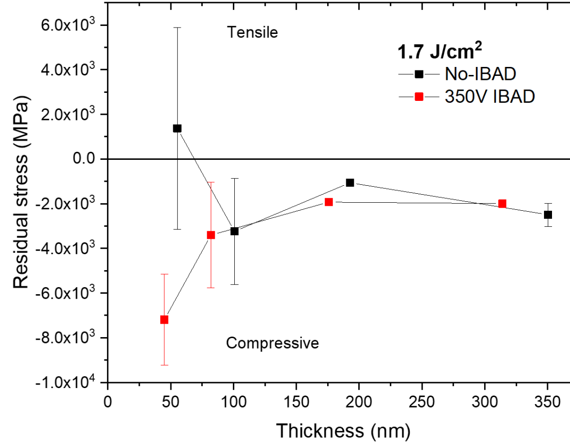

Fig. 4.1: Residual stress trend as a function of the thickness. In black the samples deposited with no ion assistance, in red those with ion acceleration voltage of 350 V. Positive values are related to a tensile residual stress, negative to a compressive stress.

approximately −7 GPa, while, the samples deposited without ion assistance, a tensile mean stress. However, the tensile value reported for this condition must be considered with care, being the average between a positive and a negative value measured for the two equivalent samples deposited in the same run.

From these preliminary observations, it seems that the effect of the Ion Beam Assisted Deposition on the stress state of the films is negligible above a threshold thickness, approximately 100 nm. This result was not predicted, indeed, the bombardment of the ions could induce some defects in the lattice and, possibly an effect of compaction. These phenomena are usually referred to as source of compressive stress [41, 68], thus lower values of stress in the IBAD films were expected. Nevertheless, it is also known that the films tend to relax the internal stresses as the thickness increases [10], mitigating, or even removing, the compressive stress accumulated.

Focusing the attention on the thinnest samples, the tensile stress featured by the film deposited without ion assistance and 55 nm thick could be interpreted as a proof of the *Volmer-Weber* growth mechanism. This behaviour is observed when the growth of the film starts from some nucleation islands that, as the thickness increases, grow and eventually coalesce. This type of growth is very common, it is featured by TiN films in many deposition

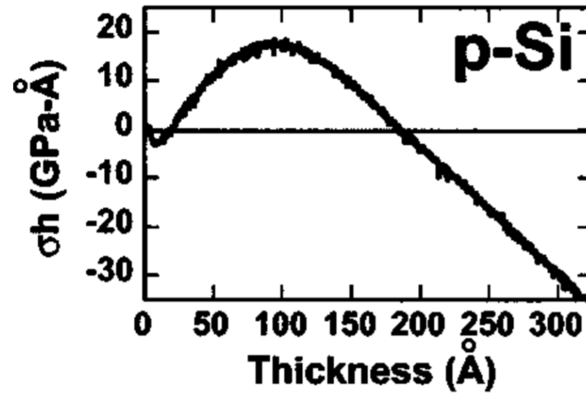

Fig. 4.2: Stress evolution as a function of the thickness of a polycrystalline silicon film deposited via electron beam evaporation. It is possible to see the typical compressive-tensile-compressive behaviour of the early stages of a *Volmer-Weber* growth. Taken from [50].

techniques and, in general, is typical of metals with low superficial mobility of the adatoms (for further details the reader is referred to section 1.3.2). Moreover, the *Volmer-Weber* mechanism is associated to a well defined stress evolution as the thickness increases that, as it can be seen in figure 4.2, follows a compressive-tensile-compressive trend [50]. The tensile peak is related to the coalescence of the islands ("zipping") and the subsequent formation of grain boundaries, while the overall compressive stress is a consequence of the strain created by the interaction between the film and the substrate during the island growth [50]. Following this interpretation, the tensile stress observed in the thinnest samples deposited with no ion assistance, could be a consequence of the coalescence of the islands. However, it does not mean that, under these deposition conditions, the threshold thickness for the islands merging is approximately 50 nm. Indeed, to identify the position of the tensile peak several measurements, even at lower thickness, are needed. Nevertheless, a coalescence thickness of a few tens of nanometers could be reasonable. For example, the aluminium and silver films deposited by by Floro et al. in [50] using electron beam evaporation, featured tensile peaks at $\sim$ 10 and $\sim$ 25 nm, respectively. In the same paper, the coalescence thickness of titanium was reported to be $\sim$ 2.5 nm, but the value may change significantly depending on the deposition conditions. In fact, Dellasega et al. in [90] for a fcc titanium films, deposited by High Power Impulse Magnetron Sputtering (HiPIMS) without applied bias, registered, using the same setup of my work, the tensile peak of titanium at $\sim$ 75 nm. Thus, the extremely

low value of ~ 4.8 nm, recorded using high-pressure RHEED by Pryds et al. in [91] on TiN films obtained by ultra-high-vacuum PLD deposition on a single crystal of MgO heated at 700°C, can not be used as reference due to the different deposition conditions used in this work. Indeed, a very high substrate temperature increases the surface mobility of the deposited species favouring the continuity of the film.
If this growth mechanism for the PLD TiN will be confirmed by further analysis, it is highly probable that also the films deposited with the ion assistance feature a *Volmer-Weber* behaviour. However, the stress featured by the sample 45 nm thick is highly compressive. In this case, it can be supposed that the islands coalescence, hence the tensile peak, is featured at lower thickness. Indeed, it could be that the additional energy from the ions may enhance the surface mobility of the deposited species favouring the merging of the islands. On the other hand, the very high compressive stress featured by the thinnest IBAD film could be a consequence of the effects of the ion bombardment, that may relax as the thickness increases.
In conclusion, the evidences obtained with this exploratory study confirm the overall compressive stress in the film reported in literature. Moreover, the tensile residual stress featured by one of the thinnest films deposited without ion assistance may indicate a possible *Volmer-Weber* growth mechanism that, indeed, was the expected one, due to the low mobility of the deposited species. Nevertheless, it is evident that further analysis on the residual stress in the TiN films are needed, in particular, it could be interesting to decrease further the thickness and correlate the results with an analysis of the crystallinity (e.g. XRD measurements).

4.2 Electrical measurements

In section 1.3.6 I presented a detailed discussion on the effects of the thickness reduction on the electrical and optical properties in TiN films deposited with many different techniques. It was highlighted that, to obtain continuous TiN films with thickness down to ~ 10 nm, the deposition could become extremely challenging. In particular, it is often required the use of highly crystalline substrates that feature a lattice structure extremely similar to the titanium nitride, e.g. MgO. Moreover, to assure the continuity of the films, and a good regularity in the structure, a high surface mobility of the deposited species is needed, that can be obtained, for example, heating the substrate. Due to these strong limitations, the possibility to deposit ultra-thin films of TiN using a room temperature PLD technique is debatable.
In the next paragraph, the results on an exploratory study of the effect of the reduction of the thickness on the electrical properties of titanium nitride films are presented. The substrates analysed are the same used for the internal stress analysis, thus with a thickness between ~ 50 and ~ 350 nm. Due to the thickness considered, it is quite unlikely to observe strong modifications in the electrical properties. Indeed, as said in section 1.3.6, the strongest effects are expected to appear as the thickness becomes comparable to the mean free path of the electrons, arguably similar to the dimension of the grains, probably few nanometres [1].

4.2.1 Results

For the electrical measurements, the setup is the same used in the previous analysis, the four-point probe described in section 2.4. The quantities analysed are, as usual, the resistivity and the carrier density and mobility. However, it was not possible to have reliable data for the last two quantities for all the samples deposited without ion assistance. The impossibility to complete Hall measurements could be an indication of the films characteristic. Indeed, according to the electrical and EDXS measurements presented in section 3.1.3 and 3.1.1, it could be a consequence of the higher stoichiometry and the lower content of oxygen in the IBAD films, or can be caused by an improvement of the electron mobility in the films, maybe related to a more compact and regular structure.
In figure 4.3 the data of the resistivity of the samples as a function of thick-

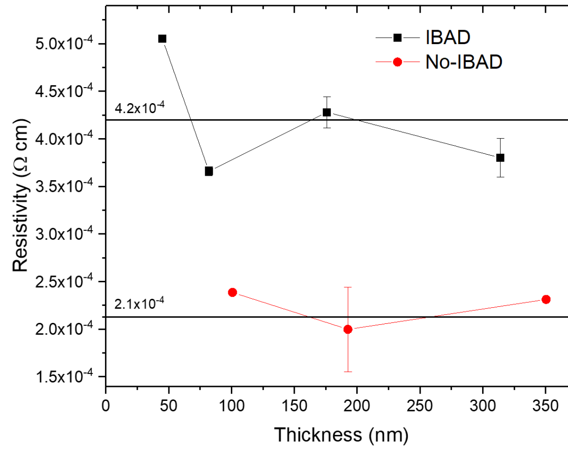

Fig. 4.3: Resistivity as a function of the thickness of the films. In black the samples deposited with ion assistance, in red those deposited without assisting ions. The two black lines indicate the respective values of the resistivity measured in the samples analysed in 3.1 and deposited under the same conditions.

ness are presented. In the graph, the values of the resistivity featured by the samples analysed in section 3.1.3 and deposited in the same conditions are also indicated, as it can be seen, they are consistent. First of all, it is evident that the 55 nm film without ion assistance could not be measured. The reasons why the resistivity could not be measured in this samples are probably very similar to those that may explain the absence of the data on the carriers, so, for example, it could be due to a very disordered structure. However, a further possible explanation can be the growth mechanism. Indeed, the samples deposited with no ion assistance and 55 nm thick, are the only two that feature an average tensile stress state, that may indicate a not complete merging of the islands. On the other hand, the three remaining samples deposited with no IBAD do not show a particular trend with respect to the thickness and, moreover, the accuracy of the measurement of the 192 nm thick sample is very low. The situation slightly changes when it comes to consider the films deposited with the ion assistance. Indeed, in this case a considerable increase of the resistivity can be observed in the 45 nm film. However, the low value of the resistivity featured by the 82 nm film do not allow to define a trend, as in the films deposited with no assisting ions. Nevertheless, the high resistivity featured by the thinnest film could be in ac-

cordance to the possible modifications in the electrical quantities highlighted in section 1.3.6. Indeed, as the thickness decreases, the surface effects start to play a major role. The unavoidable oxidation of the surface, the higher defects density of the interfaces and the interfaces itself may cause an increase of the resistivity as a consequence of the reduction of the free mean path and of the electronic density. However, as said, these effects start to be well visible only when the thickness is comparable to the mean free path of the electrons. Indeed, the data collected on the electronic density and mobility of the carriers, presented in figure 4.4b and 4.4a, as the wideness of the error bars attest, do not present a clear trend. Nevertheless, the values are comparable to those of the samples analysed in section (reported in 3.1.3 the graphs).

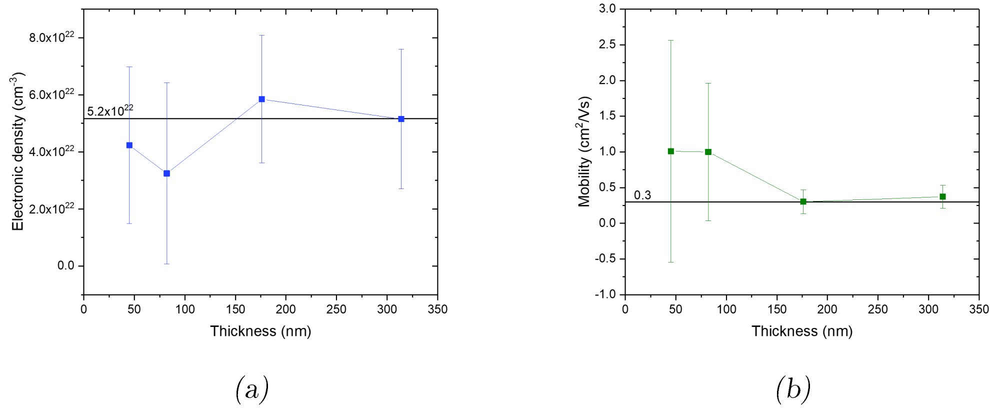

(a) *(b)*

Fig. 4.4: Electronic density *(a)* and carrier mobility *(b)* as a function of the thickness of the films deposited with ion assistance. The horizontal black lines indicate the respective values measured in the samples analysed in 3.1 and deposited under the same conditions.

In conclusion, the results from this exploratory study are far from being exhaustive, additional tests should be carried out changing the fluence, the acceleration voltage of the ions and lowering further the thickness, or exploiting other analysis techniques. Nevertheless, as first indication, it could be said that the ion assistance seems to favour the deposition of low thickness films, probably improving the overall quality of the samples, especially the electrical properties.

5. CONCLUSIONS AND PERSPECTIVES

The long term goal of this thesis is the exploitation of the tuning capability of the plasmonic frequency of TiN for technological applications, in particular in the solar energy harvesting field. For this purpose it is essential to have the ability to manage the stoichiometry of the film, while maintaining the control on the structure and the crystallinity. To achieve these goals, thin TiN films were deposited using a room temperature PLD system with nitrogen ion assistance. To assess the effectiveness of the assisting ions, several analysis were conducted, modifying both the energy of the ions and the fluence of deposition. Subsequentially, the films were subjected to three different thermal treatments, with the aim to improve the crystalline and electrical properties of the samples, and the analysis repeated to evaluate the effect of these treatments. Furthermore, by the end of the thesis, two additional exploratory studies were conducted to investigate the internal stress state and the modifications of the electrical quantities caused by the decreasing of the film thickness, down to $\sim$ 50 nm.

The PLD deposition of TiN samples were performed on thermally grown SiO_2 substrate, to reduce the thermal coefficient mismatch with the film and have the possibility to perform the electrical measurements (being silica an insulator). The deposition fluences tested were three: 1.7, 1.9 and 3.1 J/cm^2. For each fluence, three different depositions were performed: the first as reference, without ion assistance, the other two with the ion acceleration voltage set at 200 and 350 V, respectively. The thickness of the samples was set to be 500 nm, but the measurements reported values between 375 and 512 nm, in general lower for higher ion energies. The reason of this effect is not clear, it could be caused by a deflection of the incoming particles by the ion beam, or as result of a more compact film. Nevertheless, the SEM cross-section imagines showed, for all the samples, a compact structure with rather irregular columns. The effect of the ion assistance on the structure did not appear to be visible in the samples deposited at 3.1 J/cm^2, while seemed to have caused a smoothness of the columns in the films deposited at lower fluence. Despite this, the effect of the ion assistance was well visible in all the analysis conducted.

In the EDXS measurements, it was highlighted that the nitrogen concentration in the films increased with the use of the assisting ions. This increment, that resulted progressive with the energy of the ions, was more evident as the fluence was decreased. However, the exact stoichiometry of the samples was not available. Indeed, the accurateness of the EDXS measurements is not particularly high when it comes to atoms with low atomic number (as nitrogen and oxygen) and moreover, the x-ray energies associated to titanium, nitrogen and oxygen are rather close. For these reasons, a quantitative description was not possible, but the trends observed were still evident. The measured nitrogen-titanium ratio remained low with respect to the target, probably to a wider angular expansion in the plume of the nitrogen with respect to the titanium, being the first element lighter. The only films that featured values close to the target were those deposited at low fluence and high acceleration voltage. A second effect of the ion bombardment, measured thanks to the EDXS analysis, was the reduction of the oxygen concentration in the films, as the nitrogen increased. This effect could be explained assuming that the high energy of the nitrogen ions favoured the formation of $Ti - N$ bounds at the expense of oxygen, a sort of competitive process. Indeed, in general, titanium features a higher reactivity with oxygen then with nitrogen.
The Raman analysis confirmed the results from the EDXS measurements. In particular, most of the analysed spectra completely miss the band at 600 cm^{-1}, related to the nitrogen ions N^{3-}, this can be related to a very low content of nitrogen or to an absence of titanium vacancies. The only samples that featured this band were those deposited with acceleration voltage at 350 V. In particular, it was observed that the height of the band increased as the fluence was lowered, probably due to the higher nitrogen content. However, the nitrogen band featured by these films was slightly blue-shift with respect to the reference one of spectra in the literature. This shift was explained with the probable presence of an oxynitride phase in the films, arguably of the type TiO_xN_y. The presence of an oxide phase in the samples was highlighted also by the presence of small bands, in some of the spectra, associated to the spectrum of amorphous TiO_x. Moreover, in the Raman spectra of the specimen deposited at the lowest fluence and with the highest ion energy, the band at 400 cm^{-1}, related to the titanium, featured two peaks, associated to the longitudinal and transverse acustic modes of the titanium ions Ti^{4+}. In the others sample it was visible just the first one, maybe due to a less stoichiometric and regular structure.
The electrical measurements conducted revealed an electronic density coherent with the results from the EDXS measurements, thus higher in the samples deposited without ion assistance, that are particularly sub-stoichiometric. As

the energy of the ions was increased, the electronic density decreased, and in the samples deposited at 1.7 and 1.9 J/cm^2 with 350 V reached similar values to the reference one for the stoichiometric TiN of $\sim 5 \times 10^{22}$ cm^{-3}. As far as the mobility is concerned, the values measured are quite low with respect to the literature, but the ion assistance had a beneficial effect, at least at the lowest fluences. Indeed, in the samples deposited at 1.7 and 1.9 J/cm^2 the mobility increased almost linearly with the ion energy, from $\sim$ 0.15 to $\sim$ 0.3 cm/V s, with the film deposited at 1.9 J/cm^2 that reached even $\sim$ 0.38 cm/V s. The resistivity, being affected both by electronic density and mobility, generally increased with the ion assistance. This effect was particularly evident at the lowest fluence, where it doubled, going from 2.1 Ω cm, without IBAD, to 4.2 Ω cm with ion acceleration voltage at 350 V. Nevertheless, all the samples featured values even one order of magnitude higher with respect to the best found in the literature.
The measurements of the optical response reported a general red-shift of the minimum of reflectance of some tens of nanometers, as the fluence was decreased and the ion energy increased. This trend was related to the augmented nitrogen content and to the electronic density, the lower it was, the more red-shifted was the minimum of reflectance. On the other hand, the results for the slope of the reflectance edge and the values of the reflectivity at the minimum and at the long wavelength limit may be interpreted as a consequence of a lower quality of the films deposited at higher ion energy and lower fluence. This explanation can be considered in disagreement with the results of the mobility, in fact an increase in the mobility may be justified by a less defective and regular structure. Nevertheless, it could be that the defects that affect the reflectance curve and the mobility of electrons are of different typology.
From these results, it is evident that the Ion Beam Assisted Deposition can effectively tune the stoichiometry of the samples, and, according to the reflectance measurements, modify the optical response of the films. Moreover, the results showed also a decrease in the oxygen concentration and an improvement of the mobility. On the other hand, the effect on the structure and on the lattice is less clear, to have a deeper understanding, different analysis techniques are probably needed, e.g. X-Rays Diffraction (XRD). Nevertheless, it can be said, that the most encouraging results, especially on the stoichiometry and the on the electronic density and mobility, were observed in the films deposited at 1.7 and 1.9 J/cm^2, probably because a lower fluence guarantees a higher effectiveness of the ion assistance.

The thermal treatments performed were three, two that lasted one hour, at 700 and 865°C, and one 15 minutes, at 865°C. After the annealing, the same

analysis were repeated on all the films, to understand the possible effects depending on the temperature, the duration, but also the fluence of deposition and the energy of the ions. The overall effect of the thermal treatments is quite difficult to understand, indeed the reaction to the thermal stimulus was not always progressive with temperature and time, or homogeneous for all the samples. Moreover, the electronic density and mobility were not available due to the very low reliability of the measurements, probably due to an extensive superficial oxidation.
In general, it can be said that all the thermal treatments caused an increment of the oxygen concentration in the films, often together with an increase of the the nitrogen-titanium ratio of difficult explanation. In particular, this last enhancement was well visible for the samples deposited at 1.7 J/cm^2 and heated at 700°C. Among these films, the one deposited with ion acceleration voltage of 350 V reported a nitrogen-titanium ratio slightly higher then the one measured for the target. The resistivity measurements highlighted an overall decrease of the resistivity, with the samples deposited at 1.7 J/cm^2 and annealed at 700°C that showed the most constant and predictable lowering. However, the lowest values of the resistivity remained those measured in the samples deposited at 3.1 J/cm^2, probably due to a higher electronic density, and, in general, the decrease of the resistivity was limited to a few tens of percentage points, or even less. Not enough to consider the thermal treatments successful, at least from the resistivity point of view. Furthermore, since the low reliability of the measurements on carrier density and mobility could have been caused by an extensive superficial oxidation, the confidence of the resistivity data can be debatable. Nevertheless, for a complete comparison and a better understanding of the resistivity trend, the data on mobility and electronic density are needed.
The Raman spectra of the annealed samples did not show particular differences with respect to the as-deposited spectra. The only small modifications that could be noted was an increment of the small bands associated to the TiO_x and in the band at $\sim$ 600 cm^{-1}, probably related to the increment in the oxygen content or in the nitrogen-titanium ratio.
The optical analysis reported a generalized red-shift of the minimum of reflectance. This shift can be explained by a reduction in the electronic density, probably due to the higher nitrogen-titanium ratio. The results of the slope of the reflectance edge and those of the reflectance values at the minimum and at long wavelength may be interpreted as proof of an overall increase in the quality of the films, in particular for the samples treated at high temperature. Probably some healing process was activated by the heat.
In conclusion, the effect of the thermal treatments is different depending on the temperature and on the setup of deposition considered. Moreover, it

seems that the annealing treatment that induced more improvement depends on which measurement technique is considered. Indeed, if the discussion is focused on $N - Ti$ stoichiometry and electrical resistivity, the most effective is probably the most gentle one, at 700°C, especially if conducted on the samples deposited at 1.7 J/cm^2. On the other hand, if optical results are considered, the best treatments appeared to be those at 865°C. Nevertheless, further analysis, especially on the crystalline structure by XRD, are needed.

The exploratory study carried out on the thickness dependence of residual stress and electrical properties produced encouraging results. Indeed, even if the interpretation must be very cautious due to the low number of samples analysed, the results seemed to agree with a possible *Volmer-Weber* growth mechanism for the TiN films deposited using room temperature PLD. Furthermore, following this interpretation, it could be hypothesized that the ion assistance may favour the coalescence of islands at earlier deposition stages and a more compact and regular structure. These suppositions seemed to be confirmed by the electrical measurements, as it was not possible to measure the resistivity in the 45 nm films deposited without ion assistance, probably due to the absence of a structural order or continuity in the specimens. Moreover, in the samples deposited without assisting ions, the mobility and the density of carriers could not be measured, while they were available in those deposited with the IBAD technique. Nevertheless, neither in resistivity values nor in those of electronic density and mobility, it was possible to define a trend. Just the 55 nm films deposited with ion assistance featured a high resistivity value that could be a consequence of the reduced thickness, since the relative importance of interfaces, related defects and superficial oxidation in the electronic scattering increases.

To sum up, the best results obtained during this thesis work are:

- The possibility to tune with the ion energy the concentration of nitrogen in the films. This allows to modify the stoichiometry of the sample and adjust the plasmonic response. The effects are much more evident in the specimen deposited at low fluences.

- The ion assistance mitigates the problem of the high oxygen content encountered in previous work conducted in the research group [1]. In fact, as the ion energy is increased the oxygen concentration is decreased, even reaching a value comparable with the concentration measured in the target used for the deposition. Again this effect is more consistent for the deposition carried out at 1.7 J/cm^2.

- The bombardment with ions seems to favour electron mobility, that, however, remains low. On the other hand, it decreases the quality of the optical response. Probably a compromise will be necessary between optical and electrical properties.

- The thermal treatments performed had a direct effect on films properties. Lower temperature (i.e. 700°C) is to be chosen if lower resistivity must be favoured, while, higher temperature is needed if the quality of the films, from the optical analysis point of view, must be improved. Nevertheless, the decrease of the resistivity is moderate, within $\sim 20\%$.

- The bombardment with ions might have some effect even on the internal stress and the electrical quantities of the films as a function of the thickness. From a very qualitative and hypothetical point of view, it appeared that TiN films deposited without assisting ions followed a *Volmer-Weber* growth mechanism. While, the ion assistance might favour islands coalescence, probably enhancing the mobility of the deposited species. Moreover, from the electrical measurements, it could be inferred that the use of the IBAD technique may favour better electrical behaviour even at lower thickness.

Nevertheless, all the factors that influence the characteristics of the films are far form being understood. Moreover, many crucial properties could not be assessed during this thesis work. First of all, the crystallinity and grain dimension of the samples, due to the absence of the XRD analysis. These information could have been particularly helpful, since they largely influence both electrical properties and optical response. Moreover, more reliable measurements on the stoichiometry and the electrical quantities are needed to give more exhaustive explanation and interpretation to the trends observed. To improve the knowledge of the optical and plasmonics behaviour, ellipsometry measurements, that can provide the value of the plasma frequency and of the component of the complex refractive index of the material, are an essential step. As far as the stress measurements are concerned, further analysis at a lower thickness and a wider statistics are needed. In addition, it might be interesting to observe also the effect of different fluence and ion energy, that may give additional interpretation of the phenomena observed. Finally, it could be worthwhile to analyse also other properties as a function of the thickness, to provide a more complete understanding of the behaviour of the films.

Considering long therm perspectives, some interesting studied could be:

- Deeply investigating the correlations between electric and optical characteristics and the plasmonic response of the films.
- Finely tuning the plasmonic response according to the requirements of specific applications.
- Further reducing the thickness of the films down to few nanometers to exploit quantum phenomena. It is highly probable that, to exploit this possibility, it could be necessary to heat the substrate.
- Studying the optical and the plasmonic response of TiN in contact with different dielectric media. Indeed, the properties of SSP and LSPP depend on the medium in which the plasmonic material is immersed.
- Exploiting the properties and the possible architectures of nanostructured films of TiN to widen the plasmonic and optical response.

APPENDIX

A. FUNDAMENTALS OF PLASMONICS

The interaction between metals and electromagnetic waves, thanks to the high density of electrons that such materials feature, can be analysed in a satisfactory way using classical physics. The optical properties of metals are quite different from those shown by dielectric materials mainly due to the high mobility of the conduction electrons with respect to the valence ones. However, the response to an electromagnetic stimulus strongly depends on the frequency and the ability of the electrons to catch up with the oscillatory force exercised by the the electromagnetic field. The dependence on the frequency causes clear and sharp differences in the behaviour of the metals under this sort of stimuli. One of the most important feature is the presence of a specific frequency, called *plasma frequency* (ω_p), that acts as a threshold value between a spectral region characterized by high reflectivity and a region where the metal is basically transparent to the radiation. This marked variation is well visible in the alkali metals, while it is more blurry in the noble metals. In general, for metals such as gold or copper, this characteristic frequency is in the ultraviolet range.
The different behaviours with respect to the frequency of the incident radiation will be briefly discussed in the following paragraph through the analysis of the function that determines the response of the material to light: the *dielectric function* $\epsilon(\omega)$.

The discussion about the interaction between metals and light may start with Maxwell's equations in the domain of macroscopic electromagnetism:

$$\bigtriangledown \cdot \mathbf{D} = \rho_{ext} \tag{A.1}$$

$$\bigtriangledown \cdot \mathbf{B} = 0 \tag{A.2}$$

$$\bigtriangledown \times \mathbf{E} = -\frac{\partial \mathbf{B}}{\partial t} \tag{A.3}$$

$$\bigtriangledown \times \boldsymbol{H} = \boldsymbol{J_{ext}} + \frac{\partial \boldsymbol{D}}{\partial t} \tag{A.4}$$

Another important relationship, that will be useful in the following, correlates the displacement vector $\boldsymbol{D}$ with the electric field $\boldsymbol{E}$ through the dielectric

constant ϵ_0 and the macroscopic polarization $\boldsymbol{P}$:

$$\mathbf{D} = \epsilon_0 \mathbf{E} + \mathbf{P} \tag{A.5}$$

Limiting the analysis to linear and isotropic media the previous equation becomes:

$$\mathbf{D} = \epsilon_0 \epsilon \mathbf{E} \tag{A.6}$$

where ϵ is the dielectric function or relative permittivity. It assumes different values depending on the material (in vacuum $\epsilon = 1$) and in general it is a complex function of the type $\epsilon(\omega) = \epsilon_1(\omega) + i\epsilon_2(\omega)$.
It is well known that combining the two curl equation in the approximation of $\boldsymbol{J} = 0$ and $\rho = 0$, it is possible to obtain a wave equation that describes the propagation of an electromagnetic radiation:

$$\bigtriangledown \times \bigtriangledown \times \boldsymbol{E} = -\mu_0 \frac{\partial^2 \boldsymbol{D}}{\partial t^2} \tag{A.7}$$

Moreover, if we assume that the electromagnetic wave is composed by a linear combination of single plane waves of the type $\boldsymbol{E} = E_0 e^{-i(\boldsymbol{k}\cdot\boldsymbol{r}-\omega t)}$, where $\boldsymbol{k}$ is the wave vector and ω the frequency of the plane wave. Inserting it into eq.A.8 we obtain:

$$\boldsymbol{k}(\boldsymbol{k}\cdot\boldsymbol{E}) - k^2 E = -\epsilon(\omega)\frac{\omega^2}{c^2}\boldsymbol{E} \tag{A.8}$$

If we assume the wave to be transverse, thus if $\boldsymbol{k}\cdot\boldsymbol{E} = 0$ holds, we obtain the generic dispersion relation:

$$k^2 = \frac{\omega^2}{c^2}\epsilon(\omega) \tag{A.9}$$

On the other side, longitudinal waves imply that $\epsilon(\omega) = 0$.
From the dielectric function it is straightforward to derive the refractive index of the material: $\tilde{n} = \sqrt{\epsilon(\omega)}$, which is a complex function too, that can be written in the form $\tilde{n} = n + i\kappa$. The two components of the refractive index can be related to the components of the dielectric function as follows:

$$\epsilon_1 = n^2 - \kappa^2 \tag{A.10}$$

$$\epsilon_2 = 2n\kappa \tag{A.11}$$

In particular, κ is called *extinction coefficient* and it is related to the absorption coefficient α of Beer's law, that describes the exponential attenuation of a travelling beam through a medium via $I(\alpha) = I_0 e^{-\alpha x}$, with

$$\alpha(\omega) = \frac{2\kappa(\omega)\omega}{c}. \tag{A.12}$$

On the other side, in the limit of $|\epsilon_1| \gg |\epsilon_2|$, n determines the lowering of the phase velocity of the propagating wave inside the material due to the polarization.
When an electromagnetic wave encounters an interface between two different materials with different index of refraction, it can be reflected back, transmitted or absorbed. Considering just the first phenomenon, its probability can be described by the coefficient of reflectivity R that, when the incident light is normal to the interface, is:

$$R = \frac{(n-1)^2 + \kappa}{(n+1)^2 + \kappa} \tag{A.13}$$

This equation implies that, whenever $n = 0$, $R = 1$, hence, when $\tilde{n}$ is completely imaginary, the light is completely refracted back.

A.1 The dielectric function of the Free Electron Gas

If we limit the description of the optical behaviour of metals to the visible-UV range, to treat their optical response it is possible to use the *Free Electron Gas* model. The basic idea is to consider the metals as they were composed by harmonic oscillators with no restoration force, so, basically, as if the electrons were free particles with numerical density n that oscillate against a lattice background of positive charges, the nuclei. This model, proposed by Drude, goes under the name of *plasma model* and works using two strong approximations: *the independent electron* approximation and the *free electron approximation.* It means that the electrostatic repulsion between electrons is considered null and all the other interactions, as those with the lattice, are taken into account varying the value of the effective mass ($m_e^\star$). The only interactions that will be explicitly considered are the electron collisions with defect and phonons: these events are taken into account statistically through the average collision frequency Γ_D, that plays the role of the damping term in the final equation. Its value is the reciprocal of the average time between collisions: the relaxation time τ (usually in the order of $\sim 10^{-14}$ s). All this considered, it is possible to write the kinetic expression of one electron subjected to the excitation of an electric field:

$$m_e\ddot{\mathbf{x}} + m_e\Gamma_D\dot{\mathbf{x}} = -e\mathbf{E} \tag{A.14}$$

Where $\boldsymbol{x}$ is the displacement from the equilibrium position of an electron. For the electric field it is possible to assume a harmonic dependence with

respect to the time according to the *long wavelength approximation (i.e. dipole approximation)*: $\mathbf{E}(t) = \mathbf{E}_0 e^{-i\omega t}$ and, thus, a particular solution of the equation can be written in the form: $\mathbf{x}(t) = \mathbf{x}_0 e^{-i\omega t}$, with $\mathbf{x}_0$ complex amplitude that takes into account any phase shifts. Solving the eq.A.14 yields to:

$$\mathbf{x}(t) = \frac{e}{m_e(\omega^2 + i\Gamma_D\omega)}\mathbf{E}(t) \tag{A.15}$$

The macroscopic polarization $\mathbf{P}$ can be calculated starting from the displacement $\mathbf{x}$ of each electron of charge $-e$. Thus, since the numerical density of the electrons is n, $\mathbf{P} = -ne\mathbf{x}$ and, using eq.A.15:

$$\mathbf{P} = -\frac{ne^2}{m_e(\omega^2 + i\Gamma_D\omega)}\mathbf{E} \tag{A.16}$$

Inserting this equation in eq.A.5:

$$\mathbf{D} = \epsilon_0(1 - \frac{\omega_p^2}{\omega^2 + i\Gamma_D\omega})\mathbf{E} \tag{A.17}$$

where $\omega_p = \sqrt{\frac{ne^2}{\epsilon_0 m_e}}$ is called *plasma frequency* of the free electron gas. Recalling eq.A.6:

$$\epsilon(\omega) = 1 - \frac{\omega_p^2}{\omega^2 + i\Gamma_D\omega} \tag{A.18}$$

$\epsilon(\omega)$ is a complex function and can be divided into one real and one complex term:

$$\epsilon_1(\omega) = 1 - \frac{\omega_p^2\tau^2}{1 + \omega^2\tau^2} \tag{A.19}$$

$$\epsilon_2(\omega) = \frac{\omega_p^2\tau}{\omega(1 + \omega^2\tau^{2)}} \tag{A.20}$$

Since already in the visible we can consider $\omega\tau \gg 1$, the damping is negligible, and the dielectric constant, now predominantly real, can be approximated to:

$$\epsilon(\omega) = 1 - \frac{\omega_p^2}{\omega^2} \tag{A.21}$$

It is evident how for $\omega < \omega_p$ ϵ is lower than 0, this causes $\tilde{n}$ to be completely imaginary and, recalling eq.A.13, R to be 1: the light is completely reflected back. The situation drastically changes above ω_p, where $\tilde{n}$ becomes basically equal to n and the metals transparent to the radiation. It is possible to see that, as soon as $\omega = \omega_p$, the dielectric function goes to zero. This happens

to be the exact condition of existence of longitudinal waves, indeed $\epsilon = 0$ means $\boldsymbol{k} = 0$ and consequently $\lambda = 0$. From a phenomenological point of view, it is observed as a collective electronic mode in which all the electrons move together with the same phase. In other word, a simultaneous oscillator displacement with frequency ω_p of the electrons arises in a bulk metal. The quanta of energy of such collective charge oscillation are called *plasmon*.

A.2 Lorentz model

The simple *plasma model*, however, it is not enough to describe accurately the observations. To improve the correspondence with the real situation, we must take into account the electronic transitions that happen within two bands (interband transitions), usually between valence and conduction bands, in a real material. In particular we are interested in those transitions close to ω_p that can influence the optical response in this range of frequency. The basic scheme which can take account of them is the Lorentz model and, differently from Drude assumptions, it takes into account a linear restoring force ($k\mathbf{x}$) acting on the electrons. Thus, the resulting model will be represented by a damped oscillator, with a resonant frequency that coincides with the relative interband transition. The kinetic equation for the displacement from the equilibrium position as a function of the time, under the stimulus of en electric field, can be written as:

$$m_e\ddot{\mathbf{x}}(t) + \gamma\dot{\mathbf{x}}(t) + k\mathbf{x} = e\mathbf{E}_0 e^{-i\omega t} \tag{A.22}$$

Where, γ is the damping coefficient related to the interband transitions. With the same procedure as in the Drude model, we can derive the dielectric function related to the Lorentz contribution. Usually there are more possible transitions, each one with a specific energy, to account of all of them the Lorentz model can be written as a sum of different oscillators with a characteristic resonant frequency (corresponding to the specific energy of the transition they are referred to) and a multiplicative coefficient, the oscillator strength f_i, that takes into account the relative contribution of the overall dielectric function. Summing the Drude and the Lorentz contribution to the dielectric function together:

$$\epsilon(\omega) = \tilde{n}^2 = \epsilon_\infty - \frac{\omega_p}{\omega^2 - i\Gamma_D\omega} + \sum_{i=1}^{N} a_i \frac{f_i\omega_{0i}^2}{\omega_{0i}^2 - \omega^2 - i\gamma\omega} \tag{A.23}$$

where $\omega_{0i}^2 = k/m_e$ is the resonant frequency of the $i-$oscillator, thus $\hbar\omega_{0i}$ the energy of the $i-$interband transition. Moreover, it is possible to take

into account the residual polarization in the high frequency limit adding a constant term ϵ_∞.
When the interband transition are close in energy to the plasma frequency, they can modify strongly the optical response of the material in this range of frequency modifying the position of ω_p. This phenomenon can be clearly seen in gold (fig.A.1), where the interband transition between $3d$ and $4s$ orbitals is at ~ 2.1 eV, in the visible, this results in a sharp decrease of the reflectivity well before the plasma frequency with the consequence to give to gold the characteristic yellow colour. Indeed, the shorter wavelengths of the visible spectra are reflected back much more than those in the green-blue region. This scheme can describe the colour of many other $3d$ metals, such as copper.
The introduction of the interband transition into the model causes a shift of the plasmonic frequency that now assumes a value that in principle should be the observed one. To distinguish the two plasma frequency characterizing a system, the one arising from the Drude model and the experimental one, they have been called in two different ways. The first *Unscreened plasma frequency* (ω_{pu}) since it is not yet influenced by the interband transitions, indeed it can be seen as an evaluation of the ideal metallic character of the materials. The second *screened plasma frequency* (ω_{ps}) as it considers the Lorentz model too and accounts for the dielectric behaviour of the material. IN particular, the *screened plasma frequency* can be evaluated using the following equation:

$$\omega_{ps} = \sqrt{\frac{4\pi n e^2}{\epsilon_\infty m_e}} \tag{A.24}$$

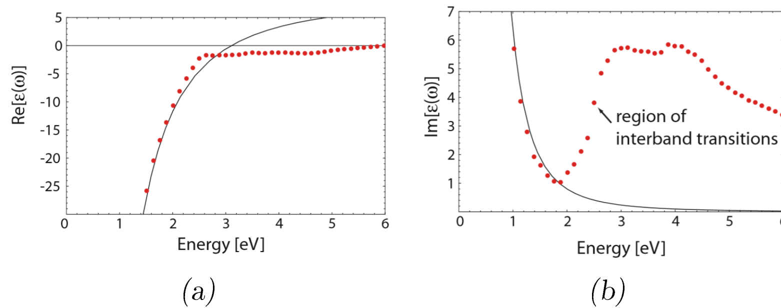

(a) (b)

Fig. A.1: Real (a) and imaginary (b) part of the dielectric function of gold. The solid black lines are the fitting of the Drude model, the dotted red lines the experimental measurements that take into account the interband transition too, (c) taken from [92].

A.3 Surface plasmon polariton

If we now focus our attention to the interface between a dielectric material and a metal, we can observe the appearance of surface-charge-density oscillations strongly evanescently confined along the vertical direction, hence bounded to the surface, and coupled with a propagating electromagnetic wave caused by the charge displacement. These modes go under the name of *Surface Plasmon Polariton (SPP)* and can be observed under specific conditions here briefly explained. To find this conditions we are going to set the interface at the plane $z = 0$ (fig.A.2) and look for homogeneous solutions of the Maxwell's wave equation:

$$\bigtriangledown \times \bigtriangledown \times \mathbf{E}(\mathbf{r}, \omega) - \frac{\omega^2}{c^2}\epsilon^2(\mathbf{r}, \omega)\mathbf{E}(\mathbf{r}, \omega) = 0 \tag{A.25}$$

since above and below the interface there are two different materials, we may define $\epsilon(\mathbf{r}, \omega) = \epsilon_1(\omega)$ in the region with $z < 0$, and $\epsilon(\mathbf{r}, \omega) = \epsilon_2(\omega)$ in the region with $z > 0$.

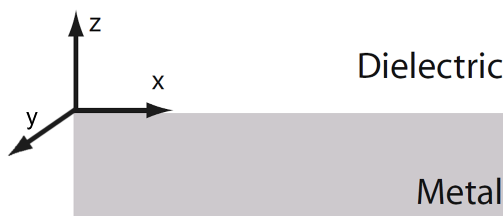

Fig. A.2: Scheme of metal-dielectric interface. Taken from [92].

It can be demonstrated that surface plasmon polariton can not sustain *s-polarized* waves, for this reason we will consider *p-polarized* waves only, namely those with no components of the electric field along y. In the half spaces $j = 1$ and $j = 2$ we can write:

$$\boldsymbol{E}_i = \begin{pmatrix} E_{j,x} \\ 0 \\ E_{j,z} \end{pmatrix} e^{ik_x x - i\omega t} e^{ik_{j,z} z}. \tag{A.26}$$

To proceed we can exploit the fact that the component parallel to the interface of the wave vector is conserved and that the displacement field ($\boldsymbol{D}$) in

the two half spaces are source free, thus $\bigtriangledown \cdot \boldsymbol{D} = 0$:

$$k_x^2 + k_{j,z}^2 = \epsilon_j k^2 \tag{A.27}$$

$$k_x E_{j,x} + k_{j,z} E_{j,z} = 0 \tag{A.28}$$

hence eq.A.26 can be rewritten as:

$$\boldsymbol{E}_i = \begin{pmatrix} 1 \\ 0 \\ -k_x/E_{j,z} \end{pmatrix} e^{ik_x x - i\omega t} e^{ik_{j,z} z}. \tag{A.29}$$

We can now set the boundaries conditions by requiring the continuity at the interface of the parallel component of $\boldsymbol{E}$ and the perpendicular component of $\boldsymbol{D}$:

$$E_{1,x} - E_{2,x} = 0 \tag{A.30}$$

$$\epsilon_1 E_{1,z} - \epsilon_2 E_{2,z} = 0. \tag{A.31}$$

Conditions A.28, A.30 and A.31 can be used to form an homogeneous system of four equations, whose solutions can be found imposing the respective determinant equal to zero. This happens for $k_x = 0$, that clearly does not describe a physical solution, and for

$$\epsilon_1 k_{2,z} - \epsilon_2 k_{1,z} = 0 \tag{A.32}$$

that, in combination with eq.A.27, leads to the following dispersion relation

$$k_x^2 = \beta_j^2 = \frac{\epsilon_1 \epsilon_2}{\epsilon_1 + \epsilon_2} \frac{\omega^2}{c^2} \tag{A.33}$$

for the parallel component of the wave and

$$k_{j,z}^2 = \frac{\epsilon_j}{\epsilon_1 + \epsilon_2} \frac{\omega^2}{c^2} \tag{A.34}$$

for the normal component. We can assume the imaginary component of the complex dielectric function to be small with respect to the real one, this approximation is justified because we are considering wave frequency close to ω_p. Since the electromagnetic wave is confined at the interface, we need $k_{j,z}$ to be imaginary, requiring that $\epsilon_1 + \epsilon_2 < 0$, on the other hand, to have propagation along x we need eq.A.33 to be positive. However, we just stated that the quantity at the numerator is negative, thus the conditions to fulfil both the requirements are:

$$\epsilon_1 + \epsilon_2 < 0 \tag{A.35}$$

$$\epsilon_1 \cdot \epsilon_2 < 0 \tag{A.36}$$

These conditions are necessary to observe SPP excitation. Since they require $\epsilon_1 < 0$, they can be fulfilled only if material 1 is a metal and materials 2 a dielectric. For this reason, we call $\epsilon_1 = \epsilon_m$ and $\epsilon_2 = \epsilon_d$.
It is possible to define the characteristic frequency of the SPP mode as the frequency obtained imposing the free electron function $\epsilon_m = 1 - \frac{\omega_p^2}{\omega^2}$ equal to $-\epsilon_d$:

$$\omega_{sp} = \frac{\omega_p}{\sqrt{1+\epsilon_d}} \tag{A.37}$$

In fig.A.3 the dispersion relation with negligible damping observed at the interface between a Drude metal and air or silica is presented: the solid lines represent the real part of the wave vector, while the broken lines the imaginary component. In the upper left corner it is possible to see the dispersion relation of the radiation into the metal in the transparency regime ($\omega > \omega_p$): $\omega^2 - \omega_p^2 = c^2k^2$. Below it there is a prohibited gap, where only purely imaginary wave vectors exist, in this region the propagation is not allowed. Finally, the last region is the bounded one, where surface plasmon polariton propagation is permitted. In this region, as the wave vector goes to infinity and, consequently, the wave length $\lambda_{sp} \to 0$, while the frequency asymptotically reaches the characteristic surface plasmon polariton frequency. In the opposite direction, the wave vector gets closer to the linear dispersion relation in

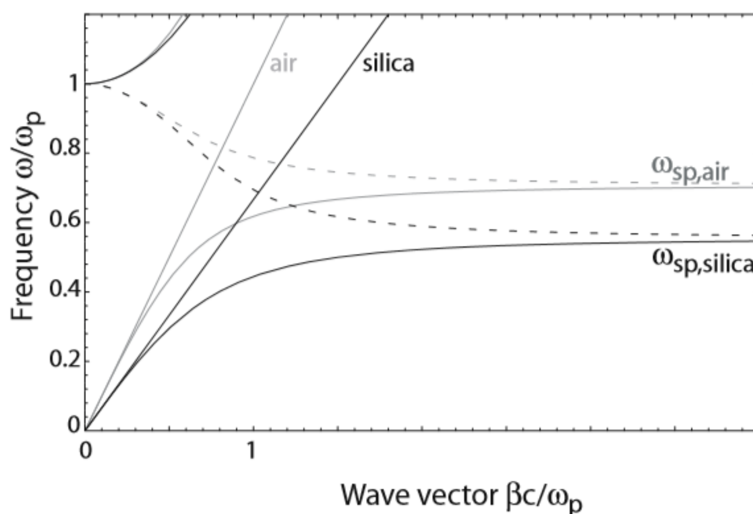

Fig. A.3: Dispersion relation of surface plasmon polariton at the interface with a Drude metal and air (grey) and silica (black). The damping are considered negligible as in an ideal model. Taken from [92].

the dielectric material with $\beta = \dfrac{\omega}{c}\sqrt{\epsilon_d}$.
As said, in the limit of negligible damping, thus with $Im[\epsilon_m(\omega)] = 0$, the wave vector goes to infinity approaching the characteristic frequency, meaning that $v_g \rightarrow 0$, this particular condition gives to the SPP mode an electrostatic behaviour. On the other hand, along the perpendicular direction, the mode is bounded, with an exponential decay length $|\hat{z}| = 1/k_z$ in the two media. In reality, the free electron model is not completely valid: the interband damping must be considered. This means that β becomes complex and the travelling surface plasmon polariton are attenuated. Indeed, it is possible to define the propagation length $L_x = (2Im[\beta])^{-1}$ that, in the visible range, it is typically of the order of some tens of micrometers. In figure A.4 it is shown how, since the damping is not negligible, the wave vector has finite maximum at ω_{sp} and the wavelength has a lower bound at $\lambda_{sp} = 2\pi/Re[\beta]$. At the same time, along the perpendicular direction, there is a limitation to the confinement since now $k_z = \sqrt{\beta^2 - \epsilon_d \dfrac{\omega^2}{c^2}}$. This allows to have propagation even in the gap region between ω_p and ω_{sp}.
Surface plasmon polaritons allow the confinement of light below the diffraction limit, indeed, since the electromagnetic field is coupled with electronic

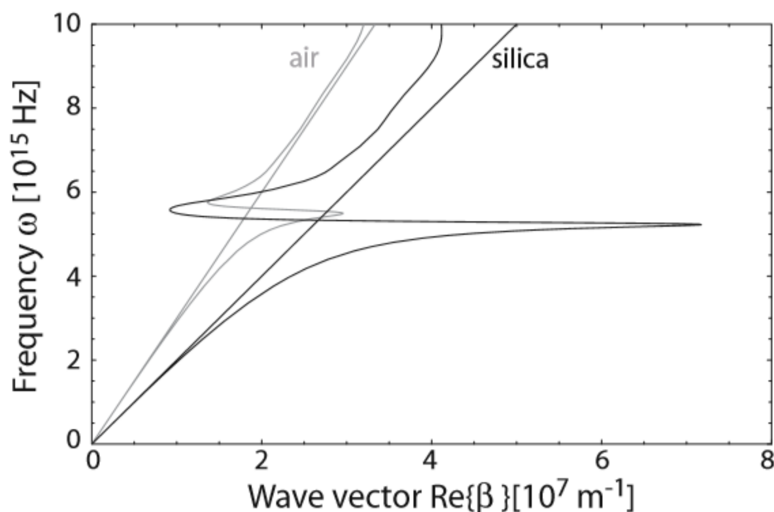

Fig. A.4: Dispersion relation of surface plasmon polariton at the interface with a Drude metal and air (grey) and silica (black). In this case the damping are not considered negligible and, indeed, the wave vector has a finite value and the propagation is allowed in the gap zone too. Taken from [92].

oscillations, we can have a propagating wave with a characteristic frequency equal to ω_{sp} that, for instance, belongs the infrared, but at the same time a wave length typical of the x-ray. Moreover, ω_{sp} can be tuned, indeed, since in the expression for the surface plasmon frequency enters ϵ_d, the dielectric material can be changed to vary ω_{sp}. However, the excitation of these modes is particularly difficult, looking at figure A.4, it is possible to notice that there is no crossing point between the dispersion relation in the dielectric and in the interface. Hence, more sophisticated methods, such as Bragg's gratings, are needed to match the wave vectors of the light travelling in the dielectric to allow the excitation of the SPP mode.

A.4 Localized surface plasmon

If we now move our attention to the electronic collective modes that arise in sub-wavelength metallic nanoparticles, we can observe the formation of non propagating oscillation of the conduction electrons. This excitation takes the name of *Localized Surface Plasmon (LSP)* and causes an amplification of the electromagnetic field, both in the vicinity and inside the particle. This effect is possible thanks to the curvature of the surface that, acting on the driven electrons, favours an effective restoring force that cause the establishment of resonance. A second major effect of the curvature of the particles is the relaxation of the strict coupling conditions needed for the SPP modes, indeed, since the electromagnetic wave impacts on a non-flat surface, there is always a component of $\boldsymbol{k}$ that matches with the one required for the excitation of the LSP.
As anticipated the dimension of the particles needs to be much less than the wavelength of the incident radiation ($d \ll \lambda$), in order to use the quasi-static approximation. This approximation assures that the electromagnetic field can be considered constant over the entire volume of the particles, in this way the spatial variation of the field can be neglected. To simplify further the discussion we can assume a homogeneous and isotropic spherical particle with radius a immersed in a isotropic and non absorbing medium. The dielectric function of the sphere is $\epsilon(\omega)$, while the one of the external medium is assumed constant with respect to ω and equal to ϵ_m. Using an electrostatic approach, we are interested in the solution of the Laplace problem ($\bigtriangledown^2\phi = 0$), from which it is possible to calculate the electric field. By solving the problem with a uniform electric field of value E_0, it can be shown that the sphere can be schematized as an ideal dipole, hence the dipole moment of the particle

is linear with respect to the field and equal to $\boldsymbol{p} = \epsilon_0 \epsilon_m \alpha \boldsymbol{E}_0$, where α is the polarizability of a sphere and writes:

$$\alpha = 4\pi a^3 \frac{\epsilon - \epsilon_m}{\epsilon + 2\epsilon_m} \tag{A.38}$$

This quantity is of paramount important in the discussion of the localized surface plasmon, indeed, it governs the overall interaction between the particles and the incident field. Taking the absolute value of the polarizability with respect to the frequency, it is possible to note that this quantity experiences a resonant enhancement whenever $|\epsilon + 2\epsilon_m|$ is a minimum. In particular, in the extreme case in which it is equal to zero, this imply that:

$$Re[\epsilon(\omega)] = -2\epsilon_m \tag{A.39}$$

This condition goes under the name of Fröhlich condition and it is associated to the *dipole surface plasmon* of the metal nanoparticle. This effect is strongly dependent on the dielectric environment and the criterion for its establishment is met when the oscillating dipole has a frequency

$$\omega_{lp} = \frac{\omega_p}{\sqrt{1 + 2\epsilon}} \tag{A.40}$$

The polarizability plays an important role in determining the entity and the intensity of absorbed and scattered light. Indeed, the corresponding cross-section of the two phenomena C_{sca} and C_{abs} can be written using the more sophisticated and complete Mie theory as:

$$C_{sca} = \frac{k^4}{6\pi}|\alpha|^2 = \frac{8\pi}{3} k^4 a^6 \left| \frac{\epsilon - \epsilon_m}{\epsilon + 2\epsilon_m} \right|^2 \tag{A.41}$$

$$C_{abs} = kIm[\alpha] = 4\pi k a^3 Im\left[\frac{\epsilon - \epsilon_m}{\epsilon + 2\epsilon_m}\right] \tag{A.42}$$

The condition for the resonant enhancement is the same in both the coefficients, however the dependence on the dimension of the nanoparticle changes. The scattering cross-section scales with a^6, thus it is favoured as the dimension increases, while, for smaller particles, the most favoured process is the absorption, that scales with a^3. The sum of the two cross-sections gives the extinction cross-section $C_{ext} = C_{abs} + C_{sca}$ and, for a sphere of volume V and dielectric function $\epsilon = \epsilon_1 + i\epsilon_2$ in the quasi-static limit is:

$$C_{ext} = 9\frac{\omega}{c}\epsilon_m^{3/2} V \frac{\epsilon_2}{[\epsilon_1 + 2\epsilon_m]^2 + \epsilon_2^2}. \tag{A.43}$$

Summing up, the overall effect is an enhancement of the local field that in turn can be associated to increased scattering or absorption phenomena.

Depending on the application, it is possible to decide whether to use bigger particles, where scattering prevails and the enhancement is widespread in the surrounding medium, or smaller ones, where absorption efficiency is higher and more feasible for local heating.

BIBLIOGRAPHY

[1] S. Garattoni. "Synthesis of titanium nitride thin films with tunable optical and electrical properties". MA thesis. Politecnico di Milano, 2019.

[2] R. Jr. Kuzel et al. "Complex XRD micristructural studies of hard coatings applied to PVD-deposited TiN films". In: *Thin Solid films* 247 (1994), pp. 64–78.

[3] Perry A.J. "A contribution to the study of Poisson's ratios and elastic constants of TiN, ZrN and HfN". In: *Thin Solid films* 193-194 (1990), pp. 463–471.

[4] P. Patsalas, N. Kalfagiannis, and S. Kassavetis. "Optical properties and plasmonic performance of titanium nitride". In: *Materials* 8 (2015), pp. 3128–3154.

[5] P. Moon et al. *Electron Devices Meeting*. presented at. Whashington, DC, USA, Dec. 2003.

[6] M. Östling et al. "A comparative study of the diffusion barrier properties of TiN and ZrN". In: *Thin Solid Films* 145 (1986), pp. 81–88.

[7] A. Didden et al. "Titanium nitride: a new Ohmic contact material for n-type CdS". In: *Journal of Applied Physics* 110 (2011).

[8] G. V. Naik, V. M. Shalaev, and A. Boltasseva. "Alternative plasmonic materials: beyond gold and silver". In: *Advanced Materials* 25 (2013), pp. 3264–3294.

[9] T. Lee et al. "Environment-dependent nanomorphology of TiN: the influence of surface vacancies". In: *Nanoscale* 4 (2012), pp. 5183–5188.

[10] P. Patsalas et al. "Conductive nitrides: growth principles, optical and electronic properties, and their perspectives in photonics and plasmonics". In: *Materials Science and Engineering R* 123 (2018), pp. 1–55.

[11] W. Li et al. "Refractory plasmonics with titanium nitride: broadband metamaterial absorber". In: *Advanced Materials* 26 (2014), pp. 7956–7965.

[12] L. Meng and M. P. Dos Santos. "Characterization of titanium nitride films prepared by dc reactive magnetron sputtering at different nitrogen pressures". In: *Surface and Coatings Technology* 90 (1997), pp. 64–70.

[13] N. Arshi et al. "Study on structural, morphological and electrical properties of sputtered titanium nitride films under different argon gas flow". In: *Materials Chemistry and Physics* 134 (2012), pp. 839–844.

[14] L. Toth. *Transition metal carbides and nitrides.* Ed. by Academic Press Inc. 1971.

[15] H. A. Wriedt and J. L. Murray. "The N-Ti (Nitrogen-Titanium) system". In: *Bulletin of Alloy Phase Diagrams* 8 (1987), pp. 378–388.

[16] U. Guler, V. M. Shalaev, and A. Boltasseva. "Nanoparticle plasmonics: going practical with transition metal nitrides". In: *Material Today* 4 (2015), pp. 227–237.

[17] Z. Khezripour, F. F. Mahani, and A. Mokhtari. "Performance improvement of thin-film silicon solar cells using transversal and longitudinal titanium nitride plasmonic nanogratings". In: *Optical Materials* 99 (2020).

[18] A. Naldoni et al. "Broadband hot-electron collection for solar water splitting with plasmonic titanium nitride". In: *Advanced Optical Materials* 5 (2017).

[19] H. A. Atwater and A. Polman. "Plasmonic for improved photovoltaic devices". In: *Nature Materials* 9 (2010), pp. 205–213.

[20] G. M. Matenoglou et al. "Structure and electronic properties of conducting, ternary Ti x Ta 1- x N films". In: *Journal of Applied Physics* 105 (2009).

[21] M. Marlo and V. Milman. "Density-functional study of bulk and surface properties of titanium nitride using different exchange-correlation functionals". In: *Physical Review B* 62 (2000), p. 2899.

[22] P. Patsalas and S. Logothetidis. "Optical, electronic, and transport properties of nanocrystalline titanium nitride this films". In: *Journal of Applied Physics* 90 (2001), pp. 4725–4734.

[23] P. Patsalas and S. Logothetidis. "Interface properties and structural evolution of TiN/Si and TiN/GaN heterostructures". In: *Journal of applied physics* 93 (2003), pp. 989–998.

[24] S. Logothetidis, I. Alexandrou, and A. Papadopoulos. "*In situ* spectroscopic ellipsometry to monitor the process of TiN_X thin films deposited by reactive sputtering". In: *Journal of Applied Physics* 77 (1995).

[25] J. S. Chawla, X. Y. Zhang, and D. Gall. "Effective electron mean free path in TiN(001)". In: *Journal of Applied Physics* 113 (2013).

[26] D. Shah et al. "Optical properties of plasmonic ultrathin TiN films". In: *Advanced Optical Materials* 5 (2017).

[27] J. Yu et al. "Titanium Nitride Electron-Conductive Contact for Silicon Solar Cells By RF Sputtering from a TiN Target". In: *ACS Applied Materials & Interfaces* 12 (2020).

[28] W. Xiang, Y. Liu, and J. Zhang. "Influence of Microstructure on the Electrical Properties of Heteroepitaxial TiN Films". In: *Electronic Materials Letters* 14 (2018), pp. 314–318.

[29] Y. L. Jeyachandran et al. "Properties of titanium nitride films prepared by direct current magnetron sputtering". In: *Materials Science and Engineering: A* 445-446 (2007), pp. 223–236.

[30] F. Elstner et al. "Structure and properties of titanium nitride thin films deposited at low temperatures using direct current magnetron sputtering". In: *Journal of Vacuum Science Technology A* 476 (1994).

[31] Y. H. Cheng. "Substrate bias dependence of Raman spectra for TiN films deposited by filtered cathodic vacuum arc". In: *Journal of Applied Physics* 92 (2002).

[32] D. M. Devia, E. Restrepo-Parra, and P. J. Arango. "Comparative study of titanium carbide and nitride coatings grown by cathodic vacuum arc technique". In: *Journal of Applied Physics* 258 (2011), pp. 1164–1174.

[33] E. Langereis et al. "*In situ* spectroscopic ellipsometry study on the growth of ultrathin TiN films by plasmaassisted atomic layer deposition". In: *Journal of Applied Physics* 100 (2006).

[34] Lee. Y. J. "Low-impurity, highly conformal atomic layer deposition of titanium nitride using $NH_3\breve{}Ar\breve{}H_2$ plasma treatment for capacitor electrodes". In: *Materials Letters* 59 (2005), pp. 615–617.

[35] M. H. Staia et al. "Chemical vapour deposition of TiN on stainless steel". In: *Surface and Coatings Technology* 76-77 (1995), pp. 231–236.

[36] J. Laimer, H. Störi, and P. Rödhammer. "Titanium nitride deposited by plasma-assisted chemical vapour deposition". In: *Thin Solid Films* 191 (1990), pp. 77–89.

[37] R. Chowdhury et al. "Characteristic of titanium nitride films grown by pulsed laser deposition". In: *Journal of Materials Research* 11 (1996), pp. 1458–1469.

[38] L. E. Koutsokeras, G. M. Matenoglou, and P. Patsalas. “Structure, electronic properties and electron energy loss spectra of transition metal nitride films”. In: *Applied Physics Letters* 94 (2004).

[39] J. M. Lackner et al. “Structural, mechanical and tribological investigations of pulsed laser deposited titanium nitride coatings”. In: *Thin Solid Films* 453-454 (2004), pp. 195–202.

[40] S. Mahieu et al. “Biaxial alignment in sputter deposited thin films”. In: *Thin Solid Films* 515 (2006), pp. 1229–1249.

[41] G. Abadias, Y. Y. Tse, and P. Guérin. “Interdependence between stress, preferred orientation, and surface morphology of nanocrystalline TiN thin films deposited by dual ion beam sputtering”. In: *Journal of Applied Physics* 99 (2003).

[42] U. C. Oh and J. H. Je. “Effects of strain energy on the preferred orientation of TiN thin films”. In: *Journal of Applied Physics* 74 (1993).

[43] B. A. Movchan and A. V. Demchishin. “Structure and properties of thick condensates of nickel, titanium, tungsten, aluminum oxide, and zirconium dioxide in vacuum”. In: *Fiz. Metal. Metalloved.* 28 (1969), pp. 653–660.

[44] I. Petrov et al. “Microstructural evolution during film growth”. In: *Journal of Vacuum Science & Technology A* 21 (2003), pp. 117–123.

[45] J. A. Thornton. “High rate thick film growth”. In: *Annual Review of Material Science* 7 (1977), pp. 239–260.

[46] A. Anders. “Microstructural evolution during film growth”. In: *Thin Solid Films* 518 (2010), pp. 4087–4090.

[47] P. R. Willmott and J. R. Huber. “Pulsed laser vaporization and deposition”. In: *Reviews of Modern Physics* 72 (2000).

[48] B. Major et al. “Titanium-based films deposited using a Nd:YAG pulsed laser”. In: *Applied Physics A* 69 (1999).

[49] D. Walton. “Nucleation of vapor deposits”. In: *The journal of chemical physics* 37 (1962), pp. 2182–2188.

[50] J. A. Floro et al. “The dynamic competition between stress generation and relaxation mechanisms during coalescence of Volmer-Weber thin films”. In: *Journal of Applied Physics* 89 (2001), pp. 4886–4897.

[51] A. S. Ingason et al. “$In - situ$ electrical characterization of ultrathin TiN films grown by reactive dc magnetron sputtering on SiO_2”. In: *Thin Solid Films* 517 (2009), pp. 6731–6736.

[52] A. Satta et al. "Growth mechanism and continuity of atomic layer deposited TiN films on thermal SiO 2". In: *Journal of applied physics* 92 (2002), pp. 7641–7646.

[53] R. Abermann and R. Koch. "The internal stress in thin silver, copper and gold films". In: *Thin Solid Films* 129 (1985), pp. 71–78.

[54] Z. Y. Hang and C. V. Thompson. "Grain growth and complex stress evolution during Volmer–Weber growth of polycrystalline thin films". In: *Acta Materialia* 67 (2014), pp. 189–198.

[55] D. R. McKenzie et al. "The orientation dependence of elastic strain energy in cubic crystals and its application to the preferred orientation in titanium nitride thin films". In: *Journal of Physics: Condensed Matter* 8 (1996).

[56] Y. M. Chen, G. P. Yu, and J. H. Huang. "Role of process parameters in the texture evolution of TiN films deposited by hollow cathode discharge ion plating". In: *Surface and Coatings Technology* 141 (2001), pp. 156–163.

[57] S. Mahieu, D. Depla, and R. De Gryse. "Modelling the growth of transition metal nitrides". In: *Journal of Physics: Conference Series* 100 (1995).

[58] P. Patsalas, C. Gravalidis, and S. Logothetidis. "Surface kinetics and subplantation phenomena affecting texture, morphology, stress, and growth evolution of titanium nitride films". In: *Journal of Applied Physics* 96 (2004).

[59] S. H. Kim et al. "Structure and mechanical properties of titanium nitride thin films grown by reactive pulsed laser deposition". In: *Journal of Ceramic Processing Research* 10 (2009), pp. 49–53.

[60] W Ensinger. "Ion bombardment effects during deposition of nitride and metal films". In: *Surface and Coatings Technology* 99 (1998), pp. 1–13.

[61] R. A. Kant et al. "The causes of property variations of IBAD-titanium nitride". In: *Materials Research Society* 128 (1989).

[62] G. H. Tompkins. "The initial stages of the oxidation of titanium nitride". In: *Journal of Applied Physics* 71 (1992).

[63] A. Glaser et al. "Oxidation of vanadium nitride and titanium nitride coatings". In: *Surface Science* 601 (2007), pp. 1153–1159.

[64] N. C. Saha and H. G. Tompkins. "Titanium nitride oxidation chemistry: an xray photoelectron spectroscopy study". In: *Journal of Applied Physics* 72 (1992).

[65] I. Milošv et al. “Electrochemical and thermal oxidation of TiN coatings studied by XPS”. In: *Surface and Interface Analysis* 23 (1995), p. 529.

[66] L. Zhang et al. “Ion beam modification of plasmonic titanium nitride thin films”. In: *Journal of Materials Science* 52 (2017).

[67] L. Zhang et al. “Effects of sputtering and assisting ions on the orientation of titanium nitride films fabricated by ion beam assisted sputtering deposition from metal target”. In: *Materials Letters* 171 (2016), pp. 304–307.

[68] E. Ribeiro et al. “Characterization of hard DC-sputtered Si-based TiN coatings: the effect of composition and ion bombardment”. In: *Surface and Coatings Technology* 188 (2004), pp. 351–357.

[69] M. Mazza. “Synthesis and optical properties of titanium nitride nanostructured thin films”. MA thesis. Politecnico di Milano, 2020.

[70] R. Eason. *Pulsed Laser Deposition of thin films*. Ed. by John Wiley Sons. 2007.

[71] L. Mascaretti. “Hydrogen-treated titanium dioxide hierarchical nanostructures for water splitting applications”. PhD thesis. Politecnico di Milano, 2018.

[72] A. Pazzaglia. “Produzione e caratterizzazione di bersagli multistrato per l’accelerazione di ioni mediante laser superintensi”. MA thesis. Politecnico di Milano, 2015.

[73] M. A. Sutton et al. “Scanning Electron Microscopy for Quantitative Smalland Large Deformation MeasurementsPart I: SEM Imaging at Magnifications from 200 to 10,000”. In: *Experimental Mechanics* 47 (2007), pp. 775–787.

[74] Y. Kim et al. “Endoscopic imaging using surface-enhanced Raman scattering”. In: *European Journal of Nanomedicine* 9 (2017), pp. 91–104.

[75] A. Perego et al. “Hierarchical TiN nanostructured thin film electrode for highly stable PEM fuel cells”. In: *ACS Applied Energy Materials* 3 (2019), pp. 1911–1922.

[76] J. Lindemuth. *Hall effect measurement handbook*. Ed. by Lake Shore Cryotronics Inc. 2020.

[77] F. Wooten. *Optical Properties of Solids*. Ed. by Inc. Academic Press. 1972.

[78] H. Köstlin, R. Jost, and W. Lems. “Optical and electrical properties of doped In_2O_3 films”. In: *Physica Status Solidi (a)* 29 (1975), pp. 87–93.

[79] A. Trenczek-Zajac et al. “Structural and electrical properties of magnetron sputtered Ti(ON) thin films: the case of TiN doped in situ with oxygen”. In: *Journal of Power Sources* 194 (2009), pp. 93–103.

[80] C. G. Ribbing and A. Roos. “Transition-metal-nitride films for optical applications”. In: *Optical Thin Films V: New Developments* 3133 (1997), pp. 148–162.

[81] A. Skerlavaj, Y. Claesson, and C. G. Ribbing. “Optimizing optical properties of reactively sputtered titanium nitride films”. In: *Thin Solid Films* 186 (1990), pp. 15–26.

[82] S. Niyomsoan et al. “Variation of color in titanium and zirconium nitride decorative thin films”. In: *Thin Solid Films* 415 (2002), pp. 187–194.

[83] E. Besozzi et al. “Coefficient of thermal expansion of nanostructured tungsten based coatings assessed by substrate curvature method”. In: *Materials & Design* 137 (2018), pp. 192–203.

[84] S. Canulescu et al. “Mechanisms of the laser plume expansion during the ablation of $LiMn_2O_4$”. In: *Journal of Applied Physics* 105 (2009).

[85] R. Chowdhury et al. “Characteristics of titanium nitride films grown by pulsed laser deposition”. In: *Journal of Materials Research* 11 (1996), pp. 1458–1469.

[86] G. Zhao et al. “Electrical and optical properties of titanium nitride coatings prepared by atmospheric pressure chemical vapor deposition”. In: *Journal of non-crystalline solids* 354 (2008), pp. 1272–1275.

[87] X. Yang et al. “Dual-function electron-conductive, hole-blocking titanium nitride contacts for efficient silicon solar cells”. In: *Joule* 3 (2019), pp. 1314–1327.

[88] B. O. Johansson et al. “Growth and properties of single crystal TiN films deposited by reactive magnetron sputtering”. In: *Journal of Vacuum Science & Technology A: Vacuum, Surfaces, and Films* 3 (1985), pp. 303–307.

[89] P. LeClair, G. P. Berera, and J. S. Moodera. “Titanium nitride thin films obtained by a modified physical vapor deposition process”. In: *Thin Solid Films* 376 (2000), pp. 9–15.

[90] D. Dellasega et al. “Role of energetic ions in the growth of fcc and ω crystalline phases in Ti films deposited by HiPIMS”. In: *SSRN* (2020).

[91] N. Pryds et al. “Growth of thin films of TiN on MgO (100) monitored by high-pressure RHEED”. In: *Applied Physics A* 93 (2008), pp. 705–710.

[92] S. A. Maier. *Plasmonics fundamental and applications.* Ed. by Springer. 2010.